Cascaded nonlinearities for ultrafast nonlinear optical science and applications

Bache, Morten

Publication date:
2017

Document Version
Publisher's PDF, also known as Version of record

Cascaded nonlinearities for ultrafast nonlinear optical science and applications

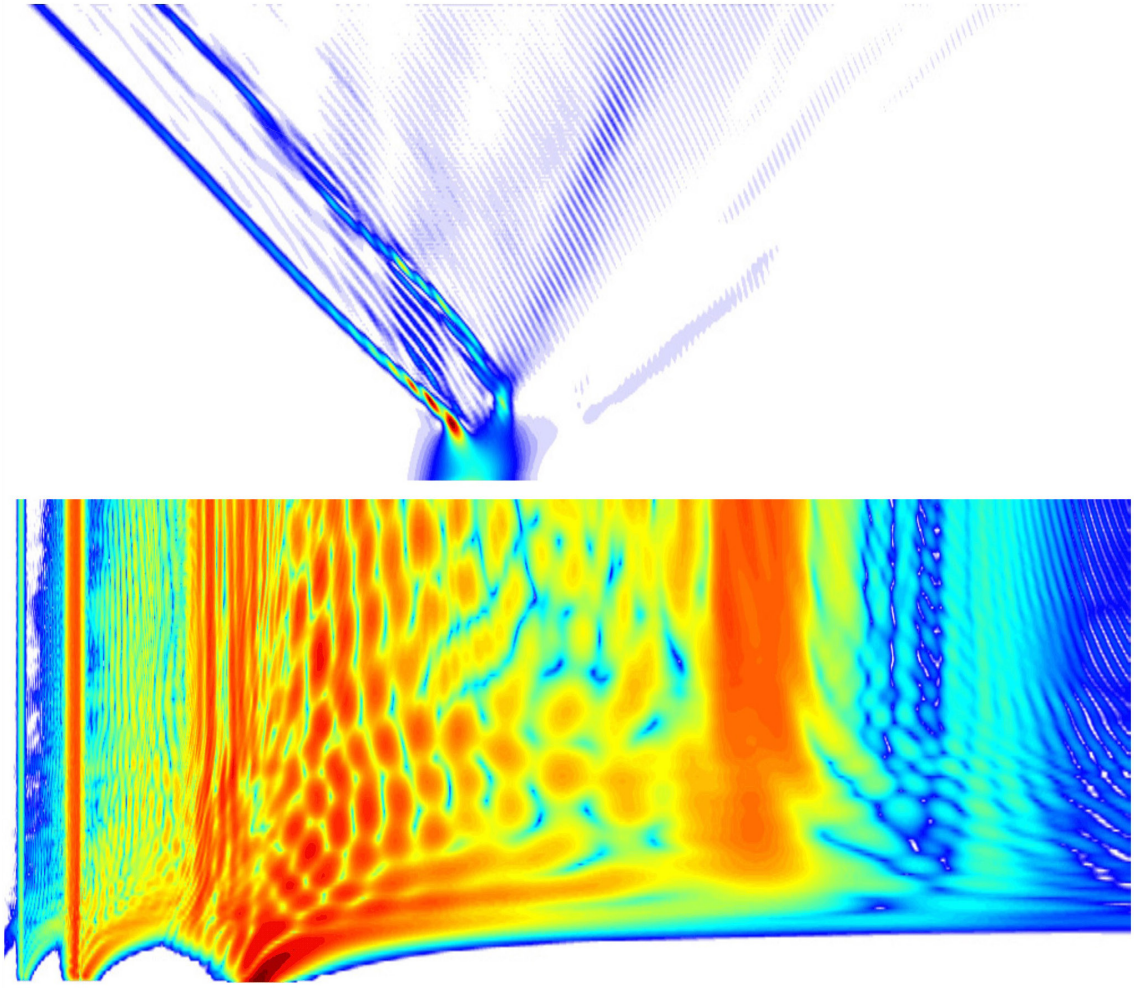

Morten Bache

Doctor Technices Thesis

DTU Fotonik
Department of Photonics Engineering

Denne afhandling er af Danmarks Tekniske Universitet antaget til forsvar for den tekniske doktorgrad. Antagelsen er sket efter bedømmelse af den foreliggende afhandling.

Kgs. Lyngby, den 6. februar 2018

Anders O. Bjarklev
Rektor

/Rasmus Larsen
Prorektor

This thesis has been accepted by the Technical University of Denmark for public defence in fulfilment of the requirements for the degree of Doctor Technices. The acceptance is based on an evaluation of the present dissertation.

Kgs. Lyngby, 6 February 2018

Anders O. Bjarklev
President

/Rasmus Larsen
Provost

Cascaded nonlinearities for ultrafast nonlinear optical science and applications

Morten Bache
DTU Fotonik, Technical University of Denmark
Doctor Technices Thesis

1 September 2017

Abstract

Cascaded nonlinearities in quadratic nonlinear crystals underlie an immensely powerful control over the ultrafast nonlinear response, where it is possible at will to change the sign of the nonlinearity and tune its strength seamlessly from weak to extremely strong. Here the physics behind the cascading nonlinearity is investigated in detail, especially with focus on femtosecond energetic laser pulses being subjected to this nonlinear response. Analytical, numerical and experimental results are used to understand the cascading interaction and applications are demonstrated. The defocusing soliton is of particular interest here, since it is quite unique and provides the solution to a number of standing challenges in the ultrafast nonlinear optics community. It solves the problem of catastrophic focusing and formation of a filaments in bulk glasses, which even under controlled circumstances is limited to energies of a few μJ. In contrast, the defocusing soliton can sustain orders of magnitude larger energies. It also solves the challenge of using mature near-IR laser technology to generate ultrashort, coherent and bright mid-IR radiation. The defocusing nonlinear effect that leads to intriguing observations with analogies in fiber optics are observed numerically and experimentally, including soliton self-compression, soliton-induced resonant radiation, supercontinuum generation, optical wavebreaking and shock-front formation. All this happens despite no waveguide being present, thanks to the defocusing nonlinearity. Finally, the richness of the complex nonlinear system is immense, and as an example the first observation of parametrically tunable resonant radiation is shown, phase-matched to the defocusing soliton, and emitted in the mid-IR and the visible/near-IR.

Resumé

Kaskader af ulinearitetet i kvadratiske ulineære krystaller ligger til grund for en ekstrem grad af kontrol over det ultrahurtige ulineære respons, hvor det er muligt efter behov at ændre fortegn på ulinearitetet samt at tilpasse dens styrke på kontinuert vis fra svag til ekstremt stærk. Her undersøges fysikken bag kaskadeulinearitetet i detaljer, især med fokus på energiske laserimpulser med femtosekund varighed der udsættes for dette ulineære respons. Analytiske, numeriske og eksperimentelle resultater bruges til at forstå kaskadeinteraktioner og anvendelser bliver demonstreret. Den defokuserende soliton er af særlig interesse her, da den er helt unik og løser en række stående udfordringer i det ultrahurtige, ulineære optiksamfund. Den løser problemet med katastrofal selvfokusering og dannelse af filamenter i glasser, som selv under kontrollerede omstændigheder er begrænset til energier på nogle få μJ. I modsætning hertil kan den defokuserende soliton understøtte størrelsesordener større energier. Den løser også udfordringen ved at bruge moden nær-IR-laser teknologi til at generere ultrakorte, kohærente og kraftig laserstråler. Den defokuserende ulineære effekt, der fører til spændende observationer med analogier til fiberoptik, observeres numerisk og eksperimentelt, herunder soliton-selvkompression, soliton-induceret resonansstråling, superkontinuumgenerering, optisk bølgebrydning og chokfrontdannelse. Alt dette sker, selvom der ingen bølgeleder er til stede, takket være den defokuserende ulinearitet. Endelig er righoldigheden af det komplekse, ulineære system enormt, og som et eksempel vises den første observation af parametrisk kontrollerbar resonansstråling, fase-låst med defokuserings-solitonen, og som dannes i det mellem-infrarøde henholdsvis det synlige / nær-infrarøde.

Preface

This Doctor Technices thesis covers a decade worth of contributions aiming at advancing ultrafast nonlinear optics by exploiting so-called cascaded nonlinear effects in crystals with a quadratic nonlinear response. Central to the thesis are 14 peer-reviewed papers that I have co-authored within theory, mathematical modeling, numerical simulations and experiments. In all of these papers my contributions were substantial in all aspects, from conceiving the ideas, obtaining funding, executing the research, writing the papers, as well as, when needed, coordinating the international collaborations required to get the results done.

That being said, I cannot take credit for executing the experiments behind some of these papers, and this task fell in large part on Dr. Binbin Zhou, to whom I owe a great thanks for staying in my team over most of the time covered by this thesis.

The work of this thesis commenced by an encounter at an international conference, where I met prof. Frank Wise and then Ph.D. student Jeffrey Moses from Cornell University. They introduced me to cascading, and we have had a wonderful collaboration on various topics over the years. To both of them I owe an enormous gratitude. I should also extend thanks to prof. Andy Chong, formerly of Cornell University, who conducted the very first experiment with Binbin at Cornell.

I also want to thank prof. Ole Bang, DTU Fotonik, and prof. Wieslaw Krolikowski, Australian National University, who showed me the exciting world of nonlocal nonlinear responses, which was the first platform we used to understand ultrafast cascaded nonlinearities.

I also want to thank prof. Xianglong Zeng, Shanghai University, for selecting to collaborate with me during a Marie Skłodowska Curie individual fellowship and for bringing Dr. Hairun Guo with him to DTU, who decided to carry out his PhD at DTU Fotonik. This collaboration ended up tying a very nice bow on the research presented in this thesis. In this connection I also want to thank Dr. Xing Liu, who during his PhD in my team provided the deciding push towards opening the door for understanding the three-wave mixing resonant radiation waves we struggled so hard to comprehend. Finally, also thanks to prof. Xianfeng Chen, Shanghai Jiao Tong Univeristy, and prof. Yen-Hung Chen and Dr. Hung-Pin Chung from National Central University, Taiwan, for providing suitable crystal samples for the PPLN experiments.

I should also thank prof. Satoshi Ashihara, Univ. of Tokyo, for sharing insight into cascaded nonlinearities, and for many good discussions over the years. Also thanks to prof. Roland Schiek, Univ. of Regensburg, for extremely generous sharing of data and long discussions on arguably the most important crystal in the nonlinear optics community, lithium niobate.

I want to thank the following for vibrant scientific discussions of the topics in this thesis over these years: all my current and former colleagues at DTU Fotonik, especially prof. Asger Mortensen, prof. Peter Uhd Jepsen, prof. Karsten Rottwitt, Dr. Michael Frosz, Dr. Jesper Lægsgaard, prof. Leif Katsuo Oxenløwe, prof. Dmitry Turchinovich, Dr. David Cooke, Dr. Krzysztof Iwaschuk, and all my international collaborators who have contributed to the cascading results over the past years: Dr. Stefano Minardi, prof. Thomas Pertsch, Dr. Matteo Conforti, prof. Fabio Baronio, Dr. Fabio Biancalana, Dr. Poul B. Petersen, Dr. Ashley Stingel, Dr. Heather Vanselous, prof. Valentin Petrov, prof.

Jens Biegert, Dr. Cord Arnold, prof. Johan Mauritsson, Dr. Marcus Seidel, prof. Matthieu Chauvet, prof. Fabrice Devaux, Dr. Miro Erkintalo, prof. Robert Boyd, Dr. Chris Phillips, prof. Marty Fejer, Dr. Santosh Raavi, prof. Christoph Hauri, prof. Mansoor Sheik-Bahae, prof. George Stegeman, prof. François Hache, prof. Goëry Genty, prof. John Dudley, prof. Thibaut Sylvestre, Dr. Ji Wei, Dr. Tan Huiming, prof. Rashid Ganeev, prof. Valentin Petrov, prof. Audrius Pugzlys, prof. Paolo di Trapani, Dr. Ottavia Jedrkiewicz, Dr. Enrico Brambilla and many others.

I would also like to extend a thanks to the thesis opponents, prof. Katia Gallo, KTH, and prof. Dmitry Skryabin, University of Bath, as well as the the thesis committee chairman, prof. Mads Peter Sørensen, DTU Compute.

Finally, a special thanks to my patient family at home for giving me the space to write this thesis: Philip and Sebastian, who are still too young to understand or care about ultrafast lasers, and of course to my beloved wife Barbara, who has supported me during my entire post-doctoral career.

Contents

Chapter 1

Introduction

oh nossai
yu saleno uei for daun
tche
yu sailefon daun, on na

al ta on

daun tche wún

Sigur Rós “Popplagið”

This thesis covers my main contributions over the past decade to cascaded nonlinearities for ultrafast nonlinear optical science and applications.[1]

The research was originally motivated by providing solutions for overcoming obstacles in the near-IR for getting routinely access to bright, few-cycle and broadband laser pulses. A current challenge is to provide similar access to bright, few-cycle and broadband laser pulses over the entire mid-IR range. Energetic mid-IR femtosecond lasers inevitably operate in selected wavelength regimes with limited bandwidths and provide pulses that are longer than the desired few-cycle duration. The scientific need for bright, broadband, and few-cycle pulses, flexibly provided across a wide spectral range, such as the mid-IR, is therefore challenging. The overshadowing objective of my work has for the past 6 years been to develop generic methods in the mid-IR to expand the bandwidth, provide efficient frequency conversion of few-cycle pulses, and to achieve compression of bright laser pulses to few-cycle duration. To do this, cascaded quadratic nonlinearities in bulk crystals have been used. The method employs an effective self-defocusing nonlinearity, and is therefore not subject to beam collapse or filamentation, and can be scaled to extreme energy levels.

Cascaded nonlinearities can have several meanings, but the focus of this thesis is the very simple case of cascaded second-harmonic generation (SHG). It is simple in the sense there is only one pump, which we call the fundamental wave (FW), and by making the nonlinear crystal phase-mismatched for SHG ($\Delta k \neq 0$), the FW experiences a nonlinear phase shift that is Kerr-like in nature ("self acting" [15]). To understand this phenomenologically, cascaded SHG occurs when the nonlinear conversion process is strongly phase

[1] For sake of clarity the 14 central papers to this thesis are chronologically numbered 1-14 both here in the main text and in the appended versions of the papers.

mismatched. On a microscopic scale moderate (due to the nozero Δk) up-conversion after one coherence length $\pi/|\Delta k|$ to the second harmonic (SH) is followed by the reverse process of down-conversion to the FW after a coherence length. On continued propagation, the macroscopic picture shows that SH is cyclically generated and back-converted (the so-called cascade of nonlinear effects). During this process the FW essentially experiences a nonlinear phase shift due to the difference in phase velocities (this is the direct consequence of a nonzero phase-mismatch), and the magnitude and sign of the phase shift are determined by the phase-mismatch parameter: the *sign* of the nonlinear phase shift is *controllable* by the sign of Δk and the *strength* is proportional to $1/\Delta k$. For large enough phase-mismatch values this nonlinear phase shift behaves in every way as the Kerr effect: it builds up linearly as the pulse propagates through the crystal and it acts nonlinearly through the modulo square of the electric field (i.e. proportional to the intensity).

There are two key aspects about cascaded quadratic nonlinearities that have been (and remain) the main attractions: Firstly, the defocusing (negative) Kerr-like nonlinearity provides solutions to some key challenges and provide new possibilities that have not emerged in other systems. This is not only the fact that the cascading can provide a negative nonlinear effect, it is also that it can cancel and even overcome the competing material self-focusing nonlinearity[2]. Therefore the negative nonlinearity becomes the *leading* nonlinear effect. This sets it clearly apart from other cases where higher-order nonlinear terms can become negative in sign, as is the case for cascaded third-harmonic generation [16, 17]. Secondly, the cascading nonlinearity is in essence completely tunable in both sign and strength through the SHG phase-mismatch parameter. This unique property has attracted much attention historically since the first experimentally demonstration [18] where the cascaded nonlinearity was shown to be tunable in sign and strength $n_2^{\text{casc}} \propto -d_{\text{eff}}^2/\Delta k$, where d_{eff} is the effective quadratic nonlinearity. Most importantly it became clear that a self-defocusing effect was accessible ($n_2^{\text{casc}} < 0$, requiring $\Delta k > 0$).

Cascaded quadratic nonlinearities have since been extensively investigated experimentally recently for ultrafast pulse compression and soliton formation [19, 20, 21, 22, 23, 24, 25, 26, 27, 28, 29, 7, 30], supercontinuum generation [31, 32, 33, 7, 10, 13, 14, 34], white light continuum from filaments [35, 36, 37, 38, 39, 40], frequency comb generation [41, 42], femtosecond modelocking [43, 44, 45, 46, 47, 48, 49, 50, 51], compensation of self-focusing effects [52, 53], material properties [54, 55, 8, 56] and ultrafast pulse control [57, 58, 59, 60, 61, 62, 63, 56, 64, 65, 66, 67, 68, 69, 70, 71, 72].

As mentioned, a controllable leading-order self-defocusing nonlinearity is quite unique, and quite some effort was therefore invested in applications of this effect in bulk crystals. One early application was pulse compression of energetic pulses, because in bulk glasses the required spectral broadening was accompanied by self-focusing, limiting the pulse energy [73]. The idea by using cascading is to compensate for the material Kerr self-focusing, making the net total nonlinearity negative, $n_2^{\text{tot}} = n_2^{\text{casc}} + n_2^{\text{SPM}} < 0$, by using cascaded effects, and this would give a filament-free pulse compressor without any limitations associated with filamentation; it was first investigated in [20], where an SPM-induced self-defocusing spectral broadening was induced in a quadratic nonliner crystal (BBO, beta-barium borate). The effective self-defocusing nonlinearity gave a negative

[2] "Self-focusing" stems from the fact the nonlinear Kerr effect in the material creates a lens-effect on the beam, proportional to the beam intensity; it is therefore the nonlinear action by the beam itself that focuses it, hence the name.

chirp across the pulse, so the pulse could be compressed by passing it through a piece of bulk glass with positive normal dispersion.

Around the same time the hollow fiber compressor was shown [74] and later filament-based compression [75]. These became the routine choice for pulse compression, even if they typically were restricted to 1 mJ, give or take. Today this limit has been moved to around 40 mJ in planar hollow waveguides (final energy 20 mJ) [76]. Still, it is remarkable that for high-peak power pulses the scaling of the cascading technique is only limited by the crystal aperture.

Another type of cascading-based pulse-compression experiment was some years later conducted by Ashihara et al. [23], where instead of compressing the pulse "externally", they achieved soliton self-compression inside the crystal. This is because at the pump wavelength (800 nm from a TiSa amplifier) BBO has normal group-velocity dispersion (GVD), and in this case exciting a soliton requires $n_2^{\text{tot}} < 0$. Although the soliton excitation was confirmed, the compression ratio was moderate. This is because BBO has a large group-velocity mismatch (GVM) between pump and SH at this wavelength, and indeed later experiments at longer wavelengths have shown few-cycle soliton self-compression in BBO due to a reduced GVM [27, 12].

In the case of defocusing soliton formation, it may become phase-matched to generate resonant radiation waves (RR waves, a.k.a. dispersive waves) [77]. Since the defocusing soliton needs normal dispersion to form, the RR wave will naturally be generated in the anomalous dispersion regime, i.e. to the long-wavelength side [5, 6]. This was recently experimentally verified in bulk BBO and LN [12, 11], and together with the soliton the RR wave(s) constitute the octave-spanning supercontinuum in the defocusing soliton case.

A remarkable point about the supercontinuum generated by the defocusing soliton and the RR waves is that since they are filament free they can carry 100's of μJ of energy, and are scalable even to mJ of energy and beyond if the parametric amplifier allows for it [11, 12]. This potentially makes cascading-based supercontinuum generation the brightest supercontinuum source in condensed matter, and it can even be implemented directly in the mid-IR [13]. The only techniques currently capable of similar energies are multi-stage thin plates, which was recently scaled to around 1 mJ [78] and also the recent trend in pumping glass plates in the strongly anomalous dispersion range [79], where filamentation seems to be suppressed if sub-10 cycle pump pulses are used [80]. The obvious drawback is the necessity of having to use such a powerful few-cycle front end well into the infrared to get large anomalous dispersion.

The defocusing soliton-induced RR waves are quite similar to the ones observed in Kerr media, since they are phase-matched by four-wave mixing (4WM, degenerate [12, 11] or non-degenerate case [12, 81]), but with the cascaded quadratic nonlinearity we also found that there are unique three-wave mixing (3WM) analogues. They were recently observed experimentally for the first time [10, 14]. Especially in the latter experiment, conducted in a standard periodically poled LN crystal, it became clear that these RR waves are quite different than ordinary RR waves from SPM. They become phase-matched to the soliton through the sum-frequency generation or difference-frequency generation terms. Essentially through phase-mismatch control the spectral position of the RR wave can be controlled parametrically, in BBO over a significant part of the visible range though the SHG/SFG term, while in LN the DFG term gives an RR wave that was tunable in the mid-IR from $4.0 - 5.5$ μm.

One particular feature of cascaded quadratic nonlinearities is that they induce a non-local nonlinearity, either spatially [82] or temporally [1]. In the spatial nonlocal case, the nonlinearity depends not only on the local intensity but also on its neighboring points [83] (see [84] for a review). In the temporal case the nonlocal action comes about because the SH group velocity is different than the FW group velocity, so as the nonlinear phase-shift accumulates, it does so more in the direction of the group-velocity mismatch than in the pulse center; this is the definition of a non-local nonlinearity. In time-domain a first-order expansion of the nonlocal response [85] reveals the analogy to the cascading-induced controllable pulse self steepening [63, 56], while a frequency-domain description reveals that the nonlocal response can be either non-resonant or resonant. In the resonant case, our recent experiment shows that the FW can be phase-matched directly to a detuned frequency in the SH spectrum [10]. This leads to a substantial depletion of the FW. When the FW is a defocusing soliton this phase-matching condition turns out to be exactly equivalent to the new SFG RR wave described above [14]. When the FW is not a soliton, we recover the standard phase-matching condition in the SH to a sideband of the broadband FW pump [10], i.e. the condition investigated in historical experiments [86, 19, 87, 88, 89, 65, 67, 70].

Many early cascading experiments were performed in BBO, where the SHG phase-matching scheme is "critical" or birefringence phase-matching. An entirely different approach is to use "non-critical" interaction, i.e. so-called type 0 interaction where FW and SH have the same polarization. The advantages are that one may exploit the large diagonal tensor components, e.g. the d_{33} of LN, and that spatial walk-off is nil. The cascading defocusing soliton was experimentally observed at 1.3 μm in a just 1 mm long unpoled LN crystal (a truly compact pulse compressor) [7], and in longer crystals an octave-spanning supercontinuum was observed. For supercontinuum generation in type 0 crystals the added bonus is that the SH has the same polarization as the pump, so there can be a considerable harmonic extension of the continuum (multiple octaves have been observed in periodically poled LN (PPLN) waveguides [32, 33] and recently also in bulk PPLN [14]). However it is worth to stress that the LN experiment in [7] did not use periodic poling, and still a net total defocusing nonlinearity was observed. Inspired by this we proposed figure-of-merit parameter for type 0 crystals FOM $= -n_2^{\text{casc}}/n_2^{\text{SPM}}$ and if FOM > 1 then the self-defocusing nonlinearity is dominating. LN has indeed an FOM > 1 in the near-IR (from 1.2-3.0 μm), and in [9] we investigated a wide range of mid-IR transparent crystals where type 0 interaction is possible. We were able to locate dozens of potential candidates that can be used for direct mid-IR pumping to get defocusing nonlinear effects for filament free pulse compression and supercontinuum generation with GW class pulses. Recently we tested one of them, $LiInS_2$, and successfully observed octave-spanning supercontinua (in the $2-7$ μm range) when pumped with 50 μJ pulses in the $3-4$ μm range in the mid-IR [13].

These cases highlight how sensible cascading is to uncertainties in the material parameters, linear as well as nonlinear. It has been crucial for our understanding of cascading to dedicate an effort in getting a better understanding the crystals we use. Even for well-known crystals like BBO and LN have we had to make a significant effort to improve the state-of-the-art knowledge [4, 7, 8, 90].

The thesis is structured as follows: In Chapter 2 the basic propagation equations for SHG are derived. In Chapter 3 I go through the basics of cascading, including a detailed

overview of how a femtosecond pump pulse is affected by nonlocal nonlinear cascading response, higher-order cascading and cascading-induced self-steepening. In Chapter 4 I review the progress we have contributed with in terms of improving the knowledge of the nonlinear crystals, including an experimental measurement of the Kerr nonlinearity of BBO and finally ending up with a figure-of-merit review of mid-IR type 0 crystals. In Chapter 5 I discuss the defocusing soliton, how we can understand it without reverting to detailed simulations. Here I show the experimental results observing the defocusing soliton in BBO and LN crystals. Chapter 6 deals with RR waves, carefully reviewing the classical phase-matching conditions for the SPM nonlinearity before passing on to the experimental observation in BBO and LN. The last part of the chapter is dedicated to the novel RR waves from three-wave mixing, first deriving the phase-matching conditions and then showing the experimental confirmation. I also discuss when RR waves are of solitonic vs non-solitonic origin. Chapter 7 reviews the experimental efforts in observing supercontinuum generation in BBO, LN, PPLN and $LiInS_2$. Finally, Chapter 8 concludes with a discussion of the obtained results and providing an outlook and discussing possibilities in other similar nonlinear systems.

Chapter 2

Second-harmonic generation

So I walked through to the haze
And a million dirty waves
Now I see you lying there

Foals "Spanish Sahara"

In this chapter I present the basic equations for modeling second-harmonic generation (SHG) with ultrafast laser pulses.

2.1 Basic SHG coupled wave equations

We consider SHG $\omega_1 + \omega_1 \to \omega_2$ between the FW (frequency ω_1) and the SH (frequency $\omega_2 = 2\omega_1$). The plane-wave coupled SHG equations under the slowly-varying envelope approximation (SVEA) of the electric field envelopes E_j are (in mks units)

$$\left[i\frac{\partial}{\partial\zeta} - \tfrac{1}{2}k_1^{(2)}\frac{\partial^2}{\partial\tau^2}\right]E_1 + \frac{\omega_1 d_{\text{eff}}}{cn_1}E_1^* E_2 e^{i\Delta k z} = 0 \tag{2.1a}$$

$$\left[i\frac{\partial}{\partial z} - id_{12}\frac{\partial}{\partial\tau} - \tfrac{1}{2}k_2^{(2)}\frac{\partial^2}{\partial\tau^2}\right]E_2 + \frac{\omega_1 d_{\text{eff}}}{cn_2}E_1^2 e^{-i\Delta k z} = 0 \tag{2.1b}$$

where $k_j(\omega) = n_j(\omega)\omega/c$ are the wave numbers, $n_j(\omega)$ the frequency dependent refractive indices of the FW ($j = 1$) and SH ($j = 2$), $n_j \equiv n_j(\omega_j)$, $\Delta k = k_2^{(0)} - 2k_1^{(0)}$ the phase mismatch parameter, $d_{12} = k_1^{(1)} - k_2^{(1)}$ the group-velocity mismatch (GVM) parameter, $k_j^{(2)}$ the group-velocity dispersion (GVD) coefficients. Generally $k_j^{(m)} = \frac{d^m k_j}{d\omega^m}|_{\omega=\omega_j}$ are the dispersion coefficients at the reference frequencies ω_j; we here only include up to 2. order dispersion for simplicity but will later generalize to higher-order dispersion. The equations have been transformed to the reference frame $\zeta = z$ and $\tau = t - zk^{(1)}(\omega_1)$, comoving with the group velocity of the FW.

We could also include self-steepening effects, but the analytical results we now present are unaffected by this. Kerr nonlinearities are also neglected for simplicity; the results presented are intended to investigate the SH dispersion and nonlinear properties when thick-crystal femtosecond SHG is operated under phase-mismatched interaction. This implies that the crystal length L is on the order of 10 mm or more, so the strongly phase-mismatched (cascading) limit $\Delta kL \gg 2\pi$ is always fulfilled. This means that the SH con-

version is weak, even for high FW intensities, and thus that Kerr self-phase and cross-phase modulation of the SH is insignificant. They are instead both very relevant for the FW, but this is not what we investigate here. Finally, d_{eff} is the effective $\chi^{(2)}$ nonlinearity.

2.2 Full SHG coupled wave equations

The basic SHG coupled wave equations is here presented in a more complete form for use in the following for analysis. It corresponds to the so-called slowly evolving wave approximation (SEWA) [91] in that it takes into account self-steepening, and also includes cubic nonlinear effects related to SPM and XPM.

The plane-wave SEWA equations for the electric field envelopes including self-steepening and Kerr SPM and XPM terms are [8]

$$\begin{aligned}&\left[i\partial_\zeta + \hat{D}_{\omega_1}\right]E_1 + \hat{S}_1\tfrac{\omega_1 d_{\text{eff}}}{n_1 c}E_1^* E_2 e^{i\Delta k\zeta}\\ &+\hat{S}_1\tfrac{3\omega_1}{8n_1 c}\left[\chi^{(3)}_{\text{SPM}}E_1|E_1|^2 + 2\chi^{(3)}_{\text{XPM}}E_1|E_2|^2\right] = 0 \qquad (2.2a)\\ &\left[i\partial_\zeta - id_{12}\partial_\tau + \hat{D}_{\omega_2}\right]E_2 + \hat{S}_2\tfrac{\omega_2 d_{\text{eff}}}{n_2 c}\tfrac{1}{2}E_1^2 e^{-i\Delta k\zeta}\\ &+\hat{S}_2\tfrac{3\omega_2}{8n_2 c}\left[\chi^{(3)}_{\text{SPM}}E_2|E_2|^2 + 2\chi^{(3)}_{\text{XPM}}E_2|E_1|^2\right] = 0 \qquad (2.2b)\end{aligned}$$

where $\hat{S}_j = 1 + i\omega_j^{-1}\partial_\tau$ are the self-steepening operators. The time-domain dispersion operator is

$$\hat{D}_{\omega_j} = \sum_{m=2}^{\infty} k_j^{(m)}\frac{i^m}{m!}\frac{\partial^m}{\partial t^m} \qquad (2.3)$$

and it can be truncated at any order to study effects of higher-order dispersion. Numerically we conveniently evaluate this directly in frequency domain as

$$\begin{aligned}\tilde{D}_{\omega_j}(\omega) &= \sum_{m=2}^{\infty} m!^{-1}(\omega-\omega_j)^m k_j^{(m)} \qquad (2.4)\\ &= k_j(\omega) - k_j^{(1)}(\omega-\omega_j) - k_j^{(0)} \qquad (2.5)\end{aligned}$$

where the latter is very useful since it can be evaluated without the need of a polynomial expansion.

For the cubic nonlinearity we take into account both self- and cross-phase modulation (SPM and XPM) using the *effective* nonlinear susceptibilities $\chi^{(3)}_{\text{SPM}}$ and $\chi^{(3)}_{\text{SPM}}$.[1] One warning here is that the cubic SPM and XPM susceptibilities are not (necessarily) the same. First of all, since we are dealing with crystals, the nonlinear susceptibilities depend on polarization and propagation angles of the field in the crystal coordinate system. Only when the FW and the SH have the same polarization (type 0 noncritical phase matching) does it hold that $\chi^{(3)}_{\text{SPM}} = \chi^{(3)}_{\text{XPM}}$, while for instance for type I (e.g. $oo \to e$ interaction) the classical result for cross-polarized fields $\chi^{(3)}_{\text{XPM}} = \chi^{(3)}_{\text{XPM}}/3$ only holds when $\theta = 0$ [8]. Another

[1] The nomenclature "effective" stems from the nonlinear crystal literature, and implies that the cubic nonlinearity is originating from various tensor components and the specific propagation angles (θ,ϕ) in the crystal coordinate system, exactly like the d_{eff} coefficient for the quadratic nonlinearity.

issue here to be aware of is that the nonlinear strength is not constant across the spectrum; usually an empirical Miller-type of scaling can be applied [92] or more complex models can be used (e.g. the two-band model [93]). Even if the FW and the SH by definition are an octave apart, in most cases it is a good approximation to neglect wavelength scaling of $\chi^{(3)}$, except if the SH is in the vicinity of the half-bandgap frequency.

Raman effects of the Kerr SPM term can be modeled by replacing

$$\chi^{(3)}_{\mathrm{SPM}} E_j |E_j|^2 \rightarrow \chi^{(3)}_{\mathrm{SPM}} [(1-f_R) E_j |E_j|^2 + f_R E_j \int_{-\infty}^{\infty} \mathrm{d}\tau' h_R(\tau-\tau') |E_j(\tau')|^2] \tag{2.6}$$

where as usual f_R is the Raman fraction of the nonlinearity and h_R is the temporal normalized Raman response function. The effects of Raman on the XPM terms should also be modeled, see [2], but is not relevant to the analytical approach as the SH field is usually quite weak. Besides, empirical observations show that the Raman effect is quite small in the standard type I crystal we have used, BBO, where these coupled wave equations have been used to model the system numerically. In turn, the Raman effect is quite strong in the main type 0 crystal we have used, $LiNbO_3$, and below in Sec. 2.3 we present a model that models the FW and SH fields in one single equation and where the Raman effects are specifically included without truncation.

We can convert the electric field to intensity $E_j \rightarrow (2/\varepsilon_0 n_j c)^{1/2} A_j$, so $|A_j|^2$ is the intensity in $[\mathrm{W/m^2}]$, and we get

$$\left[i\partial_\zeta + \hat{D}_{\omega_1}\right] A_1 + \hat{S}_1 \kappa^I_{\mathrm{SHG}} A_1^* A_2 e^{i\Delta k \zeta} + \frac{\omega_1}{c}\left[n_2^{\mathrm{SPM}} A_1 |A_1|^2 + 2 n_2^{\mathrm{XPM}} A_1 |A_2|^2\right] = 0 \tag{2.7a}$$

$$\left[i\partial_\zeta - i d_{12}\partial_\tau + \hat{D}_{\omega_2}\right] A_2 + \hat{S}_2 \kappa^I_{\mathrm{SHG}} A_1^2 e^{-i\Delta k \zeta} + \hat{S}_2 \frac{\omega_2}{c}\left[\frac{n_1^2}{n_2^2} n_2^{\mathrm{SPM}} A_2 |A_2|^2 + 2 n_2^{\mathrm{XPM}} A_2 |A_1|^2\right] = 0 \tag{2.7b}$$

where the equations now have a common SHG nonlinear parameter

$$\kappa^I_{\mathrm{SHG}} = \frac{\omega_1 d_{\mathrm{eff}}}{n_1 c}\sqrt{\frac{2}{n_2 \varepsilon_0 c}} \tag{2.8}$$

We can also establish the link between the Kerr nonlinear refractive indices and the cubic nonlinear susceptibilities as

$$n_2^{\mathrm{SPM}} = \frac{3\chi^{(3)}_{\mathrm{SPM}}}{4 n_1^2 \varepsilon_0 c}, \quad n_2^{\mathrm{XPM}} = \frac{3\chi^{(3)}_{\mathrm{XPM}}}{4 n_1 n_2 \varepsilon_0 c} \tag{2.9}$$

cf. also Eq. (C6) in [4]. We keep n_2^{SPM}, n_2^{XPM} and $\chi^{(3)}$ in mks (SI) units, while conversion to and from the esu system is reported in [4].

Note that we here adopt the usual notation for the nonlinear refractive index, where the refractive index perceived by the electromagnetic wave is perturbed from its linear refractive index n_0 according to $n = n_0 + n_2^{\mathrm{SPM}} I$ due to SPM and $n = n_0 + n_2^{\mathrm{XPM}} I$ due to XPM. Here I is the field intensity (in case of SPM the intensity of the field itself, in case of XPM the intensity of the other field). The notation with subscript "2" is historical, referring to the fact that the perturbation to the refractive index is $\propto |E|^2$, and any confusion with the SH linear refractive index n_2 is in this dissertation hopefully removed by specifying in the superscript the SPM and XPM reference.

The coupled SEWA equations with Raman effects were derived in [2] based on [63]. There it was stated that the SH dispersion in the SEWA framework is slightly modified due to the finite GVM parameter. However, later studies (e.g. [94]) of more complete numerical models that can be reduced to the SEWA model do not confirm this modification. This discrepancy remains to be resolved, but empirically the perturbation to the SH dispersion is limited and it therefore seems appropriate to model the SH dispersion directly as indicated in Eq. (2.2).

2.3 The nonlinear analytic envelope equation

Since the nonlinear dynamics we investigate potentially goes to the single-cycle limit, we can always question whether the full SHG coupled wave model is accurate. Even if the extension from the SVEA to the SEWA should give single-cycle accuracy, the use of a nonlinear Schrödinger-like equation is questionable as it only contains the SPM and XPM-like terms $|A|^2A$, and we only basically model the quadratic nonlinearity as a transfer from FW to SH and back, and not specifically SFG and DFG-like fields.

There is therefore motivation to model the full electrical field, without truncating any nonlinear terms and without any bandwidth limitations (for excellent discussions on such issues see [94, 95]). A direct method is to implement a forward-Maxwell equation approach [96, 85]. It quickly turned out that while this approach has an advantage of a simple implementation, it does remain a black-box from a physics point of view. We therefore opted to implement the so-called nonlinear analytic envelope equation (NAEE) [97, 98, 72, 99]. This has the advantage of modeling carrier-wave resolved dynamics while still keeping the envelope-like equations, which is useful for carrying out analytical investigations of phase-matching conditions as we shall see later. For both the forward Maxwell-like equation and the NAEE another advantage is that the third-harmonic wave is modeled automatically, which is convenient because in experiments often the third harmonic is in the visible range and is quite easily seen by the eye.

In a type-0 phase-matching scenario, one usually opts to to maximize d_{eff}, and in a crystal like LN this happens when the crystal is cut for $\theta = \pi/2$. In this case, the input field must be e-polarized and the nonlinear coupling to the o-polarized component is then zero. This means that any harmonic generated by $\chi^{(2)}$ or $\chi^{(3)}$ effects will also be e-polarized. We can therefore model the nonlinear dynamics in the e-polarized pump at frequency ω_1 in a single equation in the moving reference frame $\zeta = z$ and $\tau = t - zk^{(1)}(\omega_1)$ [99]

$$
\begin{aligned}
i\frac{\partial A}{\partial \zeta} + \hat{D}_{\omega_1}A + \tfrac{\omega_1 d_{\mathrm{eff}}}{n(\omega_1)c}\hat{S}_\tau\Big[\tfrac{1}{2}A^2e^{-i\omega_1\tau - i\Delta_{\mathrm{pg}}\zeta} + |A|^2e^{i\omega_1\tau + i\Delta_{\mathrm{pg}}\zeta}\Big]_+ \\
+ \tfrac{3\omega_1\chi^{(3)}_{\mathrm{SPM}}}{8n(\omega_1)c}\hat{S}_\tau\Big[(1-f_R)\left(|A|^2A + |A|^2A^*e^{i2\omega_1\tau + i2\Delta_{\mathrm{pg}}\zeta} + \tfrac{1}{3}A^3e^{-i2\omega_1\tau - i2\Delta_{\mathrm{pg}}\zeta}\right) \\
+ f_R\Big\{\tfrac{1}{2}A(\zeta,\tau)\int_{-\infty}^{\infty}\mathrm{d}\tau' h_R(\tau-\tau')e^{i2\omega_1\tau' + i2\Delta_{\mathrm{pg}}\zeta}A^{*2}(\zeta,\tau') \\
+ \left(A(\zeta,\tau) + A^*(\zeta,\tau)e^{i2\omega_1\tau + i2\Delta_{\mathrm{pg}}\zeta}\right) \\
\times\int_{-\infty}^{\infty}\mathrm{d}\tau' h_R(\tau-\tau')\left(\tfrac{1}{2}A^2(\zeta,\tau')e^{-i2\omega_1\tau' - i2\Delta_{\mathrm{pg}}\zeta} + |A(\zeta,\tau')|^2\right)\Big\}\Big]_+ = 0 \quad (2.10)
\end{aligned}
$$

where A is the electric field envelope in mks units (not to be confused with the normalization chosen previously, where $|A_j|^2$ were the envelope intensities). For notational reasons we have suppressed the dependence of A on ζ and τ except in the Raman part where it is spelled out for clarity. $\hat{S}_\tau = 1 + i\omega_1^{-1}\frac{\partial}{\partial\tau}$ is the self-steepening operator.[2] Concerning dispersion, we are now only modeling a single polarization meaning it suffices to consider a single wavevector $k(\omega) = n(\omega)\omega/c$, and $k^{(m)}(\omega') = \frac{d^m k}{d\omega^m}|_{\omega=\omega'}$ are the higher-order dispersion coefficients. The dispersion operator $\hat{D}_{\omega_1}$ is then identical to Eq. (2.3) by using k instead of k_1.

The peculiar term $\Delta_{\rm pg} = \omega_1 k_1(\omega_1) - k(\omega_1) = \omega_1(1/v_g - 1/v_p)$ accounts for the phase-group-velocity mismatch (carrier-envelope phase slip), where $v_g = 1/k^{(1)}(\omega_1)$ is the pump group velocity and $v_p = c/n(\omega_1)$ is the pump phase velocity. Finally, the $+$ sign implies that only the positive frequency content of the nonlinear term is used [97]; we remind that the analytic field A is defined over the entire frequency range $\omega \in [-\infty, \infty]$.

The NAEE was investigated for $\chi^{(2)}$ [97] and $\chi^{(3)}$ [98], and in [72] a complete equation for $\chi^{(2)}$-$\chi^{(3)}$ dynamics was presented, which unlike the other studies included Raman effects. However, as the cubic nonlinear term does not seem consistent with earlier studies,[3] we recently [99] published the complete $\chi^{(2)}$-$\chi^{(3)}$ NAEE model with no truncation on the Raman terms, which here is represented by Eq. (2.10).

If we now introduce the auxiliary field $a(\zeta,\tau) = A(\zeta,\tau)e^{-i\Delta_{\rm pg}\zeta}$ then the equation simplifies to

$$
\begin{aligned}
i\frac{\partial a}{\partial\zeta} + (\hat{D}_{\omega_1} - \Delta_{\rm pg})a + \tfrac{\omega_1 d_{\rm eff}}{n(\omega_1)c}\hat{S}_\tau\left[\tfrac{1}{2}a^2 e^{-i\omega_1\tau} + |a|^2 e^{i\omega_1\tau}\right]_+ \\
+ \tfrac{3\omega_1\chi^{(3)}_{\rm SPM}}{8n(\omega_1)c}\hat{S}_\tau\Big[(1-f_R)\left(|a|^2 a + |a|^2 a^* e^{i2\omega_1\tau} + \tfrac{1}{3}a^3 e^{-i2\omega_1\tau}\right) \\
+ f_R\Big\{\tfrac{1}{2}a(\zeta,\tau)\int_{-\infty}^{\infty}{\rm d}\tau' h_R(\tau-\tau')e^{i2\omega_1\tau'}a^{*2}(\zeta,\tau') + \left(a(\zeta,\tau) + a^*(\zeta,\tau)e^{i2\omega_1\tau}\right) \\
\times\int_{-\infty}^{\infty}{\rm d}\tau' h_R(\tau-\tau')(\tfrac{1}{2}a^2(\zeta,\tau')e^{-i2\omega_1\tau'} + |a(\zeta,\tau')|^2)\Big\}\Big]_+ = 0 \quad (2.11)
\end{aligned}
$$

This is advantageous to model numerically because the cumbersome update of the phase mismatch in the nonlinear step is moved to the linear dispersion operator.

We note that all nonlinear terms, except the SPM term, have some variant of $e^{i\omega_1\tau}$ multiplied onto them. This gives temporal oscillations on the carrier time scale. This is a consequence of the fact that even if this is an envelope approach, then it is actually the carrier that is modelled. We therefore stress that, e.g., the $A^*Ae^{i\omega_1\tau}$ term should not be confused with optical rectification exactly because the $e^{i\omega_1\tau}$ term is being retained.

We should remind that since we are considering specifically a type-0 interaction here, we know that it is only relevant to consider one $\chi^{(3)}$ value, which as was noted in [99] is exactly the one measured by SPM, i.e. $\chi^{(3)}_{\rm SPM}$. In contrast in the coupled wave equation

[2] As noted by Conforti et al. [98] and Kinsler [94], this is an approximation in time domain to the more accurate form in frequency domain ω^2/c^2. Specifically when ω^2/c^2 is expanded around ω_1 it gives $\omega^2/c^2 = \omega_1^2/c^2(1+2\Delta+\Delta^2) \simeq \omega_1^2/c^2(1+2\Delta)$, which in time domain gives the traditional self steepening operator.

[3] They use $P^{(3)}_{\rm NL} \propto E\int{\rm d}t' R(t-t')|E(t')|^2$, instead of the full expansion $P^{(3)}_{\rm NL} \propto E\int{\rm d}t' R(t-t')E^2(t')$. Here the usual response function for taking into account electronic and vibrational nonlinear effects is $R(t) = (1-f_R)\delta(t) + f_R h_R(t)$.

case in Sec. 2.2 we had to distinguish specifically between SPM and XPM as we had to allow for the SH to have a different polarization than the FW.

If we should extend the NAEE case to type I phase matching, we would have to extend the single-equation model to a coupled-equations model (one wave for each polarization state). This has been done for quadratic nonlinearities [100] but has not yet been extended to cubic nonlinearities; especially the Raman terms would be rather involved. Therefore it might be more straightforward to implement such a scheme in the forward-Maxwell kind of approach, like we recently did [85].

Chapter 3

Cascaded quadratic nonlinearities

You're a conductor
A simple conductor
The electricity just
Pouring through me

We Were Promised Jetpacks "Conductor"

Here I show the basic properties of cascaded SHG, with particular focus on the temporal aspects for ultrafast femtosecond interaction.

3.1 Cascaded Kerr-like nonlinearity

We start with the simple SHG coupled wave equations (2.1). Let us first consider the system in absence of SH dispersion, i.e. in the long-pulse limit. With this assumption we can drop the temporal dispersion terms of the SH equation. This can be justified by considering that under a heavily phase-mismatched SHG process ($|\Delta k|L \gg 2\pi$), the coherence length of the SHG $l_{\text{coh}} = \pi/|\Delta k|$ is much shorter than the characteristic dispersion length scales. This allows using the ansatz

$$E_2^{\text{nl}}(\zeta) = e_2 e^{-i\Delta k\zeta} \tag{3.1}$$

Inserting the ansatz in Eq. (2.1b) gives the connection

$$e_2 = -\frac{\omega_1 d_{\text{eff}}}{c n_2 \Delta k} E_1^2 \tag{3.2}$$

Using then the relation Eq. (3.1) and inserting $E_2^{\text{nl}}(\zeta)$ into Eq. (2.1a) in place of E_2 we get the NLS-like equation

$$\left[i\tfrac{\partial}{\partial\zeta} - \tfrac{1}{2}k_1^{(2)}\tfrac{\partial^2}{\partial\tau^2} \right] E_1 + \tfrac{3\omega_1}{8n_1 c}\chi_{\text{casc}}^{(3)}|E_1|^2 E_1 = 0 \tag{3.3}$$

where

$$\chi_{\text{casc}}^{(3)} = -\frac{8\omega_1}{3cn_2}\frac{d_{\text{eff}}^2}{\Delta k}, \quad n_2^{\text{casc}} = -\frac{2\omega_1 d_{\text{eff}}^2}{c^2\varepsilon_0 n_1^2 n_2 \Delta k} \tag{3.4}$$

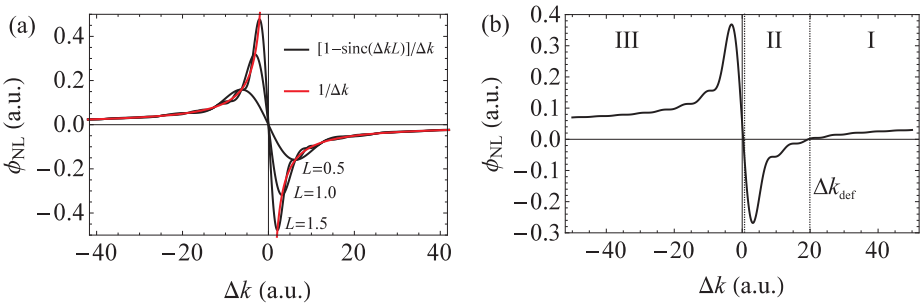

Figure 3.1: (a) Cascaded nonlinear phase shift vs. phase mismatch parameter Δk. The simple expression $\phi_{\mathrm{NL}} \propto -1/\Delta k$ is compared to the more accurate expression $\phi_{\mathrm{NL}} \propto -[1-\mathrm{sinc}(\Delta kL)]/\Delta k$, shown for three different values of L. The maximum nonlinearity is found when $\Delta kL \simeq \pi$; remark how the simple $-1/\Delta k$ expression is able to track this peak nonlinearity despite not being strictly valid in this limit. (b) The net nonlinear phase shift in presence of a constant focusing Kerr nonlinearity. In regions I and III the net nonlinear phase shift is focusing, while in region II it is defocusing.

The cascaded nonlinearity is here expressed in two equivalent ways, either as a cubic nonlinear susceptibility $\chi^{(3)}_{\mathrm{casc}}$ or as a nonlinear refractive index n_2^{casc} (cf. Sec. 2.2).

The seminal result appearing immediately from this simple ansatz is therefore [15]

- The cascaded nonlinearity invokes a Kerr-like nonlinearity on the FW
- Its nonlinear strength is proportional to the square of the quadratic nonlinearity and inversely proportional to the SHG phase mismatch
- Its sign can be controlled by the sign of the phase mismatch. For $\Delta k > 0$ it is self-defocusing, while for $\Delta k < 0$ it is self-focusing.

This Kerr-like nonlinearity will then induce self-phase modulation (SPM) on the FW. Through the phase mismatch parameter we can control the sign and strength of the nonlinearity of the system.

This simple result is alluring: a phase-mismatched SHG crystal can give incredibly strong nonlinear phase shifts (since $\phi_{\mathrm{NL}} \propto 1/\Delta k$) and it can at will access self-focusing and self-defocusing effects. However, competing and higher-order effects set limits to what we can actually access. Specifically

- The result only holds for $|\Delta k|L \gg 2\pi$. Since nonlinear crystals have finite lengths, typically a few centimeters, this result does not hold in the limit where Δk is very small.
- For $|\Delta k|L \simeq 2\pi$ or smaller, we may use the more accurate cascaded nonlinearity $\phi_{\mathrm{NL}} \propto -[1-\mathrm{sinc}(\Delta kL)]d_{\mathrm{eff}}^2/\Delta k$, which resolves the spurious divergence at $\Delta k = 0$. This expression can be derived under the assumption of an undepleted FW. The expression is more accurate, but the disadvantage is that it is not independent of the length of the sample, cf. Fig. 3.1.

- Since the leading cascading nonlinearity is cubic, it will compete with the intrinsic material Kerr nonlinearity. This is treated in Sec. 3.1.1, and is visualized in Fig. 3.1(b).
- Apart from competing with the leading-order material cubic nonlinearity, cascading also induces higher-order nonlinearities (quintic and beyond, cf. Sec. 3.1.2) as well as self-steepening effects (cf. Sec. 3.3).
- When including temporal dispersion of the SH, the cascading response is no longer simply a Kerr response but becomes a *nonlocal* response. This is treated in Sec. 3.2

3.1.1 Competing material Kerr effect

While only some (non-centrosymmetric) materials have a quadratic nonlinearity, all materials have a cubic nonlinearity. When we operate the nonlinear crystal in the cascading limit, this material nonlinearity will compete directly with the cascading Kerr-like nonlinearity. This gives the nonlinear Schrödinger equation (NLSE)

$$\left[i\frac{\partial}{\partial\zeta} - \tfrac{1}{2}k_1^{(2)}\frac{\partial^2}{\partial\tau^2}\right]E_1 + \tfrac{3\omega_1}{8n_1c}\left[\chi^{(3)}_{\text{casc}} + \chi^{(3)}_{\text{SPM}}\right]E_1|E_1|^2 = 0 \tag{3.5}$$

where $\chi^{(3)}_{\text{SPM}}$ is the effective cubic nonlinearity related to self-phase modulation (SPM). We can see that the total nonlinearity is $\chi^{(3)}_{\text{tot}} = \chi^{(3)}_{\text{casc}} + \chi^{(3)}_{\text{SPM}}$. Using the intensity scaling we therefore have the NLSE

$$\left[i\frac{\partial}{\partial\zeta} - \tfrac{1}{2}k_1^{(2)}\frac{\partial^2}{\partial\tau^2}\right]A_1 + \tfrac{\omega_1}{c}n_2^{\text{tot}}A_1|A_1|^2 = 0, \quad n_2^{\text{tot}} = n_2^{\text{casc}} + n_2^{\text{SPM}} \tag{3.6}$$

The cascading nonlinearity is seen to compete directly with the material nonlinearity. This is remarkable because essentially by phase-mismatching the quadratic nonlinearity we create an effective cubic nonlinearity that can manipulate with the next-order nonlinearity present in the system (the Kerr effect), even canceling it [56, 8]. Usually, though, the cascading nonlinearity is used to flip the sign of the material cubic nonlinearity from positive to negative, thus operating at a finite, negative nonlinearity. Coming back to Fig. 3.1, (b) shows the net nonlinear phase shift vs. phase mismatch parameter in presence of a finite focusing Kerr SPM nonlinearity. Regions I and III are focusing, while in region II the net nonlinearity is defocusing. Right at the interface between I and II the net SPM cancels; this critical phase-mismatch value for achieving defocusing is later designated Δk_{def}.

3.1.2 Higher-order cascading effects

While cascading can lead to cancellation of the material Kerr effect, it does not mean the system becomes linear. In fact, cascading also leads to self-steepening effects [56] as well as quintic [2, 8] and ultimately also an infinite series of higher-order terms [17] (although quickly these terms become less and less significant). The next-order terms modify the NLSE as

$$\left[i\frac{\partial}{\partial\zeta} - \tfrac{1}{2}k_1^{(2)}\frac{\partial^2}{\partial\tau^2}\right]E_1 + \tfrac{3\omega_1}{8n_1c}\left[\chi^{(3)}_{\text{casc}} + \chi^{(3)}_{\text{SPM}}\right]E_1|E_1|^2 + \tfrac{5\omega_1}{16n_1c}\chi^{(5)}_{\text{casc}}E_1|E_1|^4 = \\ -i\tfrac{3\omega_1}{8n_1c}\chi^{(3)}_{\text{casc}}\tfrac{2d_{12}}{\Delta k}|E_1|^2\partial_\tau E_1 \tag{3.7}$$

We see that on the left-hand side a quintic nonlinear term appears, arising due to cross-phase modulation (XPM) through the material cubic nonlinearity between the FW and the SH. Its strength is given by

$$\chi^{(5)}_{\text{casc}} = \frac{12\omega_1^2}{5n_2^2c^2}\frac{\chi^{(3)}_{\text{XPM}}d_{\text{eff}}^2}{\Delta k^2}, \quad n_4^{\text{casc}} = \frac{4\omega_1^2}{\varepsilon_0 c^3 n_1^2 n_2}\frac{n_2^{\text{XPM}}d_{\text{eff}}^2}{\Delta k^2} \tag{3.8}$$

where $\chi^{(3)}_{\text{XPM}}$ is the effective nonlinearity controlling XPM between the FW and the SH [8]. Equivalently n_4^{casc} is the next-order contribution from cascading to the nonlinear refractive index, defined through $\Delta n = (n_2^{\text{casc}} + n_2^{\text{SPM}})I + n_4^{\text{casc}}I^2$.

On the right-hand side (RHS) we find a a nonlinear time-derivative term. Initially it was compared to a Raman-like effect [61], a nomenclature we also adopted early on, but later it turned out to be more accurately be described as a contribution from cascading to self-steepening [63]. It is also intimately connected with the so-called nonlocal response discussed in Sec. 3.2. We note also that this term on the RHS is only one of several terms to this order, and to do a complete analysis one must also include similar terms from "material" self-steepening as well as lowest-order terms from delayed Raman effects. This will be discussed more in Sec. 3.3.

3.2 Nonlocal cascading response

The nonlocal theory is basically the standard cascading result that we have just derived, but where we now take into account that the waves are pulsed and thus dispersion becomes important.

The nonlocal theory builds on the approach used in [1]. We first assume a heavily phase-mismatched SHG process ($|\Delta k|L \gg 2\pi$), allowing for the ansatz

$$E_2^{\text{nl}}(\zeta,\tau) = e_2(\tau)e^{-i\Delta k\zeta} \tag{3.9}$$

that separates the ζ and τ dependence. Inserting the ansatz in Eq. (2.1b) gives the ordinary differential equation

$$\Delta k e_2(\tau) - id_{12}e_2'(\tau) - \tfrac{1}{2}k_2^{(2)}e_2''(\tau) + \tfrac{\omega_1 d_{\text{eff}}}{cn_2}E_1^2 = 0, \tag{3.10}$$

where primes denote time derivatives. Introducing the Fourier transform

$$E_2(\zeta,\Omega) = (2\pi)^{-1/2}\int_{-\infty}^{\infty} \mathrm{d}\Omega e^{+i\Omega\tau}E_2(\zeta,\tau) \tag{3.11}$$

in Fourier domain we get $e_2(\Omega)\left[\Delta k - d_{12}\Omega + \frac{1}{2}k_2^{(2)}\Omega^2\right] + \frac{\omega_1 d_{\text{eff}}}{cn_2}\mathscr{F}[E_1^2] = 0$, implying the solution

$$E_2^{\text{nl}}(\zeta,\Omega) = -e^{-i\Delta k\zeta}\sqrt{2\pi}\frac{\omega_1 d_{\text{eff}}}{cn_2\Delta k}R_{\text{casc}}(\Omega)\mathscr{F}[E_1^2] \tag{3.12}$$

where $\mathscr{F}[\cdot]$ denotes the forward Fourier transform, and we used Eq. (3.9). A normalized nonlocal response function is here introduced as

$$\tilde{R}_{\text{casc}}(\Omega) = \frac{1}{\sqrt{2\pi}}\frac{\Delta k}{\frac{1}{2}k_2^{(2)}\Omega^2 - d_{12}\Omega + \Delta k} \tag{3.13}$$

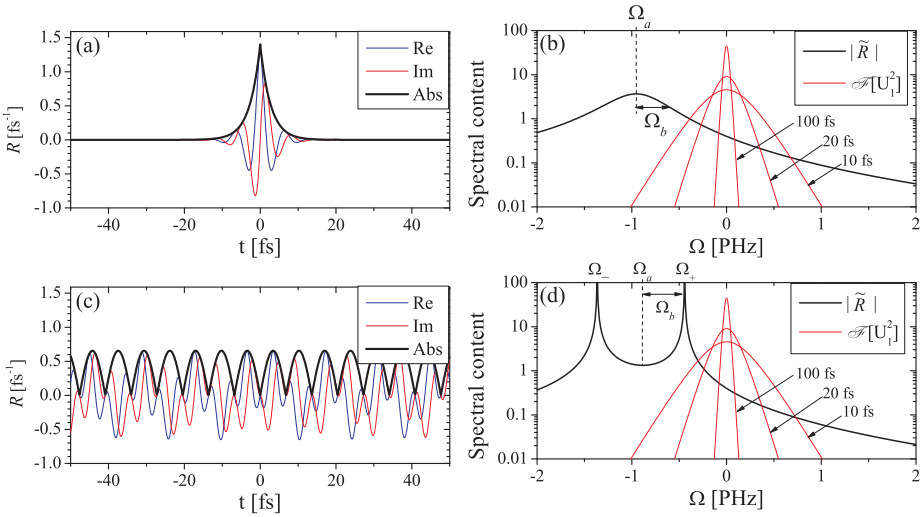

Figure 3.2: The nonlocal response functions in the (a,b) non-resonant case and (c,d) resonant case. The spectral content of $\mathrm{sech}^2(t/T_0)$ having 100, 20, and 10 fs FWHM duration is shown in (b,d). This figure was published in [3].

which turns out to be inherently dimensionless. The factor $\sqrt{2\pi}$ is precisely the factor required for the equivalent temporal response function to be normalized appropriately: this conveniently gives $\int_{-\infty}^{\infty} d\tau R_{\mathrm{casc}}(\tau) = 1$.

We see from Eq. (3.12) that the SH becomes "slaved" to the FW (the term "driven" wave has also been used): The SH spectral density for a transform-limited FW is therefore $I_2(\Omega) \propto |\tilde{R}_{\mathrm{casc}}(\Omega)|^2 I_1^2(\Omega)$. For a chirped FW the relation becomes more complicated ($|\mathscr{F}[E_1]^2| \neq |E_1(\Omega)|^2$), and one can no longer simply consider SH spectrum as a product of the FW spectral intensity and the nonlocal response function.

The denominator of the nonlocal response can become resonant when $\Delta k < \Delta k_{\mathrm{r}}$, where the phase-mismatch parameter for entering the resonant regime is

$$\Delta k_{\mathrm{r}} \equiv \frac{d_{12}^2}{2k_2^{(2)}} \tag{3.14}$$

It is an important phase-mismatch value that depends critically on the GVM parameter d_{12}. It marks the threshold between the non-resonant ($\Delta k > \Delta k_{\mathrm{r}}$) and resonant regimes $\Delta k < \Delta k_{\mathrm{r}}$. In the latter the resonant nonlocal behavior occurs because denominator will have two real roots, leading to resonant peaks in R_{casc}. These resonance frequencies are to 2. order

$$\Omega_{\pm} = \left(d_{12} \pm \sqrt{d_{12}^2 - 2\Delta k k_2^{(2)}} \right) / k_2^{(2)} \tag{3.15}$$

This result was also found in [71] using a different approach, but essentially taking the same key assumptions. Instead when $\Delta k > \Delta k_{\mathrm{r}}$ the nonlocal response is non-resonant:

the resonance peaks disappears and the nonlocal response is ultrabroadband. This is the optimal situation for few-cycle pulse compression as we discuss in Sec. 5.2. In Fig. 3.2 we show the typical temporal and spectral contents of the resonant and non-resonant nonlocal response functions as calculated for BBO at $\lambda_1 = 1.064\ \mu$m [3, Fig. 2].

Before discussing this figure in detail, we note that the nonlocal response is essentially a Lorentzian function (at least when only 2. order dispersion is considered) that can be written as

$$\tilde{R}_{\text{casc}}(\Omega) = (2\pi)^{-\frac{1}{2}} \frac{\Omega_a^2 + \Omega_b^2}{(\Omega - \Omega_a)^2 \pm \Omega_b^2} \tag{3.16}$$

with '+' corresponding to $\Delta k > \Delta k_{\text{r}}$ and '−' corresponding to $\Delta k < \Delta k_{\text{r}}$. The center of the Lorentzian Ω_a and its width Ω_b are given by $\Omega_\pm = \Omega_a \pm \Omega_b$, so

$$\Omega_a = d_{12}/k_2^{(2)}, \quad \Omega_b = |2\Delta k/k_2^{(2)} - \Omega_a^2|^{\frac{1}{2}} \tag{3.17}$$

The frequency domain response function also has an associated time domain expression

$$R_{\text{casc}}(\tau) = \frac{\Omega_a^2 + \Omega_b^2}{2\Omega_b} e^{-i\Omega_a\tau - \Omega_b|\tau|}, \quad \Delta k > \Delta k_{\text{r}} \tag{3.18}$$

$$R_{\text{casc}}(\tau) = \frac{\Omega_a^2 - \Omega_b^2}{2\Omega_b} e^{-i\Omega_a\tau} \sin(\Omega_b|\tau|), \quad \Delta k < \Delta k_{\text{r}} \tag{3.19}$$

These expressions are also plotted for each case in Fig. 3.2. One important observation is that in the resonant regime the nonlocal "gain" in the SH spectrum is related to the spectral strength of $\mathscr{F}[U_1^2]$ at that sideband frequency. Thus the resonant peaks in the SH spectrum do not appear unless the FW is very broadband (as indicated by the spectral contents of several ultra-short FW pulses). It is worth remarking that Ω_a is the critical constant controlled by GVM and that explicitly enters, e.g., the self-steepening formulas Eq. (3.31). Here it is related to the phase of the nonlocal response, and consequently we can connect the phase of the nonlocal response function to self-steepening. As we will see later the amplitude, related to Ω_b is in turn related to the soliton width. We finally remark that $\Omega_a = 0$ in absence of GVM ($d_{12} = 0$), in which case we also have $\Delta k_{\text{r}} = 0$, i.e. that the entire defocusing range is nonresonant.

The analysis so far has focused on the simple case where only SH GVD is included, but in a realistic system the entire dispersion profile must be considered. It is easy to see that the nonlocal response function (3.13) generalizes to[1]

$$\tilde{R}_{\text{casc}}(\Omega) = \frac{1}{\sqrt{2\pi}} \frac{\Delta k}{\tilde{D}_{\omega_2}(\omega_2 + \Omega) - d_{12}\Omega + \Delta k} = \frac{1}{\sqrt{2\pi}} \frac{\Delta k}{k_2(\omega_2 + \Omega) - \Omega k_1^{(1)} - 2k_1^{(0)}} \tag{3.20}$$

This changes the resonance threshold and the resonant frequencies, which no longer can be calculated analytically.

The ansatz Eq. (3.9) reflects the strong cascading limit ($|\Delta k|L \gg 2\pi$), where it is assumed that the phase-mismatch is so large that the coherence length $\pi/|\Delta k|$ is much

[1] Note that in the caption of Fig. 1 in [7] the expression for the full SH dispersion has a typo and should be replaced with Eq. (3.20).

smaller than any other characteristic length scales (see also discussion in [1]). However, it turns out to work quite very well even when one of the other length scales become similar in size. An important length scale in this comparison is the quadratic nonlinear length scale defined through the traditional Γ-parameter

$$\Gamma = \frac{\omega_1 d_{\text{eff}} E_{1,\text{in}}}{c\sqrt{n_1 n_2}} \tag{3.21}$$

where $E_{1,\text{in}}$ is the peak electric input field. The ansatz holds when $\Delta k \Gamma \gg 1$ [8]. The ansatz looks for solutions that are stationary in ζ, and this only happens when the FW can be assumed undepleted, but also when the FW phase does not change with ζ; remember from Eq. (3.12), where the "source term" $\mathscr{F}[E_1^2]$ is assumed constant in ζ and therefore should not induce SH variations in ζ either through its amplitude or phase.

However, we shall later discuss the nonlocal results in the specific case where the FW is a temporal soliton with the solution Eq. (5.5). In this case we know precisely how the FW behaves, as the soliton solution is $E_1(\zeta,\tau) \propto \operatorname{sech}(\tau/T_0)e^{iq_{\text{sol}}\zeta}$: it will not disperse, its temporal profile will be $\propto \operatorname{sech}(\tau/T_0)$ and it has a nonlinear phase due to the term $e^{iq_{\text{sol}}\zeta}$. This ζ dependence gives a deterministic contribution to the phase-mismatch condition $\Delta k \to \Delta k - 2q_{\text{sol}}$. We essentially have to modify the SH ansatz (3.9) to be $E_2(\zeta,\tau) = e_2(\tau)e^{-i(\Delta k - 2q_{\text{sol}})\zeta}$ and the nonlocal response is modified as follows

$$\tilde{R}_{\text{casc}}(\Omega) = \frac{1}{\sqrt{2\pi}} \frac{\Delta k}{\tilde{D}_{\omega_2}(\omega_2+\Omega) - d_{12}\Omega + \Delta k - 2q_{\text{sol}}} \tag{3.22}$$

This also means that the transition to the resonant regime is modified accordingly, and that the phase-matched resonant radiation frequencies (ω_{RR}) are found in the resonant regime by solving the equation

$$\tilde{D}_{\omega_2}(\omega_{\text{RR}}) - d_{12}(\omega_{\text{RR}} - \omega_2) + \Delta k = 2q_{\text{sol}} \tag{3.23}$$

We shall see later in Sec. 6.4 that this is precisely the phase-matching condition for observing soliton-induced resonant radiation through the SHG term, cf. Eq. (6.21).

The simulation in Fig. 3.3 shows a typical simulation in the resonant regime, where the intensity is large enough to excite a defocusing soliton in the FW. Looking at the SH time trace we see initially both the free wave, walking away from the FW due to GVM, and the driven wave, locked to the FW group velocity. After 10 mm the nonlocal radiation shows up, which coincides perfectly with the soliton forming. Thus, its origin is solitonic. The radiation is dispersive and it walks away from the soliton. In the SH spectrum we clearly see the radiation peak, and it overlaps very precisely with the predicted resonance (0.595 μm using the contribution from q_{sol}, dashed gray line).

Let us now show how the cascading leads to a nonlocal Kerr-like nonlinearity: Using the convolution theorem $E_2(\zeta,\tau) = -e^{-i\Delta k\zeta}\frac{\omega_1 d_{\text{eff}}}{cn_2\Delta k}\int_{-\infty}^{\infty} \mathrm{d}s R_{\text{casc}}(s)E_1^2(\zeta,\tau-s)$, where $R_{\text{casc}}(\tau) = \mathscr{F}^{-1}[\tilde{R}_{\text{casc}}]$ is the inverse Fourier transform of the response function. Inserting $E_2(\zeta,\tau)$ into Eq. (2.1a), we get that the FW obeys the following equation

$$\left[i\frac{\partial}{\partial\zeta} - \frac{k_1^{(2)}}{2}\frac{\partial^2}{\partial\tau^2}\right]E_1 + \frac{3\omega_1}{8n_1c}\chi^{(3)}_{\text{casc}}E_1^*\int_{-\infty}^{\infty}\mathrm{d}s R_{\text{casc}}(s)E_1^2(\zeta,\tau-s) = 0. \tag{3.24}$$

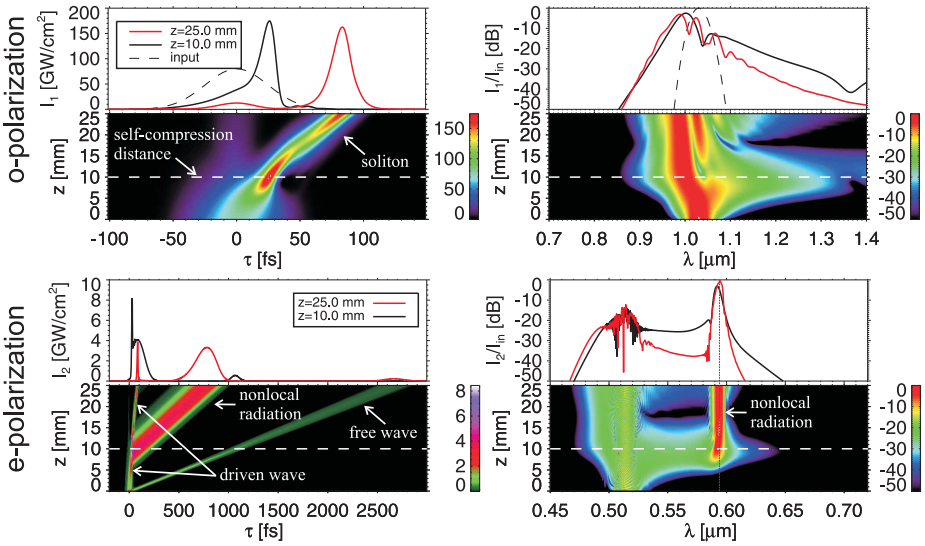

Figure 3.3: Numerical simulation of an $L = 25$ mm BBO crystal pumped with $\lambda_1 = 1.03$ μm 58 fs FWHM 80 GW/cm^2 pulses. The simulations are based on the SEWA equations using experimental parameters of the $+3°$-case of the experiment in [10], which corresponds to $\Delta k = 35$ mm^{-1}, well into the resonant regime as $\Delta k_r = 52$ mm^{-1} at this pump wavelength. Taken from [10].

The leading nonlinearity $\chi^{(3)}_{\rm casc}$ is cubic, and is equivalent to Eq. (3.4). This nonlocal Kerr-like nonlinearity is non-resonant in frequency domain when $\Delta k > \Delta k_r$ and resonant in frequency domain when $\Delta k < \Delta k_r$. Finally, in the local limit where the FW spectrum is very narrow we can make the approximation that $\tilde{R}(\Omega)$ is constant inside the spectrum, and thus $E_1^*(\zeta,\tau)\int_{-\infty}^{\infty} {\rm d}s R_{\rm casc}(s)E_1^2(\zeta,\tau-s) \simeq E_1(\zeta,\tau)|E_1(\zeta,\tau)|^2$. This is the instantaneous Kerr-like nonlinearity induced by cascading, cf. Eq. (3.3). In Sec. 3.3 we will further show that when including the next order in the local-limit expansion an additional cascading-induced self-steepening term results, equivalent to the term found in [61, 63, 56] using a perturbative approach.

3.3 Cascading and self-steepening effects

We here discuss how higher-order nonlinear terms from cascading and cubic nonlinearities affect the nonlinear dynamics. This was first addressed by the Wise group [61, 63, 56], relating the cascading effects to self-steepening. Our contributions took starting point in the nonlocal theory: we showed that the first-order expansion of the nonlocal convolution term was a time-derivative reminiscent of that seen in the Raman effect [1, 3], in line with the early observations of the Wise group [61]. Later we included also the role of the Raman effects [85], and through this it became clear that the cascading effect indeed is a self-steepening like effect in line with what [63, 56] had shown. This also corroborated the nonlocal approach giving the same result as the perturbative approach of [61, 63, 56].

Let us start by the using the SEWA equations (2.7). We then adopt the cascading ansatz (3.9) for the SH Eq. (2.7b), solve the ODE much as in Eq. (3.12) by neglecting

cubic nonlinearities but retaining self-steepening on the quadratic nonlinearity. Inserting this into the FW Eq. (2.7a), where XPM is neglected by Raman effects are included on the SPM term, we get

$$(i\partial_\zeta + \hat{D}_{\omega_1})A_1 + \hat{S}_1 \tfrac{\omega_1}{c} n_2^{\text{casc}} A_1^*(\tau)\hat{S}_2 \int_{-\infty}^{\infty} \mathrm{d}t' R_{\text{casc}}(t') A_1^2(\tau - t') + \hat{S}_1 \tfrac{\omega_1}{c} n_2^{\text{SPM}} A_1(\tau) \int \mathrm{d}t' R_{\text{Kerr}}(t') |A_1(\tau - t')|^2 = 0 \quad (3.25)$$

We now adopt the usual response function for the Kerr effect $R_{\text{Kerr}}(\tau) = (1 - f_R)\delta(\tau) + f_R h_R(\tau)$, which separates the instantaneous from the vibrational nonlinearity. The normalized Raman response function for the vibrational nonlinear effects is in frequency domain given by $\tilde{h}_R$, which for a single Raman line with resonance frequency ω_σ and damping rate Γ_σ it can be modeled by a Lorentzian

$$\tilde{h}_R(\Omega) = \frac{\omega_\sigma^2}{\omega_\sigma^2 - i\Gamma_\sigma \Omega - \Omega^2} \quad (3.26)$$

In frequency domain it is inherently dimensionless. We then get the time domain version as $h_R(t) = \mathscr{F}^{-1}[\tilde{h}_R(\Omega)]$.

We can now approximate the cascading convolution as follows

$$\begin{aligned} \int \mathrm{d}t' R_{\text{casc}}(t') A_1^2(\tau - t') &= \mathscr{F}^{-1}[\tilde{R}_{\text{casc}}(\Omega)\mathscr{F}[A_1^2(\tau)]] \\ &\simeq \mathscr{F}^{-1}[\{\tilde{R}_{\text{casc}}(0) + \Omega \tfrac{d\tilde{R}_{\text{casc}}}{d\Omega}|_{\Omega=0}\}\mathscr{F}[A_1^2(\tau)]] \\ &= \{1 + i\partial_\tau \tfrac{d\tilde{R}_{\text{casc}}}{d\Omega}|_{\Omega=0}\}A_1^2(\tau) \\ &= \{1 + i\tfrac{d_{12}}{\Delta k}\partial_\tau\}A_1^2(\tau) \end{aligned} \quad (3.27)$$

where we have used the Fourier transform property

$$i\frac{df(\tau)}{d\tau} \leftrightarrow \Omega \tilde{f}(\Omega)$$

and that $\frac{d\tilde{R}_{\text{casc}}}{d\Omega}|_{\Omega=0} = \frac{d_{12}}{\Delta k}$. In the same way

$$\int \mathrm{d}t' h_R(t')|A_1(\tau - t')| \simeq (1 - \tfrac{\Gamma_\sigma}{\omega_\sigma^2}\partial_\tau)|A_1(\tau)|^2 \quad (3.28)$$

We now invoke the self-steepening operators and keep only terms up the first time derivative. This gives the NLSE

$$\begin{aligned} (i\partial_\zeta + \hat{D}_{\omega_1})A_1 + \frac{\omega_1}{c}\left(n_2^{\text{casc}} + n_2^{\text{SPM}}\right)A_1|A_1|^2 \\ + \frac{\omega_1}{c}A_1^2\frac{\partial A_1^*}{\partial \tau}\left(n_2^{\text{casc}}\frac{i}{\omega_1} + n_2^{\text{SPM}}\left[\frac{i}{\omega_1} - \tau_R\right]\right) \\ + \frac{\omega_1}{c}|A_1|^2\frac{\partial A_1}{\partial \tau}\left(n_2^{\text{casc}} i\left[\frac{3}{\omega_1} + \frac{2d_{12}}{\Delta k}\right] + n_2^{\text{SPM}}\left[\frac{2i}{\omega_1} - \tau_R\right]\right) = 0 \end{aligned} \quad (3.29)$$

where $\tau_R \equiv f_R\Gamma_\sigma/\omega_\sigma^2$ is the usual characteristic Raman time. This equation is equivalent of that derived in [63], except that it also contains the Raman term. In the first line we find

the basic NLSE in absence of self-steepening with a total nonlinearity $n_2^{\text{casc}} + n_2^{\text{SPM}}$. In the 2. and 3. line we find the self-steepening and Raman terms. We kept all terms originating from direct self-steepening as $\frac{1}{\omega_1}$ so the origin is clear. The analysis becomes clearer when we invoke the ansatz $A = \sqrt{I}e^{i\phi}$, which means that when neglecting dispersion the NLSE can be split up into intensity and phase

$$\partial_\zeta I + \tfrac{\omega_1}{c} n_2^{\text{SS},I} I \partial_\tau I = 0 \tag{3.30a}$$

$$\partial_\zeta \phi + \tfrac{\omega_1}{c} n_2^{\text{SS},\phi} I \partial_\tau \phi + \tau_R \partial_\tau I = \tfrac{\omega_1}{c} \left(n_2^{\text{casc}} + n_2^{\text{SPM}} \right) I \tag{3.30b}$$

where we have introduced the self-steepening nonlinear parameters for the intensity (I) and phase (ϕ) equations as

$$n_2^{\text{SS},I} = 2n_2^{\text{casc}} \left(\frac{2}{\omega_1} + \frac{d_{12}}{\Delta k} \right) + n_2^{\text{SPM}} \frac{3}{\omega_1} = 3n_2^{\text{tot}} \frac{1}{\omega_1} + n_2^{\text{casc}} \left(\frac{1}{\omega_1} + \frac{d_{12}}{\Delta k} \right) \tag{3.31a}$$

$$n_2^{\text{SS},\phi} = 2n_2^{\text{casc}} \left(\frac{1}{\omega_1} + \frac{d_{12}}{\Delta k} \right) + n_2^{\text{SPM}} \frac{1}{\omega_1} = n_2^{\text{tot}} \frac{1}{\omega_1} + n_2^{\text{casc}} \left(\frac{1}{\omega_1} + \frac{d_{12}}{\Delta k} \right) \tag{3.31b}$$

where $n_2^{\text{tot}} = n_2^{\text{casc}} + n_2^{\text{SPM}}$ is the total SPM experienced by the FW.

We remark the following from this analysis

- As this approach separates the intensity dynamics completely from the phase, this means Eq. (3.30a) can be solved independently. The implicit solution shows that the equation governs the shock-front dynamics in time domain (see e.g. [101]).
- Instead, the phase equation (3.30b) cannot be solved analytically, but it suffices to state that without the Raman term it essentially describes the asymmetric spectrum associated with self-steepening. In absence of self-steepening SPM broadening is namely symmetric in frequency domain, but self-steepening breaks this symmetry: the red ($n_2^{\text{SS},\phi} > 0$) or the blue ($n_2^{\text{SS},\phi} < 0$) side will be favored depending on the sign of Eq. (3.31b).
- The cascading contributions to the dynamics can be be seen to purely add to the self-steepening coefficients Eq. (3.31).
- Essentially we observe two types of cascading contributions:
  - One that stems from the self-steepening terms in front of the quadratic nonlinear terms in the NLSE (the terms $\propto \omega_1^{-1}$).
  - One that is related to GVM and phase mismatch (the terms $\propto d_{12}/\Delta k$). This last term is the controllable self-steepening term [63], where we through manipulation of Δk and GVM can modify the total self-steepening of the system, and this gives control over the spectral asymmetry through cascading. This was demonstrated in the seminal experiment by Moses and Wise [63]. Note, however, that since they did not write up the intensity and phase equations, they proposed to directly manipulate the term for $|A_1|^2 \frac{\partial A_1}{\partial \tau}$ in the NLSE (3.29), i.e. the third line there, but as the analysis here shows it is more accurate to talk about reversing the sign of $n_2^{\text{SS},\phi}$.

- The Raman effect only enters the phase equation (3.30b). This makes sense since the Raman effect is not related to shock-front dynamics, via the intensity equation (3.30a), but rather is known to induce red-shifting of intense pulses.

- Cascading does not give any contributions to the Raman term related to $\partial_\tau I$. This corrects misleading statements in the early literature [61] that the first-order cascading contribution from cascading (beyond SPM) was a Raman-like effect: This result came about from investigating the cascading NLSE without self-steepening, see Eq. (3.7), where a Raman-like first-order term is seen on the right-hand side. Through the detailed analysis shown here, we now see that (a) there are more cascading terms than the one shown there (essentially this was the GVM term alone), and (b) cascading contributes to self-steepening.

- The right-hand side of the phase equation (3.30b) is the SPM term; for a transform-limited pulse (where $\partial_\tau \phi = 0$) and in absence of Raman, this is the classical result that the phase profile due to SPM solves to be $\phi(\tau) \propto I(\tau)$. In presence of Raman we have an additional contribution $\tau_R \partial_\tau I$ that can be shown to lead to red-shift of the pulse center frequency (see e.g. [101]).

- Since we can manipulate the total SPM, we can also make it zero, $n_2^{\mathrm{tot}} = n_2^{\mathrm{casc}} + n_2^{\mathrm{SPM}} = 0$. In fact, this is the special case where the cascading SPM exactly cancels the material Kerr SPM, i.e. where $n_2^{\mathrm{casc}} = -n_2^{\mathrm{SPM}}$. While this also cancels the material self-steepening, the total self-steepening is not canceled: in fact, the intensity nonlinearity becomes $n_2^{\mathrm{SS},I} = n_2^{\mathrm{casc}} \left(\omega_1^{-1} + d_{12}/\Delta k\right)$. Thus, the cascading may eliminate SPM, but it will still give self-steepening to the pulse. This was exploited by Moses and Wise [29].

- A part from reversing the spectral asymmetry and canceling SPM to see SPM-free self-steepening, it is clear that assessing the self-steepening impact is an important consideration when choosing the proper phase-mismatch parameter to work with in a given cascading application. In some cases, one may even see a complete cancellation of the self-steepening coefficients (either one or the other, never both), which requires that $d_{12}/\Delta k > 0$.

Chapter 4

Nonlinear crystals

Life is a waterfall
We drink from the river
Then we turn around and put up our walls

System Of A Down “Aerials”

Here I present some of the results of our investigations into the nonlinear parameters of the crystals we have used. I mainly discuss beta-barium-borate (β-BaB_2O_4, BBO) and type 0 crystals similar to lithium niobate ($LiNbO_3$, LN). Note that I have co-authored an e-print review of LN material parameters [90], but I have not contributed directly to any of the measurements there.

4.1 Cascaded nonlinearities: critical vs noncritical phase-matching

Degenerate SHG can either be noncritical (type 0) interaction, where the FW and SH fields are polarized along the same direction, or critical (type I) interaction, where the FW and SH are cross-polarized along arbitrary directions in the (θ, ϕ) crystal angles (see Fig. 4.1 for definitions). We remark that:

- In type 0 the FW and SH are usually polarized along the crystal axes ($\theta = 0$ or $\pi/2$) since this turns out to maximize the nonlinearity, and it is called *noncritical interaction* because the interaction does not depend critically on the propagation angles (both nonlinearity and phase matching parameters vary little with angle). That being said, some crystal point groups (especially semiconductors) do not have maximum nonlinearity in the type 0 configuration along the crystal axes. Not all crystals support type 0, e.g. BBO has an extremely low d_{33} value. Of pros and cons we can mention

  + No spatial walk off (a direct consequence of the FW and SH having the same polarization).
  + The quadratic nonlinearities are typically 1-2 orders of magnitude larger than the type I crystal. This often more than compensates the rather large Δk to give high defocusing n_2^{casc} values.

  - + The phase-mismatch is large enough to *always* be in the non-resonant regime where phase-mismatch dominates over GVM. This means that there is no resonant transfer to the SH and that there is a minimal self-steepening.
  - + Some crystals like LN and KTP are very technologically mature and have high damage thresholds.
  - + A huge number of mid-IR crystals support type 0 interaction, often with very large quadratic nonlinearities
  - − Large Kerr focusing nonlinearity. We therefore consider the ratio $-n_2^{\text{casc}}/n_2^{\text{SPM}}$ between the cascading and the Kerr nonlinearity as an indicative figure-of-merit, cf. Eq. (4.8) in Sec. 4.4) and Fig. 4.3.
  - +/− High dispersion, since we try to achieve SHG where the SH has the same refractive index as the FW. Especially a high GVD gives a high soliton excitation intensity, but on the other hand the soliton is generated in extremely short crystals.
  - +/− The phase-mismatch is not controllable except if quasi-phase-matching (QPM) methods are employed, which requires that the crystal is ferroelectric (like LN and KTP). This seriously reduces the flexibility of cascading. On the other hand, QPM is incredibly powerful when it can be implemented, as one can do far more than just phase-matching (segmented QPM, adiabatic QPM etc.), meaning far more flexibility than a type I case in a non-ferroelectric crystal.

- In type I interaction, θ and ϕ values can often be found where phase matching is achieved. This interaction is very angle-sensitive, which is why it is called *critical interaction*. Of pros and cons we can mention
  - + Seamless tuning of the nonlinearity from strong to weak and from focusing to defocusing by adjusting crystal angle.
  - + Moderate Kerr focusing nonlinearity. Considering the $1/\Delta k$ scaling of n_2^{casc} it is (almost) always possible to get a total defocusing nonlinearity, but it might come at the price of strong self-steepening and significant SH conversion if Δk_{def} is close to zero, where Δk_{def} is the critical value for achieving a net total defocusing nonlinearity.
  - + Very abundant crystals, technologically mature, high damage thresholds.
  - +/− Moderate-to-low dispersion, since we exploit birefringent SHG where the SH is cross-polarized to the FW. The low GVD gives a low soliton excitation intensity, but on the other hand the soliton is generated in quite long crystals.
  - − The quadratic nonlinearities are moderate at best, low at worst.
  - − significant amount of spatial walk-off between the FW and the SH, implying that there is a trade-off concerning beam size and crystal length: If the SH walks away from the FW before the crystal exit the FW beam profile will be very distorted.

- Type II interaction is where the pump photons are cross-polarized, and thereby non-degenerate. We have not conducted any experiments in this configuration, so this will not be discussed further.

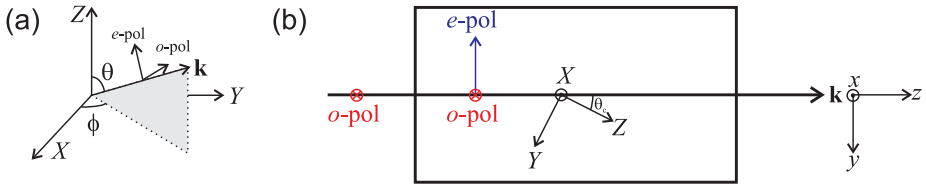

Figure 4.1: (a) The definition of the crystal coordinate system XYZ relative to the beam propagation direction $\mathbf{k}$. (b) Top view of the optimal crystal cut for type I $oo \rightarrow e$ SHG in BBO, which has $\phi = -\pi/2$ and $\theta = \theta_c$ for perpendicular incidence of an o-polarized FW beam, and the e-polarized SH is generated through type I $oo \rightarrow e$ SHG. The specific value of the cut angle θ_c depends on the wavelength and the desired application. Angle-tuning the crystal in the paper plane will change the interaction angle θ. Capital letters XYZ are traditionally used to distinguish the crystal coordinate system from the beam coordinate system xyz that has its origin in the $\mathbf{k}$-vector propagation direction. Taken from [8].

4.2 Basics of crystals

In uniaxial crystals (like BBO and LN), the isotropic base-plane is spanned by the crystal XY axes, and light polarized in this plane is ordinary (o-polarized) and has the linear refractive index n_o. The optical axis (crystal Z-axis, also called the c-axis) lies perpendicular to this plane, and light polarized in this plane is extraordinary (e-polarized) and has the linear refractive index n_e. In a negative uniaxial crystal like BBO, $n_o > n_e$. The propagation vector $\mathbf{k}$ in this crystal coordinate system has the angle θ from the Z-axis and the angle ϕ relative to the X-axis, cf. Fig. 4.1(a), and the e-polarized component will therefore experience the refractive index

$$n^e(\theta) = \left[\frac{\cos^2\theta}{n_o^2} + \frac{\sin^2\theta}{n_e^2}\right]^{-1/2} \tag{4.1}$$

while the o-polarized light always has the same refractive index. The spatial walk-off between the o and e polarized components in a negative uniaxial crystal is

$$\rho = \arctan\left(\frac{n_o^2}{n_e^2}\tan(\theta)\right) - \theta \tag{4.2}$$

4.3 Measuring BBO Kerr nonlinearities through cascading

BBO is a very popular crystal, especially for the early cascading experiments [20, 52, 23, 61, 27, 63, 29, 102, 103, 56]. It has a decent quadratic nonlinear coefficient, and because the crystal is anisotropic it can be birefringence phase-matched for type I ($oo \rightarrow e$) SHG. For femtosecond experiments it has the important properties of a low dispersion, a high damage threshold, and a quite low Kerr self-focusing nonlinearity; the latter is important for cascading as we discuss later, because the material Kerr nonlinearity will compete with the induced cascading nonlinearity.

As BBO is an incredibly important crystal also for many other applications, especially parametric amplifiers, we in [8] decided to make a review of the various experiments in the literature where the Kerr nonlinear refractive index was measured [102, 103, 104, 105, 106, 107, 108, 109, 56]. The goal was for the fist time extract all four tensor components that are relevant to describe the anisotropic nature of the cubic nonlinearity. We also measured the SPM nonlinear refractive index in the o-polarized direction.

BBO belongs to the crystal class $3m$, and has 3 independent $\chi^{(2)}$ tensor components and 4 independent $\chi^{(3)}$ tensor components. An excellent overview of the quadratic and cubic nonlinear coefficients in other anisotropic nonlinear crystal classes is found in [109].

For an arbitrary input (i.e. FW) polarization various SHG processes can come into play ($oo \to o$, $oo \to e$, $oe \to e$, $oe \to o$, $ee \to e$, and $ee \to o$). This includes both type 0, type I and type II. BBO is usually pumped with o-polarized light as the quadratic nonlinearity is largest for this configuration (d_{22} is the largest tensor component).

Note that BBO has historically been misplaced in the point group 3, and in addition there has been some confusion about the assignment of the crystal axes (where the mirror plane of the crystal was taken parallel instead of perpendicular to the crystal X-axis) [110]. Unfortunately this means that even today crystal company web sites operate with d_{11} as being the largest tensor component (in the $3m$ point group $d_{11} = 0$) and supply crystals apparently cut with $\phi = 0$ (because using the point group 3 combined with a nonstandard crystal axes definition means that $d_{11}\cos 3\phi$ must be maximized, while with the correct point group, $3m$, and correct crystal axes assignments, d_{22} is the largest tensor component and $\sin 3\phi = 1$ maximizes the effective nonlinearity). In order to sort out any confusion, the optimal crystal cut is shown in Fig. 4.1(b).

The SVEA propagation equations (2.2) have an "effective" third-order SPM nonlinearity, $\chi^{(3)}_{\text{SPM}}$, and cross-phase modulation (XPM) nonlinearity, $\chi^{(3)}_{\text{SPM}}$, which due to the anisotropy had to be calculated specifically for a given crystal class and input polarization. The SPM and XPM anisotropic cubic nonlinearities for a uniaxial crystal in the point group $3m$ were found in Eqs. (B13), (B14) and (B15) in [4]. For a type I interaction ($oo \to e$), where the FW is o-polarized and the SH e-polarized, they are

$$\chi^{(3)}_{\text{SPM}}(ooo \to o) = c_{11} \tag{4.3}$$

$$\begin{aligned}\chi^{(3)}_{\text{SPM}}(eee \to e) = &-4c_{10}\sin(\theta+\rho)\cos^3(\theta+\rho)\sin 3\phi + c_{11}\cos^4(\theta+\rho) \\ &+ \tfrac{3}{2}c_{16}\sin^2(2\theta+2\rho) + c_{33}\sin^4(\theta+\rho)\end{aligned} \tag{4.4}$$

$$\chi^{(3)}_{\text{XPM}}(ooe \to e) = \tfrac{1}{3}c_{11}\cos^2(\theta+\rho) + c_{16}\sin^2(\theta+\rho) + c_{10}\sin(2\theta+2\rho)\sin 3\phi \tag{4.5}$$

Instead for a type 0 $ee \to e$ interaction we have

$$\chi^{(3)}_{\text{SPM}}(eee \to e) = \chi^{(3)}_{\text{XPM}}(eee \to e) \tag{4.6}$$

with $\chi^{(3)}_{\text{SPM}}(eee \to e)$ given by Eq. (4.4). If the Kerr nonlinearity is considered isotropic, we have the classical relation $\chi^{(3)}_{\text{XPM}} = \chi^{(3)}_{\text{SPM}}$.

A mistake often seen in the early literature on type I interaction is to take $\chi^{(3)}_{\text{SPM}} = \chi^{(3)}_{\text{XPM}}$, and this mistake gives a 3 times too large XPM term. As shown above the identity $\chi^{(3)}_{\text{SPM}} = \chi^{(3)}_{\text{XPM}}$ only holds in the type 0 configuration, where the FW and SH have identical

polarizations, but importantly it is not an identity that is restricted to isotropic nonlinearities as it holds for an anisotropic medium as well. Thus, the error made in the past for type I could either come from using directly the propagation equations for an isotropic medium and where two pulses with the same polarization interact, but it could also come from generalizing type 0 SHG propagation equations to type I, and forgetting the XPM properties for cross-polarized interaction.

In fact, while the anisotropy of the quadratic nonlinearity is extensively used for optimizing the phase-matching properties and maximizing the quadratic nonlinear coefficients in nonlinear crystals, the case is different when it comes to treating the cubic nonlinearities: the anisotropic nature has often been neglected when studying self-phase modulation (SPM) effects from the Kerr nonlinear refractive index, in contrast to the case of third-harmonic generation, as evidenced even in early studies [111, 112]. In addition, historical measurements often neglect direct contributions to the measured nonlinear refractive index from the cascading effect.

This fact became a continuous frustration when trying to match our simulations to the experiments, so we decided to go through all the data in the literature, contact all the authors, and try to get some consensus on the parameters and experimental conditions, both concerning crystal orientation (as to determine which tensor components were measured). This detailed analysis is reported in [8].

Our results showed that the tensor component affecting the SPM of the ordinary wave, $c_{11} = \chi^{(3)}_{XXXX} = \chi^{(3)}_{YYYY}$, is very well documented, so after correcting the data for the various mistakes mentioned above, the corrected literature data agrees extremely well in the near-IR with the popular two-band model, cf. Eq. (4.10) [113].

Our experiment was based on the technique employed by Moses et al. [56]: essentially we first located the phase-matching angle and then angle-tuned the crystal until any visible nonlinear components of the spectrum had vanished (i.e. the spectrum at the exit of the crystal is unaltered compared to its input state) as $n_2^{\text{casc}} + n_2^{\text{SPM}} \simeq 0$ in this range. By fine-tuning (with $1/6^\circ$ precision) θ in this range we tracked the bandwidth 10 dB below the peak value of the recorded spectra for two different intensities. After analyzing also the contributions from XPM we found that the bandwidths became identical at the critical phase-mismatch value $\Delta k_c = 89 \pm 5\ \text{mm}^{-1}$, where the uncertainty lies mostly in finding a suitable transition value to track between the different intensities and phase mismatch values, as well as appropriately judging the contributions from XPM, see Sec. 5.2.3. This critical value corresponds to $\theta = 18.5^\circ$, $\rho = 2.7^\circ$ and $d_{\text{eff}} = 2.08$ pm/V, so calculating the cascading nonlinearity and employing the $n_2^{\text{casc}} + n_2^{\text{SPM}} = 0$ hypothesis, we get

$$n_2^{\text{SPM}} = 4.87 \pm 0.44 \cdot 10^{-20}\ \text{m}^2/\text{W},\ \lambda = 1.032\ \mu\text{m} \tag{4.7}$$

which corresponds to $c_{11} = 4.73 \pm 0.43 \cdot 10^{-22}\ \text{m}^2/\text{V}^2$. All in all, we must emphasize that this method is quite accurate for determining the Kerr nonlinearity, especially compared to the 20-30% uncertainty often seen with other techniques. This is partially because the quadratic nonlinearities and the linear dispersion properties of BBO both are very well known.

A summary of the modified literature data and our own measurement is shown in Fig. 4.2, together with the predicted electronic nonlinearity from the two-band model (2BM) [113]. The experimental near-IR data are amazingly well predicted on an *absolute* scale by the 2BM; we must here clarify that for the 2BM we chose the material constant

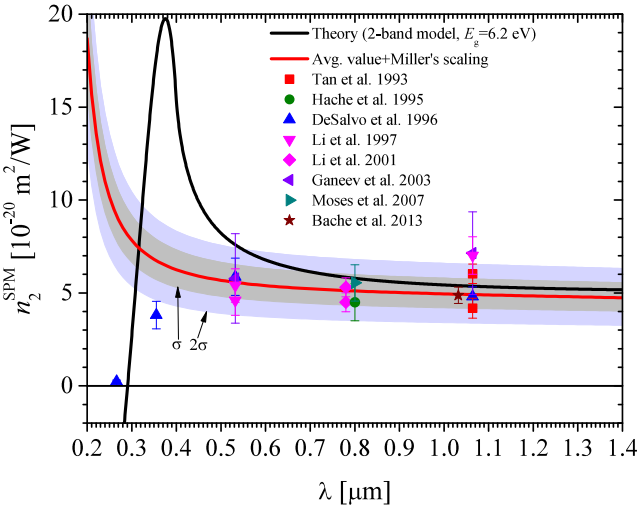

Figure 4.2: Summary of the experimental data for n_2^{SPM}-values from the literature corresponding to the c_{11} nonlinear susceptibility coefficient ($n_2^{\mathrm{SPM}} = 3c_{11}/4n_1^2\varepsilon_0 c$). The plotted values are the ones we extracted from the original literature data and taking into account updated knowledge of the BBO material parameters. References: Tan et al. 1993: [102]; Hache et al. 1995: [103]; DeSalvo et al. 1996 [104]; Li et al. 1997 [106]; Li et al. 2001 [107]; Ganeev et al. 2003 [108]; Moses et al. 2007 [56]; Bache et al. 2013 [8]. The theoretically predicted electronic nonlinearity is calculated with the 2-band model [113]. The average value curve was calculated through a weighted mean of the Miller's delta from all data, except the UV measurements below 400 nm, and the shaded areas denoted "σ" and "2σ" represent one and two standard deviations, respectively. Adapted from [8].

$K = 3100$ eV$^{3/2}$cm/GW, which was found appropriate as a single material parameter for dielectrics [104], and by using the BBO band-gap value $E_g = 6.2$ eV [104]. Thus, in practice there are no free parameters in the model, which underlines the incredible agreement obtained on an absolute scale (and not just the translation from one wavelength to another).

In the plot the red line is the average of all measurements. Such an average could be made by calculating the Miller's delta [114], generalized to cubic nonlinearities [92], which is a wavelength-independent parameter. The literature data also presented measurements of the 3 other tensor components of BBO, and after a similar analysis as for the c_{11} component, we show in Table 4.1 the proposed Miller's delta coefficients to be used for future reference in BBO.

We mention here at the end that the updated n_2^{casc} value that we measured, and which the average value from the literature data also agrees with, is substantially higher than the one we historically used ($n_2^{\mathrm{casc}} = 3.65 \cdot 10^{-20}$ m^2/W at 850 nm). However, after employing the new value in our simulations we get an almost perfect agreement between simulations and experimental data. We are therefore confident that this value is the correct one.

Table 4.1: Proposed nonlinear susceptibilities for the BBO anisotropic Kerr nonlinearity. Note the c_{16} value is deduced from the c_{11} and c_{10} coefficients, and the c_{33} value is deduced from the c_{11}, c_{10} and c_{16} coefficients.

	λ [μm]	$\chi^{(3)}$ [10^{-24} m^2/V^2]	Δ_{ijkl} [10^{-24} m^2/V^2]	Ref.
$c_{11} = \chi^{(3)}_{XXXX}$	-	-	$52.3 \pm 7.7^{(a)}$	[8]
$c_{10} = \chi^{(3)}_{XXYZ}$	1.053	-24 ± 4	-3.04	[109]$^{(b)}$
$c_{16} = \chi^{(3)}_{XXZZ}$	1.053	147 ± 34	23.8	[109]$^{(b)}$
$c_{33} = \chi^{(3)}_{ZZZZ}$	0.850	-535 ± 843	-147	[105]

$^{(a)}$This value corresponds to $c_{11} = 5.0 \cdot 10^{-22}$ m^2/V^2 at 800 nm. $^{(b)}$The THG tensor component was measured instead of the cubic self-action components.

4.4 Opportunities in the mid-IR

While traditionally cascading experiments have been conducted in type I crystals like BBO (mainly due to the direct control over the cascading nonlinearity through the phase-mismatch parameter), we conducted the first ever cascading experiment in a type 0 setting where no QPM was used [7]. Until then it was common sense that due to the large Δk of type 0, the cascading nonlinearity would only benefit from QPM since $n_2^{\text{casc}} \propto -1/\Delta k$ and QPM gives a residual QPM phase mismatch $\Delta k - 2\pi/\Lambda$ where Λ is the poling period. However, since QPM also has a penalty on d_{eff} of at least $2/\pi$, the phase-mismatch range where the QPM cascading strength is larger than without QPM also has a significantly increased self steepening. Additionally the residual QPM phase mismatch is at risk of entering the resonant regime, where resonant transfer to the SH can lead to significant depletion of the FW (whether or not this is wanted depends on the specific case, cf. the experiments in Chapter 6).

We therefore came to the surprising conclusion: take the type 0 cut of the crystal and do not use QPM to increase the cascading strength. We can simply use the figure-of-merit of type 0 crystals

$$\text{FOM} = \frac{-n_2^{\text{casc}}}{n_2^{\text{SPM}}} \tag{4.8}$$

We recognize that FOM > 0, since type 0 will always give a negative cascading nonlinearity, and FOM $= 1$ means that the SPM effect is zero, i.e. exactly the condition we used to find the c_{11} coefficient for BBO in the previous section. We therefore need FOM > 1 (best results when it is at least 1.1-1.2 or more) to be able to invoke a significant defocusing nonlinearity.

It turns out to work in LN for a certain wavelength range (FOM > 1 roughly from $1.15 - 3.0$ where defocusing is dominating), which we proved in an experiment exciting a defocusing soliton [7] at 1.3 μm. In [9] we investigated whether we could find similar crystals like LN, where the type 0 effective nonlinearity is large. It turns out that most of these crystals are mid-IR transparent, and this actually fueled our efforts to investigate the mid-IR range.

We analyzed a wide range of nonlinear frequency conversion crystals transparent in the mid-IR (both semiconductors and dielectric crystals) that can be used for ultrafast

cascading. Looking for crystals supporting self-defocusing solitons requires FOM > 1. Using d_{eff} at a given wavelength, λ_0, and using Miller's scaling [92] we get

$$n_2^{\text{casc}}(\omega) = -\frac{d_{\text{eff}}^2(\omega)}{c\varepsilon_0 n^2(\omega) n(2\omega)[n(2\omega) - n(\omega)]} \tag{4.9a}$$

$$d_{\text{eff}}(\omega) = \frac{d_{\text{eff}}(\omega_0)[n^2(\omega) - 1]^2[n^2(2\omega) - 1]}{[n^2(\omega_0) - 1]^2[n^2(2\omega_0) - 1]} \tag{4.9b}$$

where $n(\omega)$ is the linear refractive index and ω_0 is the frequency where d_{eff} is measured. We remind that in type 0 interaction the phase mismatch is always positive, and it only depends on wavelength (and somewhat also on temperature, which we here assume fixed).

The Kerr nonlinearity is often not experimentally measured for the mid-IR crystals, so we chose to model the frequency dependence of n_2^{SPM} using the two-band model (2BM) [115] as

$$n_2^{\text{SPM}}(\omega) = K' G_2(\hbar\omega/E_g)\sqrt{E_p}/n^2(\omega)E_g^4, \tag{4.10}$$

We remark that this is the electronic nonlinearity (no Raman), which is the one we need to know to understand the instantaneous focusing SPM contribution. Here K' is a material constant, fitted to $K' = 7.3 \cdot 10^{-9}$ $\text{eV}^{3.5}\text{m}^2/\text{W}$ in wide-gap dielectrics [104] and $K' = 14.0 \cdot 10^{-9}$ $\text{eV}^{3.5}\text{m}^2/\text{W}$ in semiconductors [115], $E_p = 21$ eV is the Kane energy, which is constant for most materials, E_g is the direct band gap energy (which we need to know for each material), and the function $G_2(x)$ can be found in [115, Table II]. $\hbar$ is the reduced Planck's constant in appropriate units to make $\hbar\omega/E_g$ dimensionless.

This incredibly simple idea makes it possible to sweep large wavelength ranges to get realistic ideas about good cascading crystals. We have to date investigated over 60 different nonlinear crystals suited for type 0 interaction, and where we could obtain (1) suitable Sellmeier equations (at least with 1 IR pole to ensure onset of anomalous dispersion), (2) reliable values for d_{ij} quadratic nonlinear tensor components and (3) optical band gap values E_g. Fig. 4.3 shows a summary of the best crystals we found; we have not shown the 30+ crystals where the FOM was not above unity.

The well-known near-IR cascading materials $LiNbO_3$ and $LiTaO_3$ are seen to have an FOM up to 2, and at around $\lambda = 2$ μm the GVD changes sign and becomes anomalous (dashed curve commences). The anomalous dispersion range is shown with dashed lines, and this is where resonant radiation waves can be excited if a defocusing soliton forms in the normal dispersion range. The chalcogenide $LiInS_2$ and the semiconductors ZnTe, GaSe, $CdSiP_2$ and $ZnGeP_2$ are seen to have potential as well for FOM > 1, and this is because they simultaneously have large band gaps and large quadratic nonlinearities. (Note that the latter two are of the point group $\bar{4}2m$, giving an $ee \to e$ interaction of $d_{\text{eff}} = 3d_{36}\sin\theta\cos^2\theta$ that is maximum for $\theta = 35^\circ$ and thus does not follow the traditional choice in type 0 interaction of polarizing along one of the optical axes.) AlGaAs is another interesting candidate, but in its pure form it is not stable, and reducing the aluminum content the FOM will be reduced (in fact, GaAs is below unity, as also confirmed experimentally at 5.0 μm [116]).

We can also consider pumping in the anomalous dispersion range [117], designated with dashed FOM curves. In this case, no solitons will form since the GVD and the total nonlinearity have the same sign. Instead strong spectral broadening occurs along with a

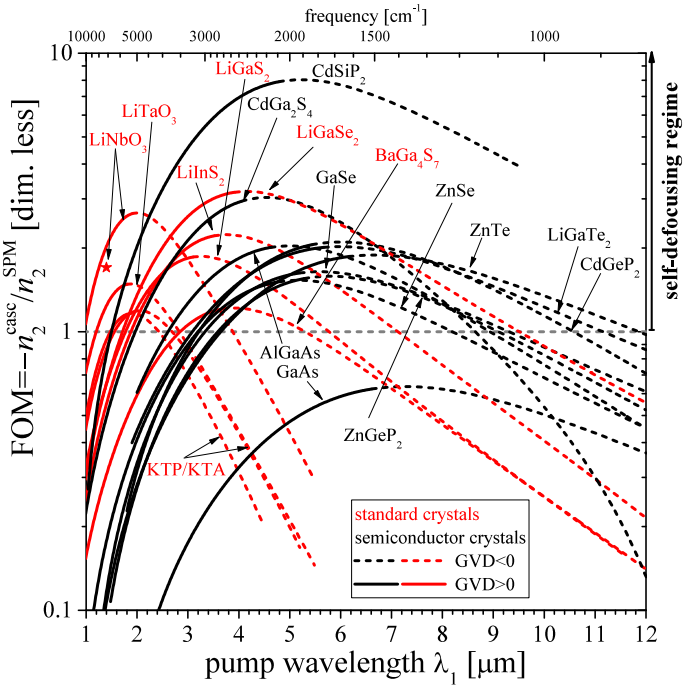

Figure 4.3: Cascading figure-of-merit (FOM) $-n_2^{\text{casc}}/n_2^{\text{SPM}}$ vs FW wavelength for cascaded non-critical type 0 SHG. Various dielectric (red) and semiconductor (black) materials are shown and the curves are full in the normal GVD regime and dashed in the anomalous GVD regime. The curves end where absorption becomes significant. Adopted from [9].

temporal re-shaping of the pulse to a very flat pulse with steep shock fronts. This is the so-called wave-breaking regime [118], and it is well known from fiber optics to produce a very linear chirp across the pulse, which afterwards is easily compensated by dispersive elements. Unlike the fiber-optics case, we here operate in bulk with negative nonlinearities and anomalous dispersion, so the compression stage has to introduce positive group-delay dispersion (GDD) to compress the pulse, and this can easily be done with a bulk piece of glass, and where tunable GDD is achieved by operating a pair of glass wedges. The continuum will not be as broad as in the soliton case, but it can be octave-spanning and is often more coherent and spectrally flatter.

It should be mentioned that since we use the 2BM to calculate the Kerr nonlinearity, the values are indicative. Take the one we know the best, LN, which we believe has the Kerr value $n_2^{\text{SPM}} = 54 \cdot 10^{-20}$ m^2/W, and a Raman fraction around 35%, estimated at 1.4 μm; this results in an FOM of 1.7, marked with a star. This is somewhat below the value shown in the curve. We might also be so lucky to find cases where the FOM is higher than expected.

This figure gives in a simple way an overview over the cascading possibilities offered by nonlinear crystals in the type 0 configuration. It is therefore a useful roadmap for discovering the potential of these crystals. In preparing it, we decided to try out the LIS

crystal ($LiInS_2$), a chalcogenide crystal that is commercially available. In Chapter 7 we show a successful experiment where this crystal was used to generate an octave-spanning mid-IR supercontinuum with 50 μJ energy slightly below the ZDW [13]. This represents the first outcome of the feasibility study presented here.

Chapter 5

Self-defocusing solitons

We think the same things at the same time
There are so many of us
Oh you can't count

Thom Yorke "Harrowdown Hill"

Here I first discuss the conditions required to excite defocusing solitons in cascaded SHG and how we can predict its behavior. I then show experimental results mixed with simulations to highlight the physics behind the results.

5.1 The soliton self-compression effect

In order to appreciate the soliton and how it can be used for pulse compression we first review the two main compression techniques, namely the external pulse compressor and the soliton self-compression method.

External pulse compression is a two-step process: (1) a spectral broadening stage, where the bandwidth to sustain a shorter pulse is accumulated, followed by (2) an external temporal compression stage by dispersive elements. The spectral broadening is achieved by SPM via the Kerr self-focusing effect and upon exiting the nonlinear medium the spectrally broadened pulse is temporally stretched with a positive chirp across it. Temporal compression is then achieved by dispersion cancellation on a pair of gratings. A very linear chirp can be achieved across the pulse, which optimizes the compressed pulse quality. Typically in the near-IR a gas-filled hollow capillary [74, 119] is used to compress high-energy (10s of GW) laser pulses; this method was recently explored up to $\lambda = 2\ \mu$m [120] but a generic mid-IR external pulse compressor has yet to be found.

Soliton self-compression occurs when the pulse experiences both spectral broadening and temporal compression in the same nonlinear medium, leaving external compression unnecessary. This relies on exciting a soliton, i.e. a nonlinear wave that exists as a balance of SPM and dispersion effects. The soliton self-compression effect is a renowned and frequently used method to compress longer pulses to ultrashort durations, even as little as 1-2 optical cycles. It relies on the fact that during the formation of an optical soliton with an intensity well beyond the balance point of a stable soliton, such a higher-order soliton will experience dramatic self-compression in the initial propagation stage. The soliton

compressor is less efficient than the external compressor and provides a less clean pulse profile, mainly because the chirp across the pulse is not linear.

Traditionally, the soliton method has been implemented in optical fibers (and to some degree waveguides). This implies that for femtosecond pulse compression the pulse energy is limited to the nanojoule range, considering the limited mode areas of standard fibers and photonic crystal fibers (PCFs). Recently, however, we must mention that gas-filled hollow-core core PCFs have shown the potential to handle sub-mJ pulse energies owing to the large mode areas and their high damage threshold.

In the traditional case, spectral broadening has been achieved by the self-focusing Kerr SPM effect, i.e. $n_2^{\mathrm{SPM}} > 0$. This has effectively prevented the soliton self-compression effect from being realized in bulk, non-waveguide structures. In fact, self-compression of GW-class pulses has historically only once been observed in a bulk piece of glass [121]. This is because for higher pulse energies as soon as the self-compression stage initiates the intensity increases and the beam starts to experience self-focusing. This means that the transverse profile collapses to a point where ionization sets in, which defocuses the beam preventing complete collapse. At further propagation a filamentation stage initiates where the beam has one or more "self-guiding" filaments of light-plasma interaction.

Filamentation is undesirable as it results in a poor spatial coherence. It is possible to harness the filamentation to achieve filament-based soliton self-compression of mid-IR pulses [122, 123], and compression of 80 fs multi-milliJoule mid-IR pulses at 3.9 μm was very recently shown [79]. The premise behind this recent advance seems to be that when the pump duration is short enough (below 10 optical cycles) the instability behind the filamentation is apparently suppressed under strong anomalous dispersion [80]. However, in many cases the pump lasers used do not have pulse durations below 10 cycles, take for instance state-of-the-art Ti:sapphire and Yb-doped laser amplifiers where the pulse duration is more often in the 15-50 cycle regime.

In turn self-defocusing nonlinearities would be desirable for pulse compression to avoid unwanted self-focusing and undesired filamentation. The main challenge has been that all materials are self-focusing[1], including the crystals we use. However, since as we have seen in Ch. 3 cascading can induce a self-defocusing Kerr lens effect, which uniquely can cancel self-focusing and even dominate to generate a net total self-defocusing effect; the beam will diverge instead of focus in the material and the process is therefore filament-free [20]. As a consequence there is really no longer any energy limit posed on the pump pulse.

This promise of an essentially filament-free nonlinearity has been the main driver behind the research of cascaded nonlinearities in the past decades. At the early stage the main motivation was the fact that it can be used for pulse compression, especially soliton self-compression, of in principle unlimited pulse energies.

Another early attraction with defocusing solitons was that because the nonlinearity has a negative sign, the appropriate GVD to support soliton formation is normal dispersion. This kind of dispersion is abundant in bulk crystals throughout the near-IR, and solitons can therefore be observed directly at the laser wavelengths without any need for waveguide dispersion engineering to get the right dispersion. Historically this was what prevented exploiting soliton formation for many years in self-focusing Kerr systems: the

[1] Except when pumping close to resonances, where undesired high linear and nonlinear losses will instead prevail.

pulsed lasers were operating in the normal GVD regime of optical fibers and waveguides where soliton formation cannot be observed.

5.2 Limits to efficient soliton formation in crystals

The early efforts into investigating soliton self-compression with cascaded self-defocusing solitons were using BBO bulk crystals and critical (birefringent) type I phase matching [23, 27, 29]. The goal was to compress high-energy pulses from laser amplifiers to few-cycle duration. However, a number of issues were not understood:

- How was the soliton dynamics connected to the well-known fiber case?
- Why was compression at 800 nm (Ti:sapphire lasing wavelength) not very efficient? Obviously this wavelength was (and still is) the main laser wavelength for mJ-class femtosecond laser amplifiers, but the 100+ fs pump pulses that were used were never compressed more than by a factor of 3.
- What are the limits to efficient soliton compression?
- Which wavelengths are the optimal for self-defocusing soliton formation in the near-IR?

In a series of theoretical and numerical papers [2, 1, 3, 4, 6] we addressed these issues.

5.2.1 The total soliton order

An important parameter to understand soliton dynamics is the soliton order N. It was coined in nonlinear fiber optics where it was defined as $N = \sqrt{L_D/L_{NL}}$, i.e. the ratio between the GVD dispersion length $L_D = T_0^2/|\beta_2|$ and the nonlinear length scale relative to the Kerr SPM effect $L_{NL} = [\gamma P_0]^{-1}$. Here β_2 is the GVD of the fiber mode, T_0 is the pulse duration of the sech^2-shaped soliton, and P_0 is the peak power of the soliton. γ is the nonlinear waveguide parameter defined by $\gamma = \omega_0 n_2^{SPM}/(cA_{eff})$, where A_{eff} is the effective area of the fiber mode.

In early simulations, we attempted to characterize the soliton compression aspects of the cascading nonlinearity. We had already derived the cascading NLSE, essentially Eq. (3.25), but from this equation it is not clear how to proceed. Instead, if one performs the lowest-order expansions of the convolution integrals, i.e. Eq. (3.29) in absence of higher-order terms, we get

$$(i\partial_\xi + \hat{D}'_{\omega_1})U_1 - \left(s_{\Delta k}N_{casc}^2 - N_{SPM}^2\right)U_1|U_1|^2 = 0 \tag{5.1}$$

where we have adopted normalized parameters $\tau' = \tau/T_0$, $\xi = \zeta/L_{D,1}$, $U_1 = A_1/\sqrt{I_0}$, and $\hat{D}'_{\omega_1} = \hat{D}_{\omega_1}L_{D,1}$ where $L_{D,1} = T_0^2/|k_1^{(2)}|$ is the GVD length of the FW and I_0 is the peak input intensity of the FW. We have here defined the soliton orders

$$N_{casc}^2 = \frac{L_{D,1}}{L_{NL}^{casc}} = L_{D,1}\frac{\omega_1}{c}|n_2^{casc}|I_0 = L_{D,1}\frac{2\omega_1^2 d_{eff}^2 I_0}{c^3\varepsilon_0 n_1^2 n_2|\Delta k|} \tag{5.2a}$$

$$N_{SPM}^2 = \frac{L_{D,1}}{L_{NL}^{SPM}} = L_{D,1}\frac{\omega_1}{c}n_2^{SPM}I_0 = L_{D,1}\frac{3\omega_1\chi_{SPM}^{(3)}I_0}{4c^2\varepsilon_0 n_1^2} \tag{5.2b}$$

We note that to keep the cascading soliton order real, i.e. $N_{\text{casc}}^2 > 0$, in both the focusing ($\Delta k < 0$) and the defocusing case ($\Delta k > 0$), we have introduced the sign of the phase-mismatch parameter $s_{\Delta k} = \text{sgn}(\Delta k)$. We also mention that N_{SPM}^2 is the usual Kerr soliton order, or at least as it would be in a bulk medium (where it is not common to use it).

What we are interested in is the case where the cascading nonlinearity is self-defocusing, $n_2^{\text{casc}} < 0$, which requires $\Delta k > 0$, i.e. $s_{\Delta k} = 1$. We must also aim at achieving a total defocusing nonlinearity $n_2^{\text{tot}} = n_2^{\text{casc}} + n_2^{\text{SPM}} < 0$, which gives the defocusing NLSE

$$\left[i\partial_\xi - \tfrac{1}{2}\text{sgn}(k_1^{(2)})\partial_{\tau'^2} \right] U_1 - N_{\text{tot}}^2 U_1 |U_1|^2 = 0 \tag{5.3}$$

where we have defined the total soliton order

$$N_{\text{tot}}^2 = N_{\text{casc}}^2 - N_{\text{SPM}}^2 = L_{\text{D},1} \frac{\omega_1}{c} (|n_2^{\text{casc}}| - n_2^{\text{SPM}}) I_0 \tag{5.4}$$

This is the soliton order that governs the self-compression dynamics of the defocusing cascading case.

5.2.2 Basic properties of defocusing solitons

We have in the above NLSE included only GVD and neglected higher-order dispersion. This defocusing NLSE can be shown to support a soliton solution only when the GVD is normal, i.e. $\text{sgn}(k_1^{(2)}) > 0$. To see this we take the following soliton ansatz

$$U_{1,\text{sol}} = \text{sech}(N_{\text{tot}}\tau') e^{iq'_{\text{sol}}\xi} \tag{5.5}$$

Inserting Eq. (5.5) into Eq. (5.3) we get that the ansatz is a solution if $\text{sgn}(k_1^{(2)}) - 1 = 0$ and $2q'_{\text{sol}} + N_{\text{tot}}^2 = 0$. This therefore confirms that normal dispersion is required to support the defocusing soliton, and we find that the dimensionless soliton wave number is $q'_{\text{sol}} = -N_{\text{tot}}^2/2$. The negative sign is due to the fact that we are dealing with self-defocusing nonlinearities, which naturally leads to a negative nonlinear phase shift $\phi_{\text{sol}} = q'_{\text{sol}}\xi$. When converting to physical units the soliton wave number becomes

$$q_{\text{sol}} = -\frac{N_{\text{tot}}^2}{2L_{D,1}} \tag{5.6}$$

$$= n_2^{\text{tot}} I_0 \frac{\omega_1}{2c} \tag{5.7}$$

where we remind that $n_2^{\text{tot}} < 0$. The latter expression is identical to that found in [124]. We see that $q_{\text{sol}}L$ physically can be understood as the accumulated nonlinear phase after propagating a certain length L with intensity I_0 and nonlinearity n_2^{tot}.

Finally, because the effect of GVD is balanced out by the nonlinear phase shift in the NLSE, the soliton is inherently dispersion-free and the following $\omega - k$ dispersion relation can be put forward

$$k_{\text{sol}}(\omega) = k_1(\omega_{\text{sol}}) + (\omega - \omega_{\text{sol}})/v_{g,\text{sol}} + q_{\text{sol}} \tag{5.8}$$

i.e. the soliton is a straight line in $\omega - k$ domain only having a phase (linear as well as nonlinear) and a group velocity $v_{g,\text{sol}}$ (which typically follows the group velocity dictated by the nonlinear medium at the soliton frequency; this is reflected in the fact that solitons can be accelerated or slowed down when frequency shifted, e.g. by Raman effects).

5.2.3 The compression window

The definition of the total soliton order allows us to make concrete calculations regarding where we can expect to observe solitons. In cascading the phase-mismatch parameter is a free tuning parameter, allowing us to manipulate the cascading soliton order while keeping the SPM soliton order fixed. We can therefore define the following limiting choices regarding the phase-mismatch parameter (always considering a defocusing nonlinearity, i.e. $\Delta k > 0$)

- We need to have a total defocusing nonlinearity, i.e. $n_2^{\text{tot}} < 0$, leading to the requirement $\Delta k < \Delta k_{\text{def}}$
- We need to have enough nonlinearity to excite a self-defocusing soliton, i.e. $N_{\text{tot}} \geq 1$, leading to the requirement $\Delta k < \Delta k_{\text{sol}}$
- We need to avoid excessive self-steepening and resonant coupling to the SH, i.e. be above the threshold for the nonlocal resonant response, leading to the requirement $\Delta k > \Delta k_{\text{r}}$, as defined in Eq. (3.14)

Concerning the first requirement, the defocusing threshold can be expressed by requiring $N_{\text{casc}}^2 = N_{\text{SPM}}^2$, leading to the *defocusing threshold*

$$\Delta k_{\text{def}} = \frac{8\omega_1 d_{\text{eff}}^2}{3cn_2\chi_{\text{SPM}}^{(3)}} = \frac{2\omega_1 d_{\text{eff}}^2}{\varepsilon_0 c^2 n_1^2 n_2 n_2^{\text{SPM}}} \tag{5.9}$$

The next requirement follow directly from this, as we now require $N_{\text{casc}}^2 - N_{\text{SPM}}^2 = 1$, leading to the *defocusing soliton threshold*

$$\Delta k_{\text{sol}} = \Delta k_{\text{def}}(1 + N_{\text{SPM}}^{-2})^{-1} = \Delta k_{\text{def}}\left(1 + \frac{c|k_1^{(2)}|}{\omega_1 n_2^{\text{SPM}} T_0^2 I_0}\right)^{-1} \tag{5.10}$$

We note that in terms of nonlinear refractive indices the defocusing soliton threshold is expressed as $L_{D,1}\frac{\omega_1}{c}(n_2^{\text{casc}} + n_2^{\text{SPM}})I_0 = -1$. As expected the soliton threshold becomes affected by the input intensity and pulse duration through the SPM soliton order.

The final requirement is related to the nonlocal response: it was shown previously in Eq. (3.14) that by keeping the phase-mismatch above the resonant threshold the nonlocal response is non-resonant. This is important because in the resonant regime the energy transfer to the resonance in the SH is substantial and in addition self-steepening will increase, as discussed in Sec. 3.3. Therefore this is a softer requirement than the others, as soltons can also be excited for $\Delta k < \Delta k_{\text{r}}$.

Based on these limits we defined a so-called *compression window* [2], i.e. a phase-mismatch range where efficient pulse compression through a self-defocusing soliton is possible. In Fig. 5.1 the results are shown for two of the crystals often used, namely BBO and LN, both in the type I configuration. We remark from the BBO results how sensitive the cascading effect is to the Kerr SPM nonlinearity: the dashed red line uses a historical value that we used in our early papers and simulations, while the full red line uses an updated value that we measured recently [8], cf. Sec. 4.3. In LN the lower limit (related to the GVM-controlled resonant threshold) behaves more or less like BBO, but the upper

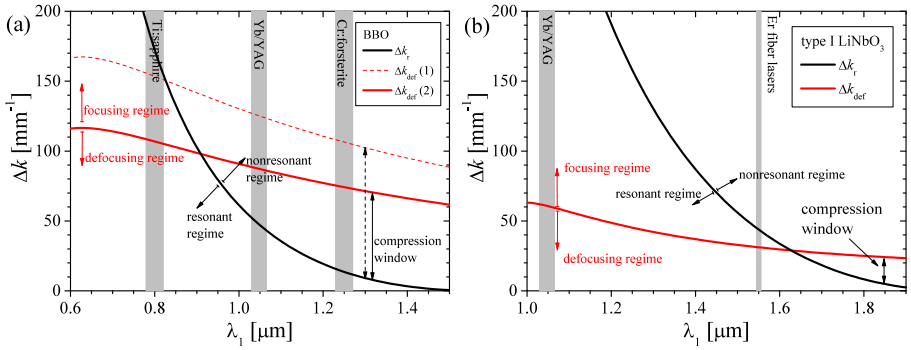

Figure 5.1: The compression window vs pump wavelength for type I cascading in (a) BBO [8] and (b) LN [4]. In both cases the upper wavelength range stops at the zero GVD wavelength. Note that $\Delta k_{\rm sr}$ is calculated for the full dispersion case, for which Eq. (3.14) is an approximation to 2. order. In (a) two values of the Kerr SPM nonlinearity is shown: case (1) corresponds to the Kerr value $n_2^{\rm SPM} = 3.65 \cdot 10^{-20}$ m^2/W@850 nm (taken from [105] and used in our early papers) and case (2) corresponds to the Kerr value found in [8]. In (b) we used $n_2^{\rm SPM} = 20 \cdot 10^{-20}$ m^2/W@780 nm [125]. The Kerr limit employs Miller's rule to calculate the nonlinear quadratic and cubic susceptibilities at other wavelengths. We have also indicated the operation wavelengths of Er, Cr:forsterite, Yb and Ti:Sapphire based amplifiers.

limit (i.e. the defocusing limit) provides a much more restrictive parameter space. This is mainly because the Kerr SPM nonlinearity of LN is quite large and thus it does not benefit from having $d_{\rm eff}$ values twice as large as BBO. The morale is that both large quadratic and low cubic nonlinearities are essential to have a good cascading crystal; this was the basis of the figure-of-merit we introduced in Sec. 4.4.

The compression window shown here is indicative as the upper limit does not really say anything about when we can excite a soliton, but just when the crystal total nonlinearity becomes self-defocusing. Once we decide on a pulse duration and/or intensity, this upper limit can be elaborated to specifically indicate the soliton threshold $\Delta k_{\rm sol}$. Through numerical simulations the validity was tested by propagating a sech-shaped pulse through a crystal and looking for the phase-mismatch value where the pulse stayed unaltered. This indicates the soliton threshold. Examples of the results are shown in Fig. 5.2: the numerical data agree well with Eq. (5.10), except close to the defocusing limit where the phase-mismatch value needed to excite a soliton drops. In the simulations this expresses itself in an increased threshold for soliton excitation, i.e. that $N_{\rm tot}$ must be taken larger than unity to see a stable soliton. Defining $N_{\rm tot,sol}$ as the soliton excitation threshold, the standard result $N_{\rm tot,sol} = 1$ no longer holds and we need to use $N_{\rm tot,sol} > 1$ to see a stable soliton; below we derive an expression that explains this deviation from unity.

The explanation from this deviation is found in the Kerr XPM terms of the coupled-wave SHG equations. This was also concluded in our early study [2] through numerical simulations, and below we provide for the first time an analytical explanation. We commence at the cascading NLSE-like equation (3.7) and adopting the dimensionless scaling

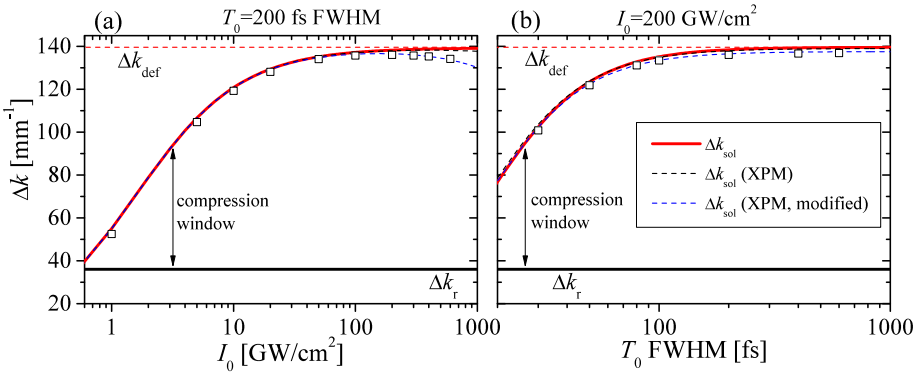

Figure 5.2: The BBO compression window vs (a) pump intensity and (b) pump duration for $\lambda_1 = 1.064\ \mu$m [2, Fig. 1]. Note that $n_2^{\rm SPM} = 3.65 \cdot 10^{-20}$ m^2/W and $\rho_{\rm XPM} = 1/3$ was used and furthermore the Sellmeier equations and the d_{ij} values for BBO were taken from [110]. The XPM soliton threshold is Eq. (5.13), and the modified version uses a $\rho_{\rm XPM}$ factor that is 6 times larger.

it reads

$$(i\partial_\xi + \hat{D}'_{\omega_1})U_1 + L_{\mathrm{D},1}\tfrac{\omega_1}{c} I_0 \left(n_2^{\rm casc} + n_2^{\rm SPM}\right) U_1|U_1|^2 + L_{\mathrm{D},1}\tfrac{\omega_1}{c} I_0^2 n_4^{\rm casc} U_1|U_1|^4 = 0 \quad (5.11)$$

where $n_4^{\rm casc}$ is defined in Eq. (3.8). We remind that it comes from the SH cascading solution being inserted back into the FW through the XPM term there. As the nonlinear index change now reads $\Delta n = (n_2^{\rm casc} + n_2^{\rm SPM})I_0 + n_4^{\rm casc} I_0^2$, this means that the requirement for exciting a defocusing soliton is

$$L_{D,1}\frac{\omega_1}{c}\left[(n_2^{\rm casc} + n_2^{\rm SPM})I_0 + n_4^{\rm casc} I_0^2\right] = -1 \quad (5.12)$$

We can express the soliton threshold Eq. (5.12) in terms of a critical phase-mismatch value

$$\Delta k_{\rm sol} = \tfrac{1}{2}\Delta k_{\rm def}(1 + N_{\rm SPM}^{-2})^{-1}\left(1 + \sqrt{1 - (1 + N_{\rm SPM}^2)\frac{8\rho_{\rm XPM} n_1}{n_2 L_{\mathrm{D},1}\Delta k_{\rm def}}}\right) \quad (5.13)$$

where we have defined the ration between the XPM and SPM nonlinearity as $\rho_{\rm XPM} = \chi^{(3)}_{\rm XPM}/\chi^{(3)}_{\rm SPM}$.[2] As we can see this expression in absence of XPM reverts back to the previous expression Eq. (5.10). This modified expression is also plotted in Fig. 5.2; while it does explain the shrunk window, it does not seem to fully explain the drop. In fact, if we increase the XPM ratio by a factor of 6 a much better agreement is found. This indicates that the approach outlined above underestimates the full effect of XPM. This may be because the XPM effect, being $\propto I_0^2$, for short pulse it induces a nonlinear phase shift mainly in the pulse center, and this leads to a stronger impact on the soliton threshold than predicted by the theory here. This is also discussed in connection with Fig. 4 in [2].

To further explain what goes on with XPM, in [2] we fitted the data from Fig. 5.2 and other similar data to the expression $N_{\rm tot,sol} = 1 + \Phi_0/\Phi_c(1 + \Phi_c/\Phi_0)^{-1}$ [2, Eq. (15)]

[2]Note that compared to [2] the relation is $B = 2\rho_{\rm XPM}$.

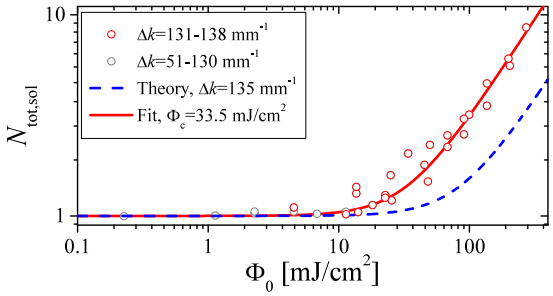

Figure 5.3: The numerical data from Fig. 3 of [2] showing the observed soliton threshold $N_{\text{tot,sol}}$ vs. pulse fluence for a range of simulations like those of Fig. 5.2. The fit uses Eq. (5.15) and is made to the data in the limited range $\Delta k = 131 - 138$ mm^{-1} (red circles). We also show Eq. (5.15) using the theoretical value of Φ_c from Eq. (5.16) using $\Delta k = 135$ mm^{-1} fixed.

where Φ_0 is the pulse fluence; $\Phi_0 = 2T_0 I_0$ for a sech-shaped pulse $\sqrt{I_0}\text{sech}(t/T_0)$. We found a critical fluence $\Phi_c = 33.0$ mJ/cm^2 found through the fit. The data behind this fit is shown in Fig. 5.3.

Here we present an explicit analytical expression explaining this behavior, and make a new fit to the resulting equation. The defocusing soliton threshold (5.12) can be expressed as $N^2_{\text{tot,sol}} = 1 + L_{D,1}\frac{\omega_1}{c} n_4^{\text{casc}} I_0^2$. If we consider the $n_4^{\text{casc}} I_0^2$ term as a perturbation to the nonlinearity, we get that the soliton order must be corrected as

$$N^2_{\text{tot,sol}} = 1 + \frac{2\rho_{\text{XPM}} n_1 N^2_{\text{SPM}} N^2_{\text{casc}}}{n_2 \Delta k L_{D,1}} \tag{5.14}$$

$$= 1 + \Phi_0^2/\Phi_c^2 \tag{5.15}$$

It is clear from the above expression that the standard soliton threshold $N^2_{\text{tot,sol}} = 1$ is now increased due to XPM. In the second line we have rewritten the XPM contribution in terms of the pulse fluence and we have defined a critical fluence

$$\Phi_c^2 = \frac{2c^2 n_2 \Delta k k_1^{(2)}}{n_1 \omega_1^2 |n_2^{\text{casc}}| \rho_{\text{XPM}} n_2^{\text{SPM}}} \tag{5.16}$$

$$= \frac{\varepsilon_0 c^4 n_1 n_2^2 \Delta k^2 k_1^{(2)}}{\omega_1^3 d_{\text{eff}}^2 \rho_{\text{XPM}} n_2^{\text{SPM}}} \tag{5.17}$$

This is the main result: it explains why we found in [2] that the pulse fluence was the main scaling parameter, and the scaling $N_{\text{tot,sol}} = \sqrt{1 + \Phi_0^2/\Phi_c^2}$ is also very similar to the empirical relation [2, Eq. (15)]. However, our theory here shows that $\Phi_c \propto \Delta k$, meaning it cannot be considered a "universal" constant as otherwise indicated in [2].

We here stress that the data in Fig. 5.3 use a wide range of Δk values (from 55-138 mm^{-1}). Most of them, though, are in the range $\Delta k = 131 - 138$ mm^{-1} (red circles) where Φ_c is almost constant, and we can therefore as a good approximation express the threshold by a single curve (the value for $\Delta k = 135$ mm^{-1} is $\Phi_c = 85$ mJ/cm^2). However, as we can see in the figure, the theoretical curve for this Δk range seems to underestimate the effect

of XPM; in fact to get a better agreement we have to modify the expression essentially by increasing the XPM effect. Just as in the previous case in connection with Eq. (5.13) a factor of 6 increase in the XPM value seems to give a good empirical trend for the increased soliton threshold as the pulse fluence is increased. A fit to Eq. (5.15) gives $\Phi_c = 33.5$ mJ/cm^2; this value is in fact almost exactly $\sqrt{6}$ smaller than the theoretical value.

Finally, let us mention a small caveat in the approach outlined above: Eqs. (5.10) and (5.13) are approximations to give convenient explicit expressions. In reality we should really solve the soliton threshold equations, e.g. Eq. (5.12), and find the phase-matching *angle* that solves the equation. This is because on the right-hand side we have d_{eff} and n_2 that both depend on the angle and they are assumed constant in solving the equations as we do above. Instead Eq. (5.15) does not have this problem, because it simple states what kind of soliton order one needs to exceed for a certain phase-mismatch value, i.e. here the angle θ is inherently taken fixed. That being said, we underline once again that a curve like the one shown in Fig. 5.3 exists for each value of Δk since the theory states that $\Phi_c \propto \Delta k$.

Another point worth making is that the quintic cascading nonlinearity should be considered a small perturbation to the cubic nonlinearity. Thus it will not hold if XPM is very dominant. As long as this is not the case, we can actually use the expression not only to predict the delayed onset of soliton formation, but also to predict a sort of modified total soliton order

$$N_{\text{tot}}^2 = N_{\text{casc}}^2 - N_{\text{SPM}}^2 - \Phi_0^2/\Phi_c^2 \tag{5.18}$$

5.2.4 Scaling laws for defocusing solitons

After having verified the onset of soliton formation, we in [2] conducted systematic numerical investigations in the nonresonant regime, where the self-compressed soliton is free of artifacts like XPM and excessive self-steepening. The goal was to find scaling laws similar to nonlinear fiber optics for expected soliton duration, compression efficiency and compression distance, respectively. These are in fiber optics typically expressed by the compression factor f_c, the pulse quality Q_c and the optical compression distance z_{opt} [126, 127, 128]. We found

$$f_c = 4.7(N_{\text{tot}} - 0.86) \tag{5.19a}$$

$$Q_c = [0.24(N_{\text{tot}} - 1)^{1.11} + 1]^{-1} \tag{5.19b}$$

$$\frac{z_{\text{opt}}}{z_0} = \frac{0.44}{N_{\text{tot}}} + \frac{2.56}{N_{\text{tot}}^3} - 0.002 \tag{5.19c}$$

where $z_0 = \frac{\pi}{2} L_{D,1}$ is the characteristic soliton length scale. These expression fit the ones from the fiber optics case quite well, which is not too surprising as the cascading interaction is well described by an NLSE, but unlike the NLSE scaling laws in the literature the data we used allowed us to fit also for low values of the soliton order. The data and the fit plots can be seen in Fig. 6 in [2].

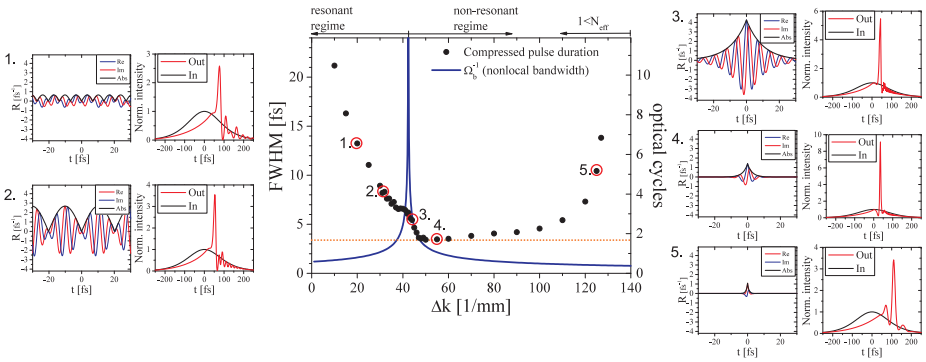

Figure 5.4: Tuning the nonlocal landscape for a fixed soliton order. The data are taken from simulations of BBO using 200 fs FWHM pulses at $\lambda_1 = 1.064\ \mu$m, and in all simulations $N_{\text{tot}} = 8$ was kept fixed. The orange dashed line shows the predicted compressed pulse duration for that soliton order. Five soliton examples are shown at selected phase-mismatch values along with the temporal shape of the corresponding nonlocal response function. Adapted from [3].

5.2.5 Limits to soliton compression

Early experimental data by Ashihara et al. showed that in BBO at 800 nm soliton self-compression could be observed for a wide range of phase-mismatch values, and it turned out some phase-mismatch values showed cleaner solitons than others. Numerically it was found that only in certain ranges was it possible to observe few-cycle compressed solitons. It was clear that GVM played an important role: as Δk becomes smaller the self-steepening effect increases, and we pointed out that performing the soliton excitation in the non-resonant regime also adds the benefit of avoiding coupling into a resonance in the SH. However, the question remained: if the governing property of cascading solitons is the total soliton order, as shown in [2], why can we not then for any Δk inside the compression window adjust the intensity appropriately to get the total soliton order needed to obtain the desired self-compression behavior? This was investigated in [3].

A summary of the findings in [3] is shown in Fig. 5.4. We used a fixed soliton order, giving sub-2 optical cycles pulse compression in the best case (case 4.). However, as we tuned the phase-mismatch value around in the compression window, we got very different results. Going towards the defocusing limit $\Delta k \simeq 140\ \text{mm}^{-1}$ the increased pulse duration can be explained by changes in the soliton order due to increased XPM effects. In fact, using the modified total soliton order (5.15) gives a significant a drop in soliton order as the boundary is approached, simply because n_2^{tot} becomes very small so large intensities are needed to reach a certain soliton order. This drives up the pulse fluence, reducing the modified soliton order giving increased compressed pulse duration. Another detail here is that clearly the trailing edge has experienced significant self-steepening, cf. case 5., which seems puzzling as self-steepening nonlinearities are minimized in this end of the compression window. The explanation is that to keep $N_{\text{tot}} = 8$ fixed the intensity is an order of magnitude larger than case 4, due to the cascading nonlinear scaling with $1/\Delta k$. This gives normalized self-steepening factors $n_2^{\text{SS}} I_0 T_0$, cf. Re. (3.31), that are in the range between 0.1 and 1, which amounts to very large self-steepening.

Going now towards the transition to the resonant regime, case 3. shows that the compressed pulse duration has increased compared to case 4., despite still being in the non-resonant regime. The explanation is that the nonlocal temporal bandwidth now limits the compressed pulse duration, cf. Eq. (3.17), which is plotted with blue. This remarkable result shows how the nonlocal theory helps unraveling the physics behind the pulse compression.

In the resonant regime the pulse duration follows a $1/\Delta k$ trend, whose origin can be found in the self-steepening contribution from cascading ($\propto d_{12}/\Delta k$), cf. Eq. (3.31). The time traces of the compressed solitons in cases 1. and 2. also show increased self-steepening signs as Δk is reduced. This is even more remarkable considering that in this range the cascading nonlinearity is very large, so the intensity to get the required soliton order drops to around 20 GW/cm^2. We also remark that a consequence of operating in the resonant regime is that there is phase-matching from the FW to the SH spectrum (to the frequency $\omega_2 + \Omega_+$), which leads to significant depletion of the FW (up to 35% at $\Delta k = 10$ mm^{-1}, compared to around 2% at $\Delta k = 60$ mm^{-1}). The main depletion of the FW does not happen before the soliton forms, though, so it is not contributing directly to the reduced duration of the soliton.

5.3 Experimental observation of solitons

Soliton self-compression in bulk crystals was originally observed by Ashihara et al. [23, 26, 28] and by Moses et al. [27, 29]. Initially the focus was pulse compression at 800 nm, the Ti:sapphire wavelength, where Wise's group had shown early promising results of spectral broadening without focusing in BBO followed by compression in a block of glass having normal dispersion to compensate for the accumulated nonlinear phase shift [20]. Ashihara et al. realized that this two-step compression could be done without the external compression stage, simply by letting the normal dispersion in BBO do the compression, i.e. excitation of a temporal soliton [23]. Both experiments evidenced that GVM in BBO at 800 nm was quite strong and a limiting factor for efficient few-cycle soliton formation. They were therefore followed by experiments at longer wavelengths where GVM is reduced, e.g. the experiments at 1260 nm by Moses et al. [27, 29] and at 1550 nm by Ashihara et al. in PPLN [26, 28].

Our initial focus was pulse compression of fiber-laser amplifiers. The most common ones (at the time) operated at 1030-1070 nm (Yb-doped fibers) and emitted 300-500 fs pulses with 10's of μJ energy, and at 1550 nm (Er-doped fibers) emitting sub-ps pulses with μJ pulse energies. Therefore we quickly abandoned Er-doped fiber lasers because the pulse energies were too low and the pulse duration was too long. Yb-doped lasers were therefore the focus, and our simulations showed that 200 fs pulses could be compressed in 25-30 mm BBO crystals [3]. However, since fiber lasers at the time emitted pulses in the range 300-500 fs, the crystal length needed was too long, and instead we investigated LN in a type I configuration as a possible alternative [4]. As Fig. 5.1 shows, the defocusing regime of LN is well into the resonant regime, and the simulations indeed showed strong coupling to the SH resonance and significant self steepening. Thus, the compression limit was $>$100 fs, which is not attractive to pursue experimentally.

In connection with a later experiment set up for validating resonant radiation in BBO [12], we observed the defocusing temporal soliton using roughly the same pump wave-

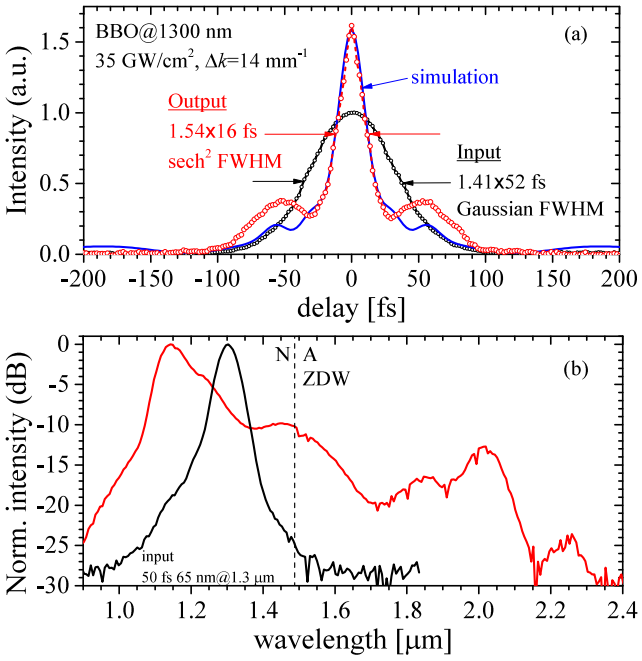

Figure 5.5: Experimental recording of a defocusing temporal soliton in BBO [12], showing the input and output (a) autocorrelation trace and (b) near-IR power spectrum. The experiment was conducted for $\lambda_1 = 1.3$ μm and $\Delta k = 14$ mm^{-1} using a 25 mm crystal, having 52 fs FWHM Gaussian shape at the input and peak intensity estimated at 35 GW/cm^2 (around 70 μJ pulse energy). The simulation result in (a) is shown in detail in Fig. 5.6.

length as in [27], namely 1300 nm. The major difference was, however, that the input pulse duration was 50 fs (instead of 100 fs) and that we had much more pulse energy available. This allowed us to use much looser focusing conditions (larger beam diameter) eliminating divergence problems and spatial walk off. As Fig. 5.5 evidences the recorded intensity autocorrelation trace shows a very clean compressed sech-shaped soliton with 16 fs FWHM duration. It agrees almost perfectly with the numerical simulations, and the pedestal is typical for soliton compression: as the detailed dynamics in Fig. 5.6 shows it is a mixture of the uncompressed pedestal and emission of resonant radiation.

The simulation in Fig. 5.6 also serves as a good example of the soliton dynamics in type I crystals like BBO. The FW soliton (in the *o*-polarization) here shows self-compression after 12 mm (the soliton order $N_{\rm tot} \simeq 2.8$), after which it stabilizes the the 16 fs duration shown in (a). During the self-compression stage it emits long-wavelength resonant radiation beyond the zero-dispersion wavelength (ZDW). The soliton itself is blue-shifted; this is actually caused by the cascading self-steepening terms [61, 63, 85]. Note in this context how the self-compressed soliton has a strong trailing edge shock front. As we recently pointed out [85] the Raman effects can counter this blue shift of the soliton, annulling or even make the soliton red-shift, and in fact in LN the soliton will experience a strong red shift (see Sec. 5.3 later). The dynamics of the *e*-polarized SH con-

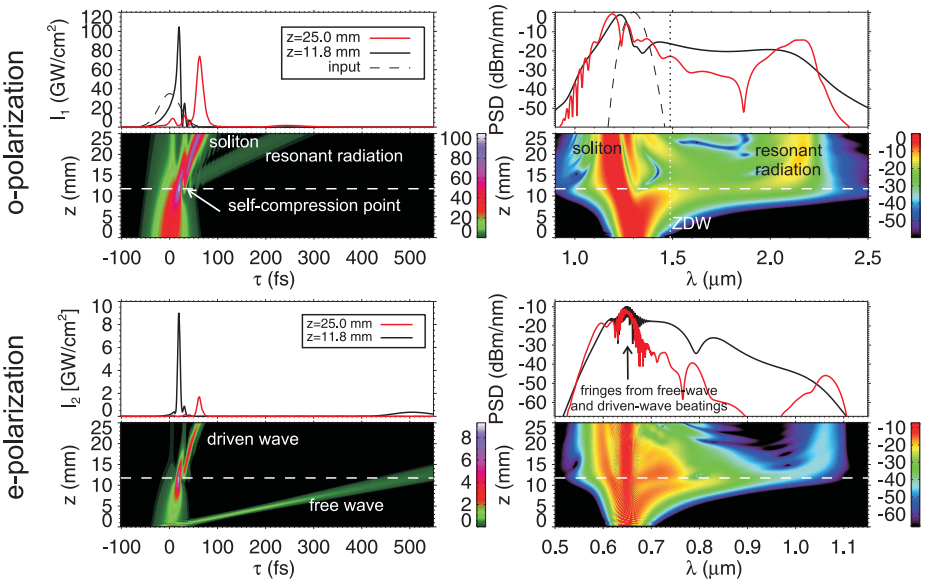

Figure 5.6: Simulation of the experiment in Fig. 5.5 using the plane-wave coupled-wave equations (2.2) with no free parameters; the Kerr SPM nonlinearity was taken from [8] and the input pulse was slightly negatively chirped $C = -0.9$ (-480 fs^2) to get the same input bandwidth as in the experiment.

tains mainly a free-wave and a driven wave. The free wave is traveling with the SH group velocity, and due to GVM it is delayed and walks away temporally. The driven wave is the one that the cascading ansatz (3.9) models and implicit in the ansatz is that it actually travels with the group velocity of the FW. This is confirmed in the simulation. In the SH spectrum we therefore see mainly this broad spectrum corresponding to the driven wave, and the free wave is just a linear wave having the center wavelength at the SH; this means that at this wavelength we see spectral beatings between the free wave and the driven wave. The dynamics of the SH will be investigated in much more detail later in Sec. 6.5, where we in particular study the case where the phase-mismatch is in the resonant range, leading to resonant radiation in the *e*-polarization.

At the time of the early feasibility studies of pulse compression in type I BBO and LN, we discovered that LN in the type 0 configuration (cascaded SHG with $ee \rightarrow e$ interaction) had a very large potential for observing self-defocusing solitons [129]. Again we focused on 800 nm but in spite what the simulations promised the experiments did not show any signs of soliton formation. This turned out to be because the nonlinear Kerr refractive index we used was too low: experimental data had it measured to be $n_2^{\text{SPM}} = 15 \cdot 10^{-20}$ m^2/W at 800 nm [130], but based on our knowledge today we believe that $n_2^{\text{SPM}} = 54 \cdot 10^{-20}$ m^2/W at 1400 nm must be used (for the SPM *e*-polarization interaction) [11, 14]. We also found that Raman effects are strong in LN (in contrast to BBO where they seem not to matter) and estimate the Raman fraction $f_R = 0.35$. Thus the Kerr electronic nonlinearity responsible for SPM $(1 - f_R)n_2^{\text{SPM}} = 35 \cdot 10^{-20}$ m^2/W is

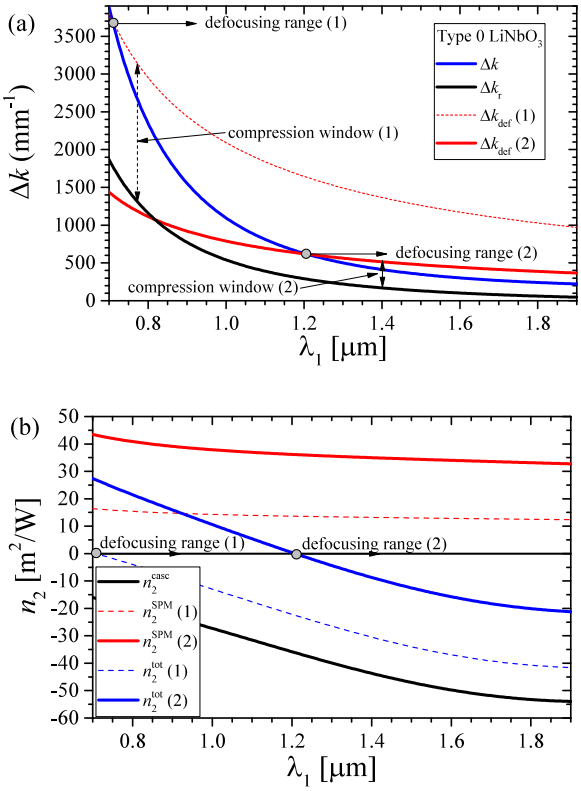

Figure 5.7: Operation regimes for type 0 cascading in LN showing (a) the compression window and (b) the nonlinear refractive indices vs pump wavelength. Two values of the Kerr SPM nonlinearity are shown: case (1) corresponds to the Kerr value $n_2^{\mathrm{SPM}} = 15 \cdot 10^{-20}$ m^2/W@800 nm [130] and case (2) corresponds to the value of the electronic nonlinearity found empirically in our recent work [11, 14] ($n_2^{\mathrm{SPM}} = 54 \cdot 10^{-20}$ m^2/W at 1400 nm, corrected for Raman effects using a $1 - f_R$ prefactor with $f_R = 0.35$).

over 2 times larger than the historical value.

This increased Kerr nonlinearity obviously impacts strongly the parameter regimes where soliton formation is observable, and to evidence this we show in Fig. 5.7 the compression window for LN in the type 0 configuration: in case (1) the phase-mismatch parameter (blue line) enters the compression window just below 800 nm, while in case (2) the happens around 1200 nm. Note here that unlike the type I case the type 0 interaction gives a fixed Δk value because $\theta = \pi/2$ is set to maximize d_{eff}.[3] Remarkably the phase-mismatch value is always in the nonresonant regime since $\Delta k > \Delta k_{\mathrm{r}}$ in the entire range. Because Δk is not tunable, but fortunately always in the non-resonant regime, the only thing that matters is whether the total nonlinearity is defocusing. It is therefore enough to

[3] Δk can be tuned slightly with temperature but to get complete control QPM is needed, which we treat in Sec. 6.4.1.

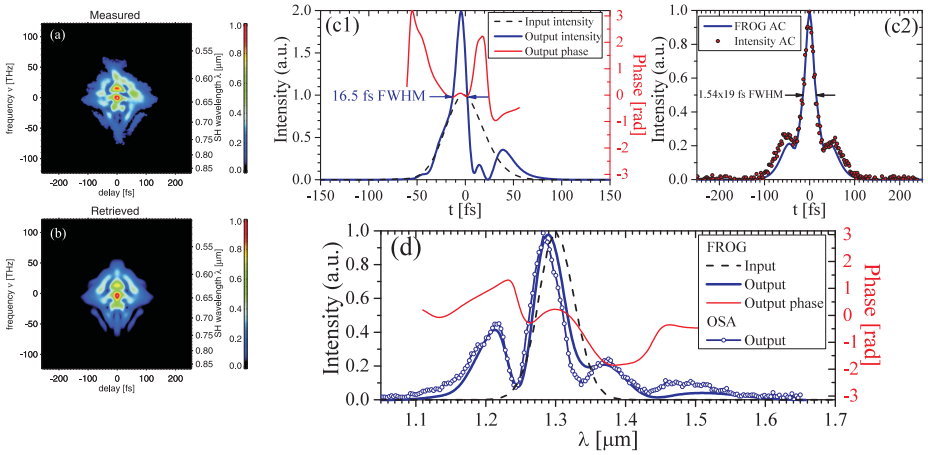

Figure 5.8: Experimental recording of a defocusing temporal soliton in type 0 LN [7]. The 1 mm long crystal was pumped at 1300 nm with 50 fs FWHM pulses having $I_0 = 1.0$ TW/cm^2 (0.46 mm spot size, ~ 125 μJ pulse energy). (a,b) FROG traces (amplitude) of the output pulse. (c1) The temporal and (d) spectral amplitudes and phases retrieved by the FROG algorithm. (c2) The calculated FROG intensity AC and the experimentally measured AC. The crystal was a 5% MgO-doped congruent $LiNbO_3$ (Y-cut, $\theta = 90^\circ$, 1 mm long, 10×10 mm^2 aperture).

show the focusing and defocusing regimes by plotting the nonlinear refractive indices vs wavelength, as seen in Fig. 5.7(b).

Having failed to experimentally observe the defocusing soliton at 800 nm in type 0 LN, we attempted pumping at longer wavelengths using an optical parametric amplifier (OPA). This experiment was conducted at 1300 nm, in part because this is where the OPA has maximum power, and in part because this is the lasing wavelength of Cr:forsterite amplifiers. At this wavelength we immediately observed pulse compression in the intensity auto-correlation trace, which is the first sign of soliton excitation, and noticed also a strong spectral broadening. The complete characterization of the soliton is shown in Fig. 5.8; the 50 fs FWHM input pulses at 1300 nm are compressed to sub-20 fs [7]. The soliton is characterized with a frequency-resolved optical gating (FROG) trace, where (a) and (b) shows the measured and retrieved FROG traces, which agree within 1%. From the retrieval, we get access to the complex field (amplitude and phase), and the pulse intensity and its phase is shown in (c1). A systematic check is that this pulse agrees with the intensity auto-correlation trace measured independently with a separate device, which (c2) confirms. Finally, (d) shows the spectral intensity and phase, and again it is confirmed that the intensity agrees with the spectrum measured by the optical spectrum analyzer.

The soliton based on the spectrum (d) and the auto-correlation trace (c2) looks similar to the BBO case in Fig. 5.5. However, the temporal FROG trace (c1) reveals a more complex structure. One immediate explanation is that the solitons were measured at different stages. In the BBO case the goal was to confirm its presence and not to measure the soliton right at its self-compression stage. Compare the BBO simulations in Fig. 5.6 how the pulse looks like at the self-compression point, where the pulse shape is less symmetric and clean. Having clarified this, let us analyze the LN soliton:

Firstly, the soliton is asymmetric as the leading edge is uncompressed and the trailing edge has indications of shock-front formation. This is not uncommon at the soliton self-compression stage, especially for cascading defocusing solitons, and a similar shape is in fact seen also in the BBO simulation at the self-compression stage.

Secondly, the asymmetric pulse makes it hard to properly define the FWHM duration, especially because the leading edge pedestal sets in just at the half intensity point. The 16.5 fs duration is therefore indicative, and a more fair value reflecting the various results from different fitting routines is 17 ± 2 fs. This also clarifies somewhat the autocorrelation result, where we observe roughly 30 fs FWHM in both cases. As it is well known, this value for a simple pulse shape can be converted into an intensity FWHM, and the conversion factor for a sech^2 shaped pulse is 1.54. This gives the indicated 19 fs in (c2). However, it is also clear from the FROG trace that the pulse shape is not really that simple. Therefore the conversion factor should be considered indicative.

Thirdly, beyond the soliton trailing edge there is a clear secondary peak. The explanation lies in the fact that the Raman effect of LN is quite strong; as mentioned above we have empirically found it accounts for 35-50% of the "DC" Kerr SPM nonlinearity and finding this value was to a large part rooted in trying to corroborate the experimental soliton in Fig. 5.8 and the ensuing supercontinuum (see more in Sec. 7.1). Such a strong Raman effect is well beyond what is seen in glasses and besides the bandwidths of the Raman lines in a crystal are much narrower than those of glasses. This means that the result cannot be interpreted based on literature results. We here show new simulations that help clarify what was originally discussed in [7].

To understand why a secondary peak appears on the trailing edge, we show in Fig. 5.9 the results of a simulation of the soliton experiment using the NAEE code. The time trace after 1 mm confirms the pulse shape observed experimentally, having a 13 fs FWHM duration and the same trailing pedestal. We do note that slightly later the soliton has experienced full compression to sub-10 fs, but where the pulse profile is less consistent with the FROG trace. This could indicate that we measured the soliton slightly before the self-compression point (the intensity control in the experiment was not at all continuous as neutral-density filters were used). At the self-compression point the spectrum shows significant broadening and is shifted towards the ZDW; this is due to Raman. In fact, we see in the time trace that two solitons are eventually generated, both red-shifted all the way up to the ZDW so they end up at the same group velocity in the time trace (explaining the spectral beatings just below the ZDW). Interestingly, we can see in the spectrum where each soliton "hits" the ZDW wall, marked with (1)-(2), and correspondingly we have marked the solitons in the time trace. It is not entirely clear from this figure how the secondary soliton forms, as it does not seem like ordinary soliton fission, and we will investigate this below. However, the presence of 2 solitons actually explains why we did not manage to do like the BBO case, i.e. get clean autocorrelation traces of the stabilized soliton with thicker crystals. In the spectrum we also note the mid-IR resonant radiation peak at 3 μm, investigated more in Chapter 6.

Coming back to the trailing edge peak at the compression point, we believe it is caused by the Raman nonlinearity being unusually strong, having the opposite sign of the instantaneous nonlinearity and due to the *nonlocal* delayed nature of the Raman response. These things combined gives a strong focusing nonlinearity that acts only on the trailing edge, causing a chirp reversal and thus preventing soliton formation. This argument follows

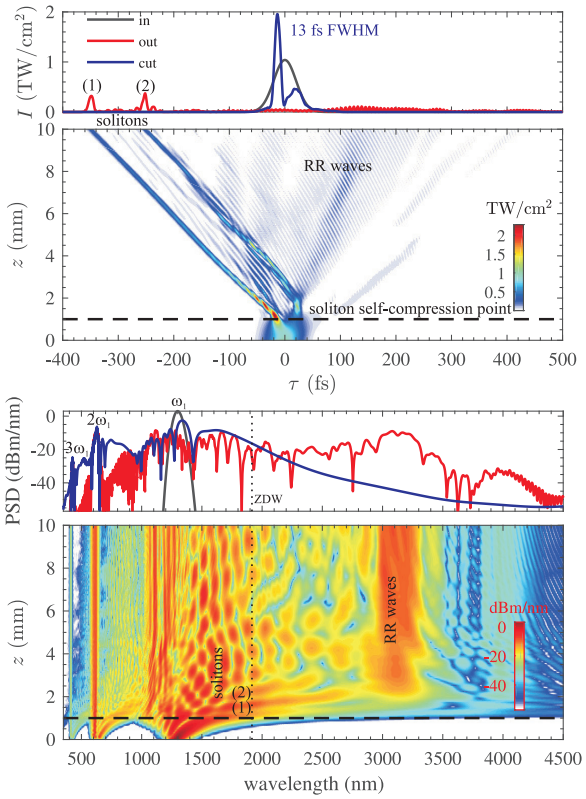

Figure 5.9: Numerical simulation of the soliton experiment in Fig. 5.8 using the NAEE (2.10), $I_0 = 1.04$ TW/cm^2, pulse prechirp -340 fs^2, bandwidth 59 nm (chirped duration 52 fs FWHM). Note the NAEE gives all the harmonics in one single field, which is why in the time trace the harmonics below 1000 nm have been filtered away to avoid interference fringes in the time plot. Note we here used the Kerr nonlinearity values of the later papers [11, 14], $n_2^{\rm SPM} = 54 \cdot 10^{-20}$ m^2/W, $f_R = 0.35$, and we only changed $d_{\rm eff} = 27$ pm/V.

the logic of our recent investigation into pulse splitting and multiple compression stages in gas-filled hollow-core fibers when the gas is becoming ionized [131]. To support the argument we are going to make, consider the cascading NLSE equation (3.25); neglecting self-steepening and considering only the local limit of the cascading we get in the dimensionless form

$$(i\partial_\xi + \hat{D}'_{\omega_1})U_1 - \overbrace{[N^2_{\rm casc} - \underbrace{(1-f_R)N^2_{\rm SPM}}_{\text{Kerr inst.}}]}^{\text{total inst. SPM}} U_1|U_1|^2 + \underbrace{f_R N^2_{\rm SPM}}_{\text{Kerr vibr.}} U_1(\tau') \int_{-\infty}^{\infty} dt' h'_R(t')|U_1(\tau - t')|^2 = 0 \quad (5.20)$$

We remark that the instantaneous (electronic) Kerr SPM is reduced by $1 - f_R$, giving

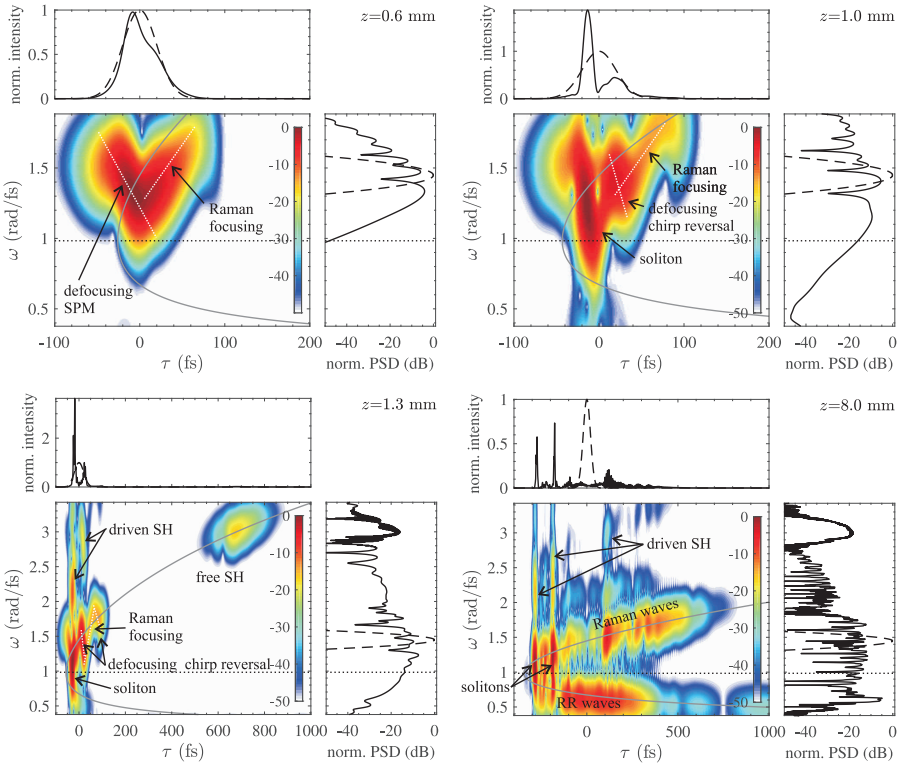

Figure 5.10: Spectrograms at selected proapgation distances of the simulation in Fig. 5.9. The gating pulse was 10 fs FWHM. In the initial stages only the near-IR and mid-IR spectral ranges are shown as to focus on the soliton while in the last stage the SH range is shown as well. The gray line denotes the GVM line $\omega = [k^{(1)}(\omega) - k_1(\omega_1)]z$.

the electronic, instantaneous, nonlinearity. This is because the experimentally measured $n_2^{\rm SPM}$ is (in most cases) the "DC" value in the long-pulse limit.[4] The important point to emphasize is that in the NLSE above the Raman response is much stronger than in, e.g., optical fibers. In silica fibers $f_R = 0.18$, making the electronic nonlinear response 5 times stronger than the vibrational one. Here, not only is $f_R = 0.35$ but the instantaneous total nonlinearity is $N_{\rm casc}^2 - (1-f_R)N_{\rm SPM}^2$, which in some cases is significantly smaller than the vibrational nonlinearity $f_R N_{\rm SPM}^2$. In the specific case we have $N_{\rm casc}^2 = 79$, $N_{\rm SPM}^2 = 89$, making $N_{\rm casc}^2 - (1-f_R)N_{\rm SPM}^2 = 21$; thus the vibrational nonlinearity is 50% *larger* than the electronic one (as opposed to 5 times *smaller* in the silica fiber case). On top of this, we also remind that the Raman nonlinearity has the opposite sign of the instantaneous nonlinearity.

The final part of the argument is the nonlocal action of the Raman effect: we have

[4]This limit is quite specific: when the pulse bandwidth is narrower than the frequency of the lowest Raman mode, the measured Kerr nonlinearity would be the DC value. For LN the lowest Raman mode is 7.5 THz, corresponding to pulses over 200 fs FWHM would be in the long-pulse limit.

an instantaneous (local) SPM that gives a defocusing nonlinear phase-shift in the pulse center. If we carry out the convolution of the Raman effect, however, it can be shown that it is acting some 10-15 fs delayed from the pulse center. This is not unusual, but the difference with the classical fiber case is that the Raman effect here has the opposite sign than the instantaneous nonlinearity, and it is an order of magnitude stronger than in the fiber case. This causes the trailing edge to build up a positive chirp, preventing soliton compression there. We show in Fig. 5.10 cross-FROG spectrograms of the simulation in Fig. 5.9 to support this argument. After 0.6 mm, there is a clear negative chirp on the leading edge from the defocusing nonlinearity. However, the trailing edge shows also a clear up-chirp, due to the Raman effect. At 1.0 mm the leading edge has (almost) completed the soliton formation stage as normal GVD compensates for the negative chirp, but notice here that on the trailing edge the positive chirp starts getting reversed. This is because the trailing edge now becomes affected by the "local" (instantaneous) defocusing nonlinearity (remember that Raman is nonlocal, delayed) and this reverses the chirp. In turn the Raman effect keeps extending the positive chirp on the trailing edge. At 1.3 mm we show a zoomed out spectrogram, where the SH range is included (only the third harmonic is not shown). Here the chirp reversal on the trailing edge is almost complete, and we actually see another stage forming further out on the trailing edge. It turns out not to have enough energy to form a soliton, but Fig. 6.6(c) shows a case where 3 solitons form. Since we now see also the SH, we can see how the SH is composed of a "driven" wave, locked to the FW group velocity, and a "free" wave (traveling away due to GVM; it lies right on top of the GVM line). Finally, the last spectrogram at 8.0 mm shows that eventually a defocusing soliton forms from the trailing edge uncompressed peak, and the remaining waves from the Raman action on the trailing edge now has formed a trail of radiation following the GVM line ("Raman waves"). These Raman waves do show signs of self-compression since it is clear that the defocusing effect provides chirp reversal and thus eventually a solitonic state may form. These are actually responsible for the blue part of the continuum around the pump frequency. However, due to strong 3WM and 4WM with waves at other frequencies in the trailing part of the entire pulse it seems that these solitonic states deplete and eventually become too weak to be a soliton and hence start to disperse. In the mid-IR a long trail of resonant radiation (RR) waves has formed.

We therefore attribute the secondary peak to this kind of competing nonlinearity where the delayed nonlinearity has the opposite sign of the instantaneous. It is presently not completely clear how the trailing edge reverses sign from positive to negative chirp so quickly, but we have seen in connection with simulations using longer pulses for compression in LN [132] that a 200+ fs pulse envelope breaks up due to a kind of modulation instability into a pulse train, and that this was connected to Raman. It might be that the modulation instability gain is present even for such short pulses we investigate here. An obvious analogy appeared recently in gas-filled hollow core fibers where the plasma formation gives a nonlocal delayed defocusing effect that competes with the local instantaneous focusing effect [131]. However, in that case the chirp reversal seemed to appear because the plasma turned off right after the soliton was compressed, leaving SPM to reverse the chirp on the uncompressed trailing edge.

There is therefore a lot of interesting physics going on during and after the compression stage. In addition we also emphasize the importance of the type 0 scheme, which is naturally free of spatial walk-off between the FW and SH. This implies that much lower

pulse energies can be used as the beam can be focused more tightly, and we also note that in the 50 fs case we investigated the soliton forms in a just 1 mm long crystal, which is massively shorter than the 20+ mm crystals needed in the type I BBO case. That being said, the obvious pulse splitting at the compression stage and the typical formation of multiple solitons means that the method as a tool to compress pulses to few-cycle duration is less attractive than in crystals like BBO.

5.4 Soliton compression at various wavelengths

Our early results focused on 800 nm, first of all to understand the potential of BBO. This showed that the experimental results of Ashihara et al. [23] could not be improved further, and the explanation was that soliton formation happened in the resonant regime with significant self-steepening. LN turned out not to work either there, as both the type 0 and type I cases have too high Kerr nonlinearities to work at this wavelength.

Around 1.0 μm BBO is much more promising. One problem so far in actually pursuing this is that Yb-based laser amplifiers (fiber or solid state) typically have 200-300 fs FWHM duration, which requires very long BBO crystals to compress the pulses. This leads to very strong requirements of a large beam size due to spatial walk-off (as this is non-zero in the type I configuration) and since a quasi-collimated beam is required it is difficult to avoid diffraction [132]. This ultimately results in requiring a high pulse energy, typically beyond what fiber amplifiers can deliver. Another practical problem is that BBO crystals are typically not much longer than 30 mm, meaning that two or three crystals must be stacked together to do pulse compression with 300+ fs pulses.

Ultimately the best BBO results were achieved around 1300 nm, where GVM is quite small and the cascading nonlinearity can be taken very large without entering the resonant regime. LN in the type 0 configuration also works really well at this wavelength, with the added bonus of zero spatial walk off and very short crystals. The main issue with LN is the Raman effect, causing pulse splitting. Soliton compression in type 0 LN works up to 1.8 μm, close to the ZDW. In the type I case this regime should also work, especially with QPM [28], but it has not been pursued by us because it seems unlikely that few-cycle solitons can be achieved.

Beyond 2.0 μm we have only attempted excitations of solitons in the $LiInS_2$ crystal in connection with a supercontinuum experiment. We attempted to measure and characterize the soliton, but the home-built autocorrelator was not able to show clear signs of a clean soliton. This might also be connected to similar issues as in LN, i.e. pulse splitting due to Raman effects, but we did not pursue it further since the soliton was not the main focus in that experiment.

Chapter 6

Defocusing soliton-induced resonant radiation

Jigsaw falling into place
So there is nothing to explain

Radiohead “Jigsaw Falling Into Place”

As we have seen in the soliton experiments in Sec. 5.3 the soliton-self compression stage is accompanied by a peak beyond the ZDW. This phenomenon is known as soliton-induced resonant radiation (RR), and in previous literature RR waves have also been known as dispersive waves, or optical Cherenkov radiation.

RR waves were originally considered a radiative perturbation of the pure soliton state [133, 134], but has later been understood as a crucial part of soliton-based supercontinuum generation [124, 135] where it provides a coherent extension of the continuum through phase-matching with the soliton. Excellent reviews of the process in fibers are found in [136, 77].

In a typical fiber dispersion landscape, the focusing soliton in the anomalous dispersion region couples to the RR wave in the normal dispersion regime towards the blue. If the fiber has 2 or more ZDWs then an RR wave can also be found towards the red. However, observing RR waves in the mid-IR has been a challenge since silica fibers have the IR loss boundary beyond 2.2 μm, and only recently progress has been made on silicon-photonics based platforms where RR waves in the mid-IR have been predicted [137].

Therefore the defocusing soliton is interesting in this context alone, because since it naturally exists in the normal dispersion region, it will couple into an RR wave beyond the ZDW in the mid-IR without any need for tailoring the dispersion profile of the nonlinear material. In fact, the first prediction of mid-IR RR waves were made by us in bulk crystals (BBO and LN) [5, 6], and later observed experimentally [11, 12]. The added benefit of the defocusing solitons in bulk crystals is that we can couple 10s of μJ of energy into the mid-IR RR wave, orders of magnitude more than any other system.

6.1 Phase-matching considerations

The temporal optical soliton is the formal solution to the NLSE in presence of GVD. It provides dispersion-free propagation due to the balance between the nonlinear phase-shift from the Kerr effect and the linear phase shift from GVD. The question is: in presence of only GVD, the soliton is dispersion free, but what happens if it is affected by HOD? It turns out that the soliton keeps the dispersion-free property but the HOD gives phase-matching to resonant radiation at some side-band frequency, which takes a finite amount of energy away from the soliton. Because of this the soliton will adapt, relaxing the peak power and pulse duration to keep the GVD-nonlinear balance, but it will survive the influence of HOD. This was the essential message behind the early theory of RR waves [133, 134].

The phase-matching condition between the soliton and the RR wave can be calculated using perturbation theory. In the defocusing soliton case the calculations are identical to the focusing soliton case, simply because the NLSE is essentially the same except for flipped signs in the GVD and nonlinear terms. These flipped signs do give some significant differences later when the specific phase-matching points need to be calculated, but the approach remains the same.

One approach [134] is to consider that the full soliton dispersion Eq. (5.8) in the NLSE framework is simply given by $k_{\mathrm{sol}}^{\mathrm{NLSE}}(\omega) = q_{\mathrm{sol}}$ and the linear RR wave simply has the dispersion given by Eq. (2.4), i.e. $k^{\mathrm{NLSE}}(\omega) = \tilde{D}_{\omega_1}(\omega) = k_1(\omega) - k_1^{(1)}(\omega_1)(\omega - \omega_1) - k_1(\omega_1)$. This gives the well-known phase-matching condition

$$\sum_{m=2}^{\infty} m!^{-1}(\omega_{\mathrm{RR}} - \omega_1)^m k_1^{(m)}(\omega_1) = q_{\mathrm{sol}} \tag{6.1}$$

Essentially the soliton wave number is usually only changing the condition marginally and is therefore often neglected, so all one has to do is to find the roots of the dispersion operator to locate the phase-matching conditions. A more rigorous approach was taken by Skryabin and Yulin [138]: they took the ansatz $U_1(\xi,\tau') = U_{1,\mathrm{sol}}(\xi,\tau') + g(\xi,\tau')$, where g is the linear wave, and put it into the NLSE in presence of HOD. This resulted in the same condition as above, but by additionally allowing the linear wave to be composed of two components (a weak cw "probe" interacting with the soliton to generate an RR wave) the following generalized phase-matching conditions can be written

$$\tilde{D}_{\omega_1}(\omega_{\mathrm{RR}}) = J[\tilde{D}_{\omega_1}(\omega_{\mathrm{probe}}) - q_{\mathrm{sol}}] + q_{\mathrm{sol}}, \quad J = -1, 0, +1 \tag{6.2}$$

Where $J = 0$ is the usual degenerate FWM condition, while $J = \pm 1$ concerns RR waves generated through non-degenerate interaction between the soliton, the probe and the RR wave.

However, this obscures the physics behind the phenomenon. An important contribution from Skryabin et al.'s work has been to pose an equivalent but more intuitive set of phase-matching conditions that can be put forward by translating back to the stationary lab frame and include the lowest orders of dispersion. This gives [138]

$$k(\omega_{\mathrm{RR}}) = J[k(\omega_{\mathrm{probe}}) - k_{\mathrm{sol}}(\omega_{\mathrm{probe}})] + k_{\mathrm{sol}}(\omega_{\mathrm{RR}}) \tag{6.3}$$

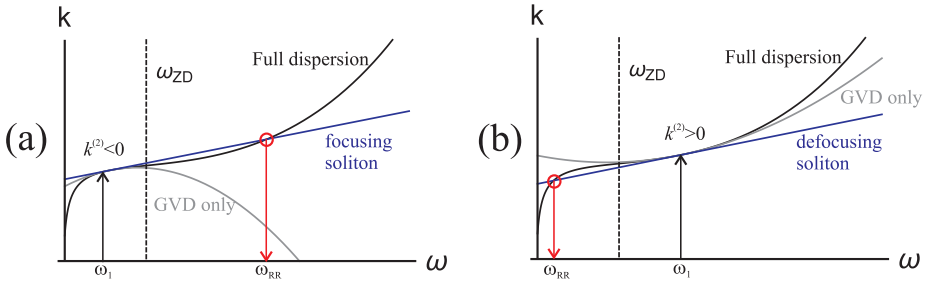

Figure 6.1: Sketch of the dispersion relations leading to the degenerate phase-matching condition for the RR waves, Eq. (6.3) with $J = 0$, in the focusing (a) and defocusing (b) soliton cases.

From this we see that in the degenerate case the RR wave is essentially generated by converting soliton photons *at the RR frequency* into the RR wave. This is extremely important, because it shows it is not an up- or down-conversion of the soliton photons at the soliton center frequency ω_{sol} to the RR frequency, but rather a direct conversion from the soliton wave to the RR wave at that particular frequency. As we shall see later, this is not always so: we can also find RR waves that indeed do rely on up- or down-conversion, cf. Sec. 6.4 and the discussion around Eq. (6.31). Therefore we have to stress that this is not a general result, and rather it is a very particular property of the type of RR wave investigated above, which alone is attributed to the fact that the nonlinearity providing the phase-matching to the soliton is SPM, i.e. a self-acting nonlinearity. This explains why the soliton photons must be found at the RR wave frequency.

It is therefore often in the literature stated that in order to see an RR wave, the soliton spectrum must overlap with that frequency. It also explains why the conversion into the RR wave is mainly happening at the stage where the soliton is self-compressed because this is where the soliton has the broadest spectrum and can therefore efficiently support photons for the conversion process at the often very red- or blue-shifted RR frequencies. In the non-degenerate cases, we see we must also invoke in a similar fashion soliton photons at the probe frequency to carry out the RR wave conversion. We should warn here that all these statements were historically made in connection with the SPM nonlinearity, as this was the only type of nonlinearity considered. As we mentioned earlier, we show later that new RR waves can be phase-matched that do not share these properties because they in fact do rely on up- or down-conversion, cf. Eq. (6.31).

A graphical representation like the one in Fig. 6.1 is at this stage appropriate to explain the role of the soliton dispersion and the linear dispersion, and for simplicity let us consider the degenerate case. The classical focusing soliton exists in the range below the zero-dispersion frequency (ω_{ZD}) where the GVD is anomalous ($k^{(2)} < 0$). The straight-line dispersion of the soliton will not intersect with the material dispersion except if HOD is included. In that case, the RR wave can be phase-matched and it always happens beyond ω_{ZD}, i.e. towards the blue in the normal dispersion regime. For the defocusing soliton the soliton dispersion is graphically not much different, but it now exists in the blue side of ω_{ZD} where the GVD is normal ($k^{(2)} > 0$). When including HOD it can becomes phase-matched to an RR-wave located towards the red, beyond ω_{ZD} in the anomalous dispersion regime. This is the property that allows us to use near-IR lasers to

excite solitons and observe phase-matched RR waves in the mid-IR range.

A practical approach when estimating q_{sol}, cf. Eq. (5.7), for calculating phase-matching conditions is to forget about soliton orders and input durations, and instead consider them as fundamental solitons with $N_{\mathrm{tot}} = 1$, having the intensity I_{sol} and the duration T_{sol}, i.e. $A_{1,\mathrm{sol}} = \sqrt{I_{\mathrm{sol}}}\mathrm{sech}(\tau/T_{\mathrm{sol}})$. This then gives the simple expression

$$q_{\mathrm{sol}} = -\frac{k_1^{(2)}}{2T_{\mathrm{sol}}^2} = -(2L_{D,\mathrm{sol}})^{-1} \tag{6.4}$$

Depending on soliton duration different soliton wavenumbers can then be estimated; typically we see stabilized solitons propagating with durations of 3-4 optical cycles while solitons ejected from parent solitons by soliton fission typically have pulse durations twice that. This approach is convenient in a complex case like cascading where the nonlinear phase shift has multiple contributions and especially the Raman effect and XPM makes it sometimes difficult to use a meaningful soliton order. We should therefore remind that the two approaches are equivalent, because as we see from the ansatz $T_{\mathrm{sol}} = T_0/N_{\mathrm{tot}}$, and using Eq. (5.6) we can write $q_{\mathrm{sol}} = -k_1^{(2)}[2(T_0/N_{\mathrm{tot}})^2]^{-1}$ which is identical to Eq. (6.4). This is related to the fundamental property of a soliton that its amplitude scales inversely with its duration. So in Eq. (5.7), q_{sol} is found by using the soliton order to predict the final soliton duration, while in Eq. (6.4) q_{sol} is found by using an empirical observation of the final soliton duration. It is here appropriate to mention that the peak intensity and pulse duration of the soliton are not the same as those predicted by the scaling laws Eq. (5.19); the scaling laws tell use how the pulse looks like at the compression stage, while instead q_{sol} relates to the accumulated nonlinear phase leading up to the compression stage. It does pose the challenge that in a compression stage the soliton intensity is increasing, so one could also use a weighted average between I_0 and the peak intensity at the compression stage. In most of our publications we even used directly the peak intensity at the compression stage, which will certainly overestimate the soliton wavenumber.

6.2 Defocusing soliton resonant radiation I: BBO

We first pointed out the presence of defocusing RR waves in soliton compression simulations in BBO [3], and a subsequent detailed presentation was given in [5]. The essential dynamics we presented there is captured in Fig. 5.6: before the soliton formation the spectrum broadens and the maximum bandwidth is at the self-compression point. It is here that the soliton couples energy into the infrared RR wave located around 2.1 μm. The soliton itself experiences blue shift. This is due to self-steepening but also because of recoil away from the ZDW, which acts like a potential wall for the soliton [139]. Remark also that the SH seemingly also has an RR wave just below 1.1 μm. This is not really the case, as this spectral peak is a direct consequence of the fact that this part of the SH spectrum is the driven wave, locked to the FW supercontinuum $|\tilde{U}_2(\omega)|^2 \propto |\mathscr{F}[U_1]|^2$. Thus, this peak is merely the SH mirror of the FW RR wave.

We see that the defocusing soliton gives rise to RR waves in the same principle way as the focusing soliton, except for it being located in the anomalous dispersion regime. It could therefore seem as surprising as to why it was not observed in the first soliton experiments. To explain this, we calculated the phase-matching wavelengths for a range

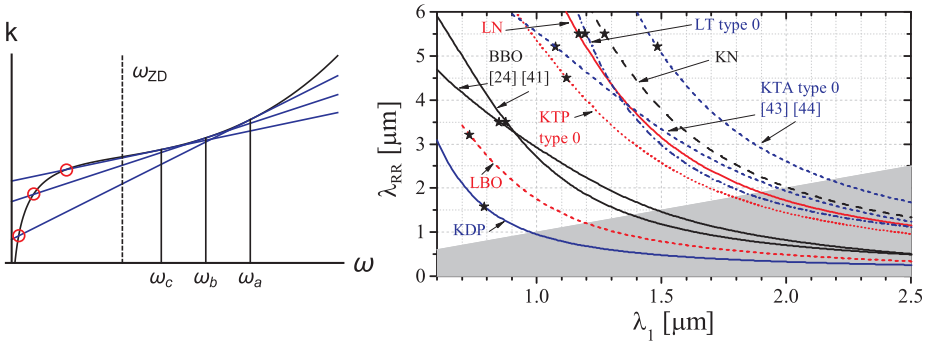

Figure 6.2: Left: Sketch showing how the the defocusing RR phase-matching conditions blue-shifts as the soliton is red-shifted closer to the ZD frequency. Right: RR phase-matching curves to defocusing solitons vs soliton wavelength for various popular quadratic nonlinear crystals as calculated from Eq. (6.2) with $J = 0$ and $q_{sol} = 0$. The gray area denotes the regime with normal GVD where the RR wave requires a focusing soliton. The phase matching considered is type I $oo \rightarrow e$, except where denoted 'type 0', where $ee \rightarrow e$ interaction is considered. The KN and LN curves hold for both type 0 and type I phase matching as they turn out to have almost identical phase-matching curves. The crystals are as follows (the Sellmeier equations are all taken at room temperature and are from Ref. [140], except where noted). KDP: Potassium Dihydrogen Phosphate, LBO: Lithium Triborate, BBO: β-Barium Borate [141, 142], KTP: Potassium Titanyl Phosphate, LT: Lithium Tantalate, LN: 5% Magnesium-Oxide Doped Lithium Niobate [143], KN: Potassium Niobate, KTA: Potassium Titanyl Arsenate [144, 145]. Adopted from Fig. 6 in [5].

of nonlinear crystals [5]. First of all, we note that BBO pumped at 800 nm, the first soliton experiment [23], has an RR wave well beyond the IR absorption edge. However, as the sketch shows on the left, if the soliton is excited closer to the ZD frequency, the RR wave will correspondingly blue shift. Therefore for the 1.26 μm soliton experiment [27] would be optimal for observing the RR wave as it should now be located inside the transmission range, but in that experiment the spectral content beyond 1.7 μm was not measured.

In connection with a similar experiment (pumping at 1.42 μm), Moses and Wise did observe a spectral peak just above the ZDW (again no information was recorded beyond 1.7 μm). This had remained unpublished, but in a collaborative paper we carefully analyzed it [5, Fig. 7] and concluded that this was the red shoulder of the SPM broadened FW that had leaked into the anomalous dispersion regime, and therefore not an RR wave. In a recent experiment [12], shown in Fig. 6.3, we were able to follow up on this study and fully characterize the entire supercontinuum up to 2.5 μm; it shows over an octave of bandwidth, and importantly two clear peaks beyond the ZDW. Clearly pumping so close to the ZDW the simulation in (b) shows that the red SPM shoulder is leaking into the anomalous dispersion range (just as the early data by Moses and Wise), and by treating it as a "probe" wave we can analyze the phase-matching conditions with the soliton in the normal dispersion range, and verify that the 2.0 μm peak is indeed a $J = +1$ non-degenerate RR wave.

The fact that [27] did not measure the spectral content beyond 1.7 μm undoubtedly prevented the first RR wave observation. It is only recently that we gained the possibil-

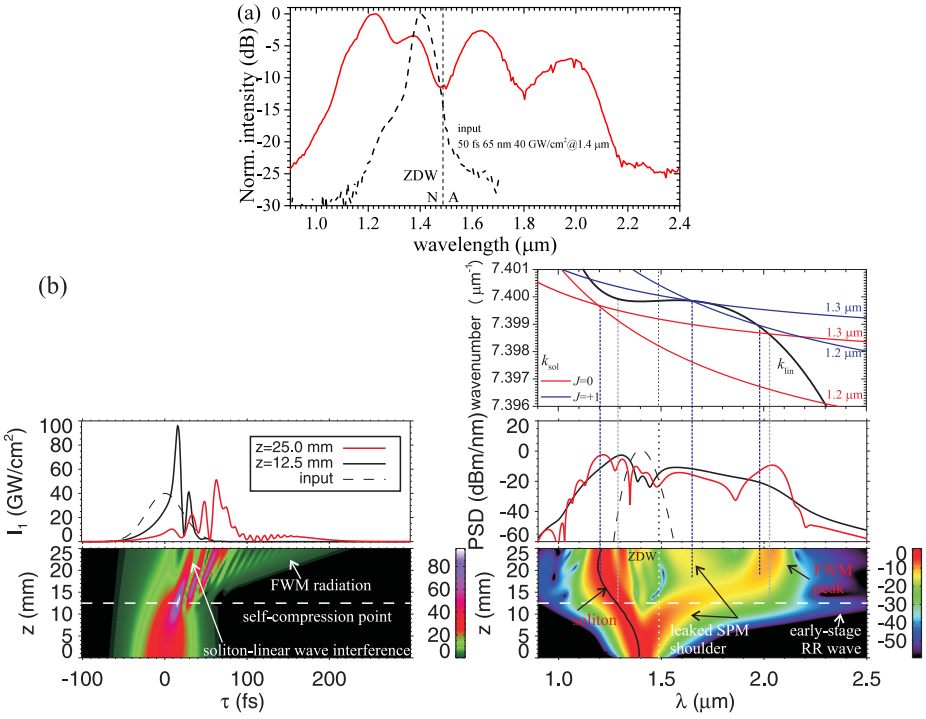

Figure 6.3: (a) Experimental observation of non-degenerate RR waves in BBO using $\lambda_1 = 1.4\ \mu$m, $I_{in} = 40$ GW/cm^2, and $\Delta k = 10$ mm^{-1}. (b) Simulation of the experiment showing the *o*-polarized evolution using the same duration and bandwidth of the experiment (50 fs FWHM and 65 nm, chirp parameter $C = -0.6$). The black line tracks the pump/soliton maximum wavelength. The plot above the spectral evolution shows the phase-matching curves are plotted in the moving reference frame for $\lambda_{sol} = 1.4\ \mu$m for both a degenerate ($J = 0$) and non-degenerate ($J = +1$) case (using a probe wave located at 1.65 μm). Two different soliton wavelengths are shown to gauge the impact of the soliton blue shift. Adapted from [12].

ity of routinely characterizing the mid-IR spectral range so that the cascading RR waves could be pursued experimentally. The experiment behind the results in Fig. 5.5 and 6.3 was indeed designed to observe the degenerate ($J = 0$) RR wave in BBO. In Fig. 6.4 we show a typical experimental result (similar to the one presented in Fig. 5.5, except $\Delta k = 10$ mm^{-1}), and now the RR wave is showing a much more distinct peak beyond the ZDW. In the simulation in (b) the degenerate RR wave formation is confirmed: as the soliton compresses the RR wave is formed when the spectrum is broadest, and after that the slower group velocity of the RR wave means that it experiences temporal walk-off from the soliton: they never interact again. This is an interesting difference with focusing solitons, where the soliton and the RR wave continuously bump into each other (in part because Raman effects slows down the focusing soliton). Notice also the significant shock-front formation on the trailing edge at the compression point; this is much more pronounced than in Fig. 5.6 because Δk is smaller. The spectral position of the RR wave

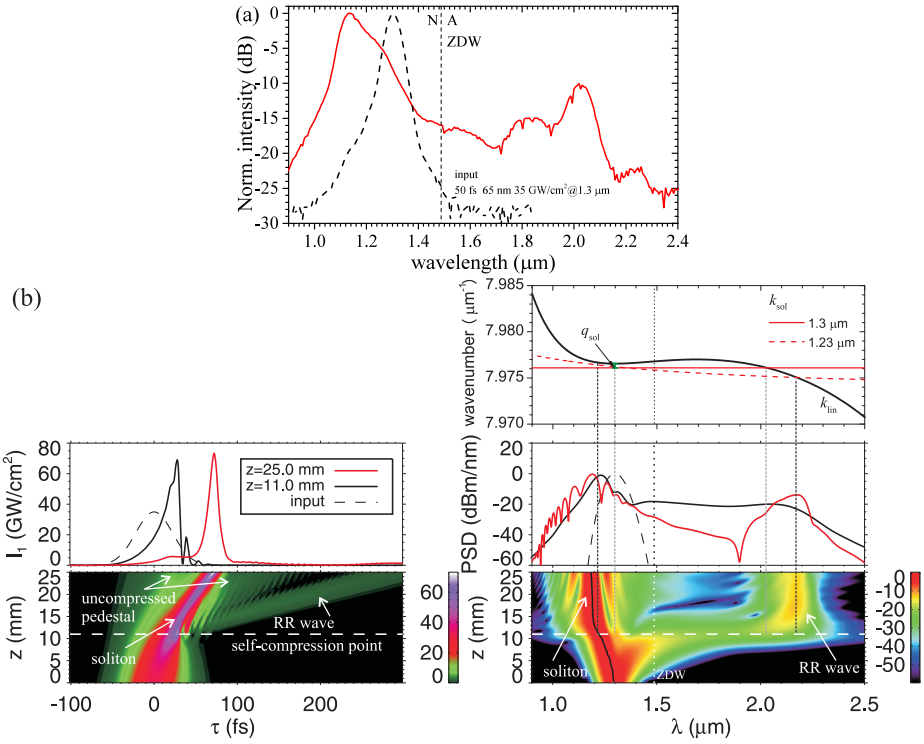

Figure 6.4: (a) Experimental observation of a degenerate RR wave in BBO with the same parameters as in Fig. 5.5, except $\Delta k = 10$ mm^{-1}. (b) Simulation of the experiment showing the o-polarized evolution using the same duration and bandwidth of the experiment (52 fs FWHM and 65 nm, $C = -0.9$). The phase-matching curves are shown for $\lambda_{sol} = 1.3$ μm for degenerate ($J = 0$) interaction, plotted for two different soliton wavelengths. Adapted from [12].

agrees well with the phase-matching curves. The offset q_{sol} is indicated in the figure, and it was calculated by using $I = 80$ GW/cm^2; this is over a factor 2 larger than the theory indicates (where $I_0 = 35$ GW/cm^2 should be used) but despite this clearly it does not change the phase-matching point much.

The soliton is dominating the time trace, where the RR wave is barely visible on a linear scale at the crystal exit. This is of course also consequence of the dispersive nature of the RR wave: as it propagates it spreads out temporally. Here it is also worth underlining that the spectrum shows that the RR wave is located at around -10 dB, which indicates that up to 10% of the energy is in the RR wave. This is not far off what we estimate experimentally by isolating the RR wave with long-pass filters, and it underlines that the RR wave is not just a minor perturbation but actually can contribute substantially to the supercontinuum and in fact act as a frequency conversion process on its own. In some sense, it also underlines how remarkably resilient the soliton is to quite strong interactions with other waves.

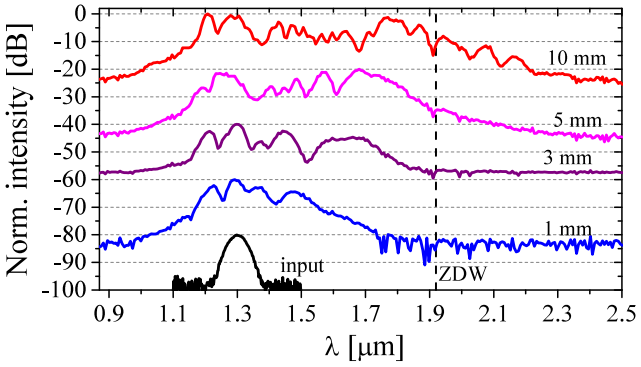

Figure 6.5: Experimentally recorded spectra in LN with various lengths using 1.3 μm 50 fs and 1.04 TW/cm^2 peak intensity. A 20 dB offset per curve is provided for sake of presentation. Adapted from [7].

6.3 Defocusing soliton resonant radiation II: LN

The soliton-induced RR waves is of course one of the secrets behind the success of supercontinuum generation, but a paradigm shift came when it was shown that in hollow-core gas-filled fibers a remarkably efficient conversion from the near-IR soliton to a UV RR wave [146]. These stunning numerical results were later corroborated experimentally [147, 148], showing that RR waves can indeed be considered an efficient frequency conversion tool to wavelength ranges where ultrafast lasers do not operate.

When [146] was published, we were therefore immediately inspired to look for RR waves in the elusive mid-IR range [5]. The added incentive was that defocusing solitons seemed to be the only solution to get mid-IR RR waves as focusing solitons always will be phase-matched towards the visible and UV except under strong waveguiding conditions, and certainly no waveguides or fibers could match the pulse energies that can be handled in a bulk crystal.[1]

Fig. 6.2 helped us in providing a road map to observe a defocusing soliton-induced RR wave in the mid-IR. It stood out that BBO could not give much access to the mid-IR due to the absorption edge, so we focused instead on the various crystals in the niobate family, and especially LN stood out due to the possibility of obtaining RR waves in the range from $2-5$ μm and because we were already conducting soliton experiments in LN. A feasibility study of mid-IR RR waves in LN was published in [6]; there we used the knowledge gained in the soliton experiment [7] (cf. Sec. 5.3), especially concerning the material nonlinearities and the strong Raman effect, and showed that the LN crystal should support RR waves in the mid-IR range up to 4.5 μm. We also saw up to 25% conversion rates, notably when the pump is close to the ZDW so the soliton couples to a RR wave immediately on the opposite side of the ZDW (cf. also the sketch in Fig. 6.2). The efficiency is obviously higher in this case as the spectral overlap at ω_{RR} with the soliton is much stronger.

[1] This was true then and remains true today, although recently a mid-IR RR wave has been seen numerically in hollow-core gas-filled fibers [149]. This occurs due to a modified phase-matching condition as an ionization term starts to contribute under high intensities but so far the efficiency is well below 0.1%.

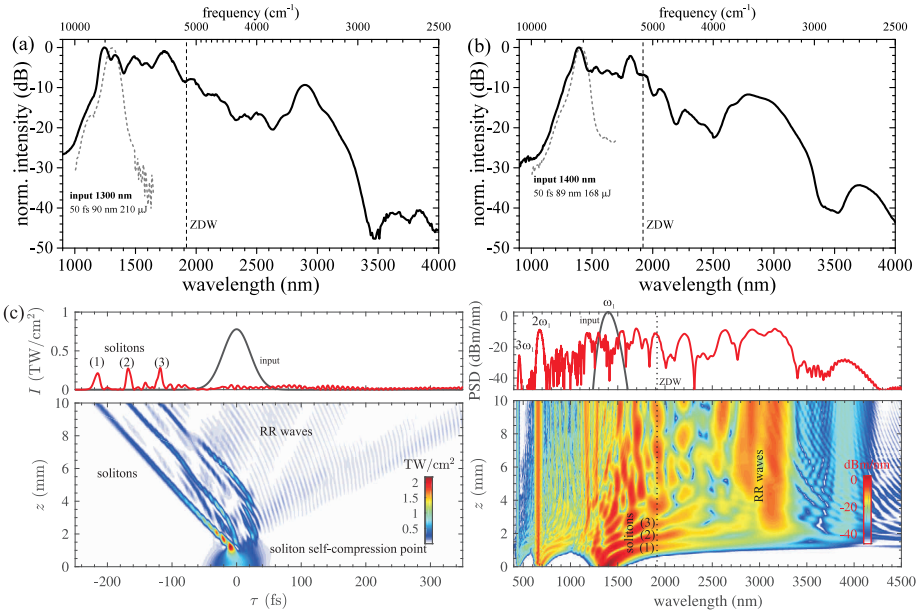

Figure 6.6: Mid-IR RR waves in LN from a near-IR defocusing soliton. A 10 mm LN was used with 50 fs pump pulses loosely collimated to 0.6 mm spot size. The input pulse was $I_0 = 1.0$ TW/cm^2 at 1.3 μm (a) and $I_0 = 0.8$ TW/cm^2 at 1.4 μm (b). (c) Numerical simulation of the case (b) using the NAEE (2.11); note that the higher harmonics have been filtered away from the time trace to avoid oscillations on the envelope from the driven harmonics fields. Compared to the SEWA simulation in [11] we only changed $d_{\text{eff}} = 27$ pm/V (the specific parameters are thus the same as Fig. 5.9). Adapted from [11].

At the same time, we conducted the soliton experiment in LN, and trying to look for possible signs of the RR wave we recorded the spectrum for the same intensity we used to excite the defocusing soliton at 1 mm, and then use progressively longer crystals. The result is summarized in Fig. 6.5, and we see that the spectrum does progressively expand as the crystal gets longer. The 10 mm case even shows significant spectral content in the anomalous dispersion range, whereas the 5 mm case seems to have a spectral tail. In the 1 and 3 mm cases the spectrum beyond the ZDW was most likely below the noise floor of the spectrometer. While these spectra eventually become octave-spanning, it is also clear that the RR wave is not observed. The strongly red-shifted spectrum for longer crystals is due to the soliton becoming Raman red-shifted, but it does not lead to any distinct RR waves below 2.5 μm.

We therefore acquired a grating monochromator (FPAS-1600 spectrometer, Infrared Systems) with a cooled HgCdTe (MCT) detector connected with a box-car integrator, and using long-pass filters to selectively cover the $2-6$ μm range in the mid-IR (to avoid ghost harmonic signals). The detection across the mid-IR range was carefully calibrated with a black body source. The InGaAs CCD-based spectrometer was used for wavelengths below 2.3 μm, and the entire spectrum was stitched together by appropriate overlapping

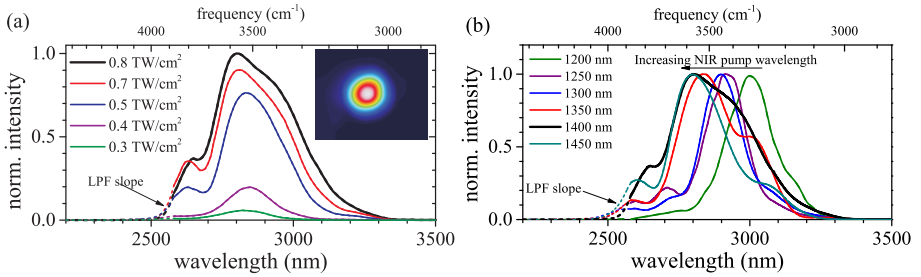

Figure 6.7: Dynamics of the experimentally observed mid-IR RR waves, recorded using a long-pass filter (LPF, cut-on wavelength 2.4 μm). The filtered spectra are plotted on a linear scale. (a) Evolution of the spectrum for $\lambda_1 = 1.4$ μm and sweeping the pump intensity, but without changing the neutral density filter; the spectra are normalized to the peak intensity of the 0.8 TW/cm^2 case. Inset: beam profile of the filtered MIR pulse at 0.8 TW/cm^2. (b) Normalized spectra recorded under various near-IR pump wavelengths and using the maximum intensity available. Taken from [11, Fig. 2].

of concurrent ranges. Examples of mid-IR RR waves are shown in Fig. 6.6, where we now clearly see the RR waves forming in the mid-IR. We show both the 1.3 μm case corresponding to the earlier experiment, as well pumping at 1.4 μm. In both cases the near-IR spectrum containing the soliton(s) has broadened right up to the ZDW, as we saw earlier in Fig. 6.5, which is due to the Raman effect, while little-to-none broadening is seen towards the blue.[2] This is also confirmed in the simulation in (c), modeling the 1.4 μm case. It is quite similar to the simulation in Fig. 5.9 for the soliton compression discussion: we see a train of three solitons, all red-shifted up to the ZDW. The spectrum shows where each soliton "hits" the ZDW wall, marked with (1)-(3), and correspondingly we have marked the solitons in the time trace. The strong RR wave at $2.5-3.2$ μm is therefore actually composed of multiple emissions as each of the 3 solitons radiate into the mid-IR. The simulation also confirm the peak between $3.5-4.0$ μm, and detailed analysis reveals it is a weak RR wave emitted in the very early stage of the propagation by the main soliton.

Remarkably, despite the pump being deep into the near-IR, the RR waves are peaked around -10 dB, and we measured over 10 μJ energy in each of the mid-IR spectra above 2500 nm (corresponding to 5-6% efficiency). This is notably not really limited by any fundamental effects, because unlike filamentation it is entirely possible to increase the energy to the mJ level by simply using a bigger spot size in a larger-aperture crystal. In Fig. 6.7(a) we show specifically how the mid-IR RR wave grows in strength as the input intensity is increased. The spectra are shown on a linear scale and are recorded in one go so the strength can be compared on a relative level. The early sign of the RR wave at 0.3 TW/cm^2 shows that this is close to the soliton threshold (in fact, at 0.2 TW/cm^2 no RR wave could be recorded). At 0.5 TW/cm^2 the RR wave has grown significantly, indicating a secondary soliton has formed, and after this the RR wave only grows another 20% in strength. The inset shows the transverse profile of the RR wave at the peak inten-

[2] We note that the spectrum recorded in [7] at the same intensity, as shown in Fig. 6.5 with a red line, matches on a qualitative level quite well the near-IR part but some differences were seen, which we attribute to the fact that the input bandwidth was around 50% larger than in Fig. 6.5.

sity, displaying excellent beam quality. We should also remark that we measured intensity autocorrelation traces of the filtered RR waves, where quite clean Gaussian-shaped pulses were observed having durations of around 150-200 fs FWHM. It is expected that the RR waves are broadened temporally since they experience dispersion upon propagation, but we also expect to be able to compress them to sub-50 fs duration using GVD compensation with a piece of mid-IR glass. In (b) we show the RR wave (again on a linear scale) for various pump wavelengths; we were able to observe the RR wave all the way down to 1200 nm. The trend observed is that the RR wave blue shifts as the near-IR pump wavelength is increased. This is in qualitative agreement with the trend predicted in Fig. 6.2, but the shift is much smaller than expected from that figure. The main reason is that the soliton strongly red-shifts before and during formation due to the Raman effect, and this shifts the RR waves over a much narrower range. We also remark that the spectra are normalized to unity here, but quantitatively the efficiency changes from 1% to 6% as the pump wavelength goes form 1200 nm to 1450 nm.

6.4 Resonant radiation from quadratic nonlinearities

In connection with modeling the RR waves observed experimentally in LN, we investigated to potential of using QPM control over the phase-mismatch in PPLN crystals for multi-stage soliton compression [150]. During that process we implemented a numerical code that modeled the electric field instead of the envelope [85], and suddenly a new mid-IR wave appeared that puzzled us: It always appeared beyond the mid-IR RR wave around 3.0 μm, it could not be observed in the SEWA code, and we could not find a good explanation behind its phase-matching condition. Finally, it seemed only to appear when we used QPM and not when using a bulk QPM-free crystal, and the QPM pitch could be used to control the spectral position.

To verify what we were dealing with, we decided to throw a PPLN crystal into the beam line of the LN soliton and RR wave experiment that we presented in the previous section 6.3, and after some iterations we found that pumping closer to the ZDW the long-wavelength mid-IR peak in the 4.0-5.5 μm range could indeed be observed for certain QPM pitch values.

It turns out that this is indeed an entirely new type of RR wave, driven by the quadratic nonlinearity rather than the cubic SPM one responsible for the traditional RR wave we have treated so far. It also turns out that the novel RR-waves will not appear in standard coupled-wave equations since they retain only the up-conversion nonlinearity A_1^2 in the SH equation or the down-conversion nonlinearity $A_1^* A_2$ in the FW. Instead, it is necessary to model the full electrical field without any truncation of the nonlinearities. In the coupled-wave equations these additional nonlinear terms are thrown away due to the fast oscillations $e^{\pm i\omega_0 t}$ but we could in principle retain all of them. This is essentially what the NAEE framework is all about. We prefer this type of framework over the approach using a forward-Maxwell equation [96, 85], which we originally used, because as we shall now see retaining the envelope-like equations is advantageous when we want to study the RR wave phase-matching conditions analytically.

6.4.1 Phase-matching conditions

The starting point is the full NAEE Eq. (2.10). For the following phase-matching analysis Raman effects and self-steepening are not relevant, so removing these we arrive at the more simple form

$$i\partial_\zeta A + \hat{D}_{\omega_1} A + \kappa^{(2)}[\tfrac{1}{2}A^2 e^{-i\omega_1\tau - i\Delta_{\rm pg}\zeta} + A^* A e^{i\omega_1\tau + i\Delta_{\rm pg}\zeta}]_+ + \kappa^{(3)}[|A|^2 A + |A|^2 A^* e^{i2\omega_1\tau + i2\Delta_{\rm pg}\zeta} + \tfrac{1}{3}A^3 e^{-i2\omega_1\tau - i2\Delta_{\rm pg}\zeta}]_+ = 0 \quad (6.5)$$

The nonlinear strengths are designated $\kappa^{(2)}$ and $\kappa^{(3)}$, but the values of these as well as the normalization of A are not relevant for the following analysis.

The equations will support a number of phase-matching conditions between a soliton at the pump frequency and a linear (dispersive) wave. The soliton envelope is the exact nonlinear solution in presence of SPM and GVD only. Particular to the cascading case we study here is of course that the soliton is self-defocusing from the total nonlinearity, given by the sum of the Kerr SPM nonlinearity and the cascading nonlinearity. Let us for simplicity denote it $\kappa^{(3)}_{\rm eff} = \kappa^{(3)}_{\rm casc} + \kappa^{(3)}$, and the self-defocusing nature of the nonlinearity implies that $\kappa^{(3)}_{\rm eff} < 0$. Thus, the ansatz $A(\zeta,\tau) = F_{\rm sol}(\tau)e^{iq_{\rm sol}\zeta}$, where $F_{\rm sol}$ is the soliton envelope (which is real), $q_{\rm sol}$ is the nonlinear wavenumber of the soliton, solves the following self-defocusing nonlinear Schrödinger equation (see also Sec. 5.2.2)

$$i\partial_\zeta A - \tfrac{1}{2}k_2(\omega_s)(\partial_\tau)^2 A + \kappa^{(3)}_{\rm eff}|A|^2 A = 0 \quad (6.6)$$

As we saw earlier, a consequence of the self-defocusing negative nonlinearity is that $q_{\rm sol} < 0$, cf. Eq. (5.6). Another direct consequence is of course the requirement of normal dispersion, $k_2(\omega_s) > 0$.

To find the RR phase-matching conditions, we take the extended ansatz [138] $A(\zeta,\tau) = F_{\rm sol}(\tau)e^{iq_{\rm sol}\zeta} + g(\zeta,\tau)$, where g is the dispersive wave. To leading order we get

$$\begin{aligned}(i\partial_\zeta + \hat{D}_{\omega_s})g + \kappa^{(2)}F_{\rm sol}[ge^{i\zeta(q_{\rm sol}-\Delta_{\rm pg})-i\omega_s\tau} + 2{\rm Re}(ge^{-iq_{\rm sol}\zeta})e^{i\omega_s\tau+i\Delta_{\rm pg}\zeta}] \\ + \kappa^{(3)}F^2_{\rm sol}[g^* e^{i2q_{\rm sol}\zeta} + (2g^*+g)e^{i\zeta(-q_{\rm sol}+2\Delta_{\rm pg})+i2\omega_s\tau} + ge^{i\zeta(2q_{\rm sol}-2\Delta_{\rm pg})-i2\omega_s\tau}] = \\ -\sum_{m=3} m!^{-1}k_m(\omega_s)(i\partial_\tau)^m F_{\rm sol}e^{iq_{\rm sol}\zeta} + \kappa^{(3)}_{\rm casc}F^3_{\rm sol}e^{iq_{\rm sol}\zeta} \\ -\kappa^{(2)}F^2_{\rm sol}[e^{i\zeta(2q_{\rm sol}-\Delta_{\rm pg})-i\omega_s\tau} + e^{i\omega_s\tau+i\Delta_{\rm pg}\zeta}] \\ -\kappa^{(3)}F^3_{\rm sol}[e^{i\zeta(-q_{\rm sol}+2\Delta_{\rm pg})+i2\omega_s\tau}e^{i\zeta(3q_{\rm sol}-2\Delta_{\rm pg})-i2\omega_s\tau}] \quad (6.7)\end{aligned}$$

The next step is to find solutions for the dispersive wave g. We can make the ansatz $g(\zeta,\tau) = g'(\zeta,\tau)e^{i\tilde{D}_{\omega_s}(\omega)\zeta - i(\omega-\omega_s)\tau}$, and after neglecting the nonlinear contributions proportional to $F_{\rm sol}$ and $F^2_{\rm sol}$ on the left-hand side, we get the phase matching conditions relating the dispersion on the left-hand side with the nonlinear driving terms on the right-hand side.

For the 4WM terms mediated by the $\chi^{(3)}$ nonlinear terms, the phase-matching conditions are well-known [98]

$$\tilde{D}_{\omega_s}(\omega_{\rm RR}) = q_{\rm sol}, \qquad ({\rm SPM\text{-}RR},\ |A|^2A) \quad (6.8)$$

$$\tilde{D}_{\omega_s}(\omega_{\rm RR}) = -q_{\rm sol} + 2\Delta_{\rm pg}, \qquad ({\rm SPM\text{-}cRR},\ |A|^2A^*) \quad (6.9)$$

$$\tilde{D}_{\omega_s}(\omega_{\rm RR}) = 3q_{\rm sol} - 2\Delta_{\rm pg}, \qquad ({\rm THG\text{-}RR},\ A^3) \quad (6.10)$$

The first condition is the traditional RR induced by SPM, reported above in Eq. (6.1), the second is the "conjugate RR" from SPM (a.k.a. negative-frequency RR), while the third is the "third-harmonic generation RR" or simply THG-RR. We note that apart from our work in quadratic nonlinear crystals [5, 6, 11, 12], the SPM-cRR has been studied numerically [151].

Usually the soliton ansatz will remove the term $\propto F_{\mathrm{sol}}^3$ in Eq. (6.7), see e.g. [98, Eq. (9)]. In our case it remains with the prefactor $\kappa_{\mathrm{casc}}^{(3)}$ because we consider the soliton ansatz that solves a self-defocusing NLSE with a reduced effective nonlinearity, Eq. (6.6). However, it does not change anything for the 4WM phase-matching conditions since its phase-matching condition is identical to the SPM-RR case.

In the same way, our analysis here shows that the 3WM from the $\chi^{(2)}$ nonlinear terms will support the following phase-matching conditions

$$\tilde{D}_{\omega_s}(\omega_{\mathrm{RR}}) = 2q_{\mathrm{sol}} - \Delta_{\mathrm{pg}}, \qquad (\text{SFG-RR}, A^2) \tag{6.11}$$

$$\tilde{D}_{\omega_s}(\omega_{\mathrm{RR}}) = \Delta_{\mathrm{pg}}, \qquad (\text{DFG-RR}, A^*A) \tag{6.12}$$

We note here that there are no "conjugate" RR terms for the 3WM case: the term A^*A is its own conjugate, and the conjugate of A^2 resides for negative frequencies only [97] and is therefore not giving any relevant phase-matching conditions for $\omega > 0$ [and also this is why it does not appear in Eq. (2.10)].

Note that the nonlinear wavenumber of the soliton q_{sol} is not entering the DFG phase-matching condition Eq. (6.12) because as we show below it cancels out as a result of the DFG mixing between the two soliton photons. We stress that it is not an indication that a soliton is not part of the phase-matching condition. In fact a similar effect is well known from 4WM RR, where in the nondegenerate case of a soliton and a linear probe interacting, q_{sol} may also cancel, cf. Eq. (6.2).

In all the non-standard cases, the term Δ_{pg} appears, and it is therefore important to specify that in this context we intend it to be evaluated at the soliton frequency ω_s, i.e. specifically $\Delta_{\mathrm{pg}} = \omega_s/v_{g,\mathrm{sol}} - k(\omega_s)$, where $v_{g,\mathrm{sol}} = 1/k^{(1)}(\omega_s)$ is the soliton group velocity.

For a physical interpretation it is instructive to transform the interaction back to the lab-frame coordinate, because this reveals the direct wave-number phase-matching conditions. In this connection, we use the soliton dispersion relation Eq. (5.8). For the 4WM we get

$$k(\omega_{\mathrm{RR}}) = k_{\mathrm{sol}}(\omega_{\mathrm{RR}}), \qquad (\text{SPM-RR}, |A|^2A) \tag{6.13}$$

$$k(\omega_{\mathrm{RR}}) = -k_{\mathrm{sol}}(\omega_{\mathrm{RR}}) + 2\omega_{\mathrm{RR}}/v_{g,\mathrm{sol}}, \qquad (\text{cSPM-RR}, |A|^2A^*) \tag{6.14}$$

$$k(\omega_{\mathrm{RR}}) = 3k_{\mathrm{sol}}(\omega_{\mathrm{RR}}) - 2\omega_{\mathrm{RR}}/v_{g,\mathrm{sol}}, \qquad (\text{THG-RR}, A^3) \tag{6.15}$$

For the 3WM we get

$$k(\omega_{\mathrm{RR}}) = 2k_{\mathrm{sol}}(\omega_{\mathrm{RR}}) - \omega_{\mathrm{RR}}/v_{g,\mathrm{sol}}, \qquad (\text{SFG-RR}, A^2) \tag{6.16}$$

$$k(\omega_{\mathrm{RR}}) = \omega_{\mathrm{RR}}/v_{g,\mathrm{sol}}, \qquad (\text{DFG-RR}, A^*A) \tag{6.17}$$

Let us discuss these results, because except for Eq. (6.13) they have not been reported in this form before. Exactly Eq. (6.13) is therefore a good place to start: it simply means that the wavenumbers of the soliton and the dispersive wave match at the RR frequency.

However, as mentioned above, all the other phase-matching equations have the term $\Delta_{\rm pg}$ and this leads to the $\omega_{\rm RR}/v_{g,\rm sol}$ terms in the above representations. As we show below, this term represents the group-velocity mismatch (GVM) between the soliton and the harmonic wave of the nonlinear process.

In the two other 4WM cases it is more involved: for the cSPM-RR the phase-matching condition is equivalent to

$$k(\omega_{\rm RR}) = -k_{\rm sol}(-\omega_{\rm RR}) \tag{6.18}$$

i.e., the RR wave is phase-matched to the soliton evaluated at the negative frequency of the RR wave. The explanation behind this peculiar "negative frequency RR" is that because an equivalent to Eq. (2.10) exists expressed by the complex-conjugate system, we can express the "conjugate" defocusing soliton, i.e., the forward-propagating defocusing soliton that solves the complex conjugate equation system, as $k^c_{\rm sol}(\omega) = -k_{\rm sol}(-\omega) = -k(\omega_s) + (\omega+\omega_s)/v_{g,\rm sol} - q_{\rm sol}$, and hence $k(\omega_{\rm RR}) = k^c_{\rm sol}(\omega_{\rm RR})$ gives an equivalent but positive phase-matching frequency [152, 151].

For the THG-RR case, we get

$$k(\omega_{\rm RR}) = k_{\rm sol}(\omega_a) + k_{\rm sol}(\omega_b) + k_{\rm sol}(\omega_c), \quad \omega_a+\omega_b+\omega_c = \omega_{\rm RR} \tag{6.19}$$

which is the 4WM equivalent of an SFG process. The challenge for the THG-RR case is substantial: it turns out to be phase-matched deep in the low-frequency part of the spectrum [98], but nonetheless the analysis here shows that all the contributing soliton photons must have lower frequencies. This explains why it has been elusive to observe even in simulations. To that end, we should mention that recently it was shown [153] that deep into the anomalous dispersion regime the THG-RR wave can become phase-matched above the soliton frequency, which according to the above analysis is much more likely. Such an observation is unlikely in the defocusing case, because there is no equivalent possibility to go deep into the normal dispersion regime and get the THG-RR wave phase matched.

Next let us consider Eq. (6.16) that is a result of the A^2 wave mixing term. It is straightforward to show that it is equivalent to

$$k(\omega_{\rm RR}) = k_{\rm sol}(\omega_a) + k_{\rm sol}(\omega_b), \quad \omega_a+\omega_b = \omega_{\rm RR} \tag{6.20}$$

i.e., the SFG between soliton photons at two different frequencies, constrained of course with energy conservation to give the new frequency. If we expand the dispersion on the left-hand side around the second-harmonic (SH) frequency of the soliton frequency $\omega_2 = 2\omega_s$, we get

$$\tilde{D}_{\omega_2}(\omega_{\rm RR}) - (\omega_{\rm RR}-\omega_2) d^{\rm SHG}_{\rm GVM} + \Delta k_{\rm SHG} = 2q_{\rm sol} \tag{6.21}$$

where $d^{\rm SHG}_{\rm GVM} = k^{(1)}(\omega_s) - k^{(1)}(2\omega_s)$ is the GVM coefficient between the soliton and its SH. $\Delta k_{\rm SHG} = k(2\omega_s) - 2k(\omega_s)$ is the SHG phase mismatch between the soliton and its SH. What is striking about this result is that it is actually equivalent to the resonance condition in the nonlocal analysis, cf. Eq. (3.23). In other words, the SFG-RR wave is formally identical to the resonance peaks that can be observed in the SH spectrum in the nonlocal resonant case.

In the DFG-RR case we can rewrite the phase-matching condition Eq. (6.17) as[3]

$$k(\omega_{\mathrm{RR}}) = k_{\mathrm{sol}}(\omega_a) - k_{\mathrm{sol}}(\omega_b), \quad \omega_a - \omega_b = \omega_{\mathrm{RR}} \tag{6.22}$$

i.e., the DFG between soliton photons at two different frequencies, constrained of course with energy conservation so the difference between them gives the new frequency. When expanding the linear wave dispersion on the right-hand side around some low-frequency value ω_{DFG} the condition becomes

$$\tilde{D}_{\omega_{\mathrm{DFG}}}(\omega_{\mathrm{RR}}) - (\omega_{\mathrm{RR}} - \omega_{\mathrm{DFG}}) d_{\mathrm{GVM}}^{\mathrm{DFG}} - \Delta k_{\mathrm{DFG}} = 0 \tag{6.23}$$

where $d_{\mathrm{GVM}}^{\mathrm{DFG}} = k^{(1)}(\omega_s) - k^{(1)}(\omega_{\mathrm{DFG}})$ is the GVM coefficient between the soliton and the DFG frequency. The DFG phase-mismatch coefficient is given by

$$\Delta k_{\mathrm{DFG}} = k_{\mathrm{sol}}(\omega_s) - k_{\mathrm{sol}}(\omega_s - \omega_{\mathrm{DFG}}) - k(\omega_{\mathrm{DFG}}) \tag{6.24}$$

This shows that again there is a direct connection between the RR wave phase-matching condition and the nonlocal resonance criterion for a DFG process (the latter has been calculated, e.g., in [154]). Note that $\Delta k_{\mathrm{DFG}} \neq 0$ (in fact, in a type-0 interaction in a crystal like LN we will find that we always have $\Delta k_{\mathrm{DFG}} < 0$ just like we always have $\Delta k_{\mathrm{SHG}} > 0$), so the DFG process is heavily phase-mismatched. The RR wave will then appear at the frequency where Eq. (6.23) is zero.

Getting back to the form of the DFG-RR phase-matching condition reported in Eq. (6.17), we can write the left-hand side as $\omega / v_{\mathrm{ph}}(\omega)$, where $v_{\mathrm{ph}}(\omega) = c/n(\omega)$ is the phase velocity at the frequency ω. In this way, the DFG-RR condition becomes a very particular requirement, namely that

$$v_{\mathrm{ph}}(\omega) = v_{g,\mathrm{sol}} \tag{6.25}$$

i.e., that the phase velocity of the RR wave is the same as the group velocity of the soliton. Alternatively it is expressed as $n(\omega) = n_{g,\mathrm{sol}}$ where $n_{g,\mathrm{sol}} = c/v_{g,\mathrm{sol}}$ is the group index of the soliton. Such a condition is well-known from THz generation through optical rectification [155], where it is known as the *velocity-matching condition*. It is not easy to fulfill this condition because the phase- and group-velocities are quite different even when considering that the RR wave is allowed to have any frequency within the transparency region of the crystal. For a fixed soliton frequency it is possible to achieve velocity-matching, i.e. fulfill condition Eq. (6.25), when the RR frequency is higher than the soliton frequency. This because within a certain transparency region all materials have for a fixed frequency the phase index n below the group-index n_g, i.e. that the phase velocity is faster than the group velocity, and additionally both will monotonically increase with frequency. Consequently, the soliton must necessarily look towards higher frequencies to find a wave with an phase-index of the same value. However, through the analysis presented above it is a requirement that the RR frequency is located to the red side of the soliton, $\omega_{\mathrm{RR}} < \omega_s$, otherwise the soliton wavenumbers do not cancel. This requirement practically makes velocity-matching impossible in LN, unless one goes beyond an IR resonance and exploit that on the other side of the resonance in the far-IR transparency window the phase index is sufficiently high to achieve velocity matching. This is essentially what is done in the THz case.

[3] Note that Eq. (9) in [14] has a typo: it should have read $k(\omega_{\mathrm{RR}}) = k_{\mathrm{sol}}(\omega_a) - k_{\mathrm{sol}}(\omega_b)$.

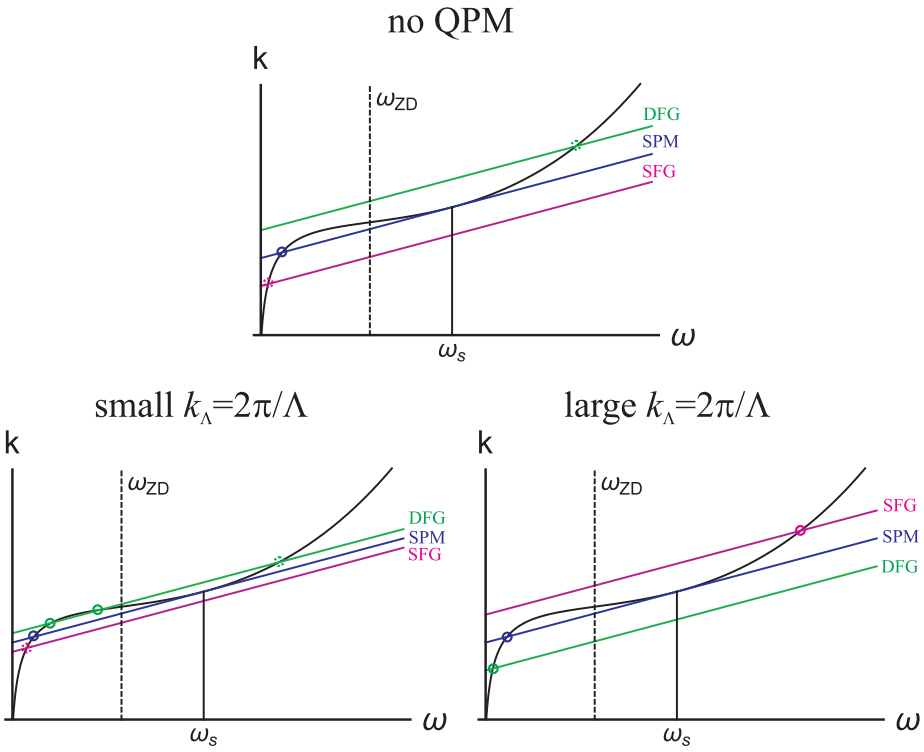

Figure 6.8: Sketches of the main RR wave dispersion relations for a defocusing soliton, originating from 4WM Kerr SPM (degenerate case), as well as the novel 3WM cases due to the SFG A^2 and DFG A^*A terms. The circles mark the predicted RR phase-matching frequencies. The first plot on the left shows the case without QPM, while the next two plots show increasing contributions from QPM (i.e. decreasing QPM pitch values Λ).

To visualize the phase-matching conditions we show qualitative sketches in Fig. 6.8, where the classical SPM condition is plotted together with the new SFG and DFG conditions. As we can see without any QPM the SFG condition is fulfilled for low frequencies. As we discussed above this makes it unlikely to observe RR waves as the SFG condition additionally requires to take soliton photons below the final RR frequency. Vice versa with DFG we conclude that the RR wave cannot be observed since it is phase-matched well beyond the soliton frequency, and it requires taking soliton photons that are larger than the final RR frequency. We have therefore made the circles dotted in the figure.

It is therefore relevant to remind that this is actually in agreement with the nonlocal analysis, where we remind that Fig. 5.7 remarked that no matter where we pumped in bulk type 0 LN, we would always be in the non-resonant regime. This manifests itself here in absence of phase-matching through the SFG nonlinearity. A similar analysis can be done with the nonlocal DFG response.

We therefore need to control the phase mismatch, like the birefringent angle control in the type I case, and find parameter regimes where phase matching is possible. In peri-

odically poled LN (PPLN), the so-called quasi-phase matching (QPM) technique uses a periodic-poling structure of the quadratic nonlinearity to achieve control over the phase mismatch in a type 0 scheme. The effective quadratic nonlinearity has here a grating that is generally expressed as $d_{\text{eff}} g_{\text{QPM}}(z)$, where $g_{\text{QPM}}(z)$ is the normalized QPM grating function. The simplest and most widely used case is where the grating is a square function that effectively reverses the sign of $\chi^{(2)}$ with 50% duty cycle and periodicity Λ. Expressing the square grating in a Fourier series gives

$$\begin{aligned} g_{\text{QPM}}(z) &= \frac{4}{\pi} \sum_{l=0}^{\infty} \frac{1}{2l+1} \sin\left[(2l+1)k_\Lambda z\right] \\ &= \frac{2}{\pi} \sum_{l=-\infty}^{\infty} \frac{-i}{2l+1} e^{i(2l+1)k_\Lambda z} \end{aligned} \tag{6.26}$$

where $k_\Lambda = 2\pi/\Lambda$. We here immediately see the well-known $2/\pi$ prefactor, which is the "penalty" on the nonlinear strength for using a uniform QPM square-grating poling compared to the unpoled case. The general idea behind QPM is that the exponential terms $m_0^{-1} e^{i m_0 k_\Lambda z}$, $m_0 = (2l+1) = \pm 1, \pm 3, \pm 5, \ldots$, contribute to the similar exponential terms in front of the $\kappa^{(2)}$ terms, here $e^{\pm i \Delta_{\text{pg}} \zeta}$, respectively. In principle there is an infinite series of contributions when written in terms of the exponential expansion. However, we also see that the m_0^{-1} coefficient makes the higher-order terms irrelevant as the nonlinear strength quickly drops for increasing m_0 values. Therefore it is custom to consider only the first few orders to see if phase-matching can be achieved.

Therefore, using a QPM square grating the 3WM phase-matching conditions change to

$$\tilde{D}_{\omega_s}(\omega_{\text{RR}}) = 2q_{\text{sol}} - \Delta_{\text{pg}} + k_\Lambda, \qquad (\text{SFG-RR}, A^2) \tag{6.27}$$

$$\tilde{D}_{\omega_s}(\omega_{\text{RR}}) = \Delta_{\text{pg}} - k_\Lambda, \qquad (\text{DFG-RR}, A^* A) \tag{6.28}$$

In principle there is an m_0 term in front of the k_Λ. However, we have here used the knowledge that $\Delta_{\text{pg}} > 0$ so that the SFG case needs QPM to increase the right-hand side of (6.27), thus invoking the $+k_\Lambda$ term of the exponential QPM grating expansion, and similarly for the DFG case we choose the $-k_\Lambda$ term. Expressed in the stationary lab frame we get

$$k(\omega_{\text{RR}}) = 2k_s(\omega_{\text{RR}}) + k_\Lambda - \omega_{\text{RR}}/v_{g,\text{sol}}, \qquad (\text{SFG-RR}, A^2) \tag{6.29}$$

$$k(\omega_{\text{RR}}) = -k_\Lambda + \omega_{\text{RR}}/v_{g,\text{sol}}, \qquad (\text{DFG-RR}, A^* A) \tag{6.30}$$

At this stage, it is a matter of finding the right grating pitch Λ to achieve RR wave phase matching.

Coming back to Fig. 6.8 the QPM control now allows to move the SFG and DFG lines. Initially for a large QPM pitch the QPM wavenumber is small; this means the 3WM lines move closer to each other, but still they are phase-matched in the wrong regions. Simultaneously, because of the QPM penalty of $2/\pi$ to d_{eff} (and thus a $4/\pi^2$ penalty for the cascading nonlinearity n_2^{casc}), the overall cascading nonlinearity drops in strength. Upon decreasing the QPM pitch eventually the lines are swapped so that the DFG line is below the SPM line and the SFG line above. This means that we can achieve phase-matching in the regimes where soliton photons of the proper frequencies are present. At

the same time the cascading nonlinearity increases as the reduced QPM pitch makes the SHG process closer to phase-matching.

Not only does QPM here give access to phase-matching of the RR waves, but also to a complete parametric control over the specific RR phase-matching frequency. Such a parametrically tunable RR cannot be found in 4WM. The SPM cases simply do not offer this kind of control. While the THG case does in principle offer a similar kind of birefringent control of the TH wavenumber, i.e. the left-hand side of Eq. (6.15), if the soliton forms in a birefringent medium, the THG-RR case is very elusive and almost all relevant cases studied so far for 4WM are fibers or waveguides in nonlinear media that are not birefringent.

Using QPM to achieve velocity matching for THz wave generation has been implemented in lithium niobate [156] (see review in [157, 158]), but it has to our knowledge not been used to generate velocity matching in the same transparency window as the pump/soliton wave, i.e., in the primary VIS-IR transparency range of $0.3-5.5\ \mu$m. This would also require a very broadband pump; in the standard case an 800 nm pump is used, and if we want to generate an RR at 5 μm then the pump bandwidth should be around 150 nm, corresponding to a sub-10 fs pump pulse.

Let us finally summarize the defocusing soliton-induced RR waves

$$k(\omega_{\mathrm{RR}}) = k_{\mathrm{sol}}(\omega_{\mathrm{RR}}), \qquad (\text{SPM-RR}, |A|^2A) \tag{6.31a}$$

$$k(\omega_{\mathrm{RR}}) = -k_{\mathrm{sol}}(-\omega_{\mathrm{RR}}), \qquad (\text{cSPM-RR}, |A|^2A^*) \tag{6.31b}$$

$$k(\omega_{\mathrm{RR}}) = k_{\mathrm{sol}}(\omega_a) + k_{\mathrm{sol}}(\omega_b) + k_{\mathrm{sol}}(\omega_c), \quad \omega_a+\omega_b+\omega_c = \omega_{\mathrm{RR}}, \qquad (\text{THG-RR}, A^3) \tag{6.31c}$$

$$k(\omega_{\mathrm{RR}}) = k_{\mathrm{sol}}(\omega_a) + k_{\mathrm{sol}}(\omega_b) + k_{\Lambda}, \quad \omega_a+\omega_b = \omega_{\mathrm{RR}}, \qquad (\text{SFG-RR}, A^2) \tag{6.31d}$$

$$k(\omega_{\mathrm{RR}}) = k_{\mathrm{sol}}(\omega_a) - k_{\mathrm{sol}}(\omega_b) - k_{\Lambda}, \quad \omega_a-\omega_b = \omega_{\mathrm{RR}}, \qquad (\text{DFG-RR}, A^*A) \tag{6.31e}$$

What is worth to emphasize is the fundamental difference between the SPM RR waves and the up- and down-conversion RR waves: in the SPM cases, the soliton feeds photons into the RR wave with soliton photons of the same frequency, see also discussion in connection with Eq. (6.3). It is the quintessential definition of a self-acting nonlinearity, and explains why the SPM-RR wave needs the soliton spectrum to overlap with it before any radiation is observed. In contrast, we see that the THG-RR, SFG-RR and DFG-RR waves are converted from soliton photons that do not need to be at the RR frequency; they are indeed of up- or down-conversion origin, and in fact the soliton photons might even originate quite close to the spectral center of the soliton. Most importantly, though, is that the soliton spectrum does not have to overlap the RR frequency. Therefore these RR waves may even be observed at very isolated regions of the spectrum.

With this new theory in place, we can explain the puzzling peaks we observed in the PPLN experiments. This is explained in what follows.

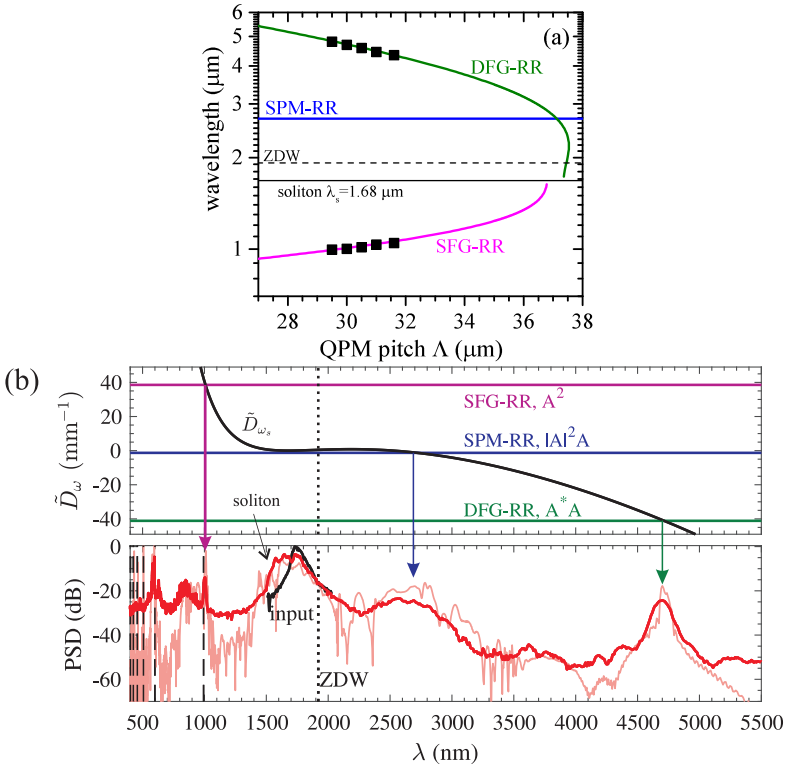

Figure 6.9: (a) Calculated tuning curves for SPM, DFG and SFG RR waves (using a fixed $\lambda_s = 1.68$ μm), plotted with data from the same experiment as (b) but where the QPM pitch was varied. (b) Full experimental spectrum recorded for $\lambda_0 = 1.75$ μm, 50 fs (80 nm FWHM) and $I_0 = 150$ GW/cm^2, launched in a 10 mm PPLN with $\Lambda = 30.0$ μm; the experimental data (thick red) are directly compared to a numerical simulation (thin light red) and calculated higher-order quasi-phase matching resonances (dashed lines). The top plot shows the theoretical RR phase-matching conditions to the soliton using $\lambda_s = 1.68$ μm and q_{sol} calculated using $T_{\text{sol}} = 10$ fs.

6.4.2 Quadratic nonlinear resonant radiation in PPLN

Figure 6.9(a) shows how the specific phase-matching curves look like in PPLN; we do not show the cSPM-RR and THG-RR waves as they were not observed neither in simulations nor in the experiment. The curves are plotted vs our control parameter, the QPM pitch. As the QPM pitch is reduced the SFG and DFG RR waves start to become phase-matched in the "physical" regimes (the phase-matching curves above and below the soliton line, respectively, are not shown) and slowly branch out from the soliton frequency. Around $\Lambda = 25$ μm the SHG process becomes phase matched ($\Delta k - k_\Lambda = 0$) for the chosen soliton wavelength, so for QPM pitch values smaller than this we have self-focusing from cascading. The phase-matching curves were calculated for the specific experiment shown in (b), where we used a $\lambda_0 = 1.75$ μm pulse in a 10 mm long PPLN with $\Lambda = 30.0$ μm. We estimate from the spectrum that the soliton slightly blue-shifts to 1.68 μm, which was the value used in the phase-matching calculations. The supercontinuum spans over 3

octaves (550-5000 nm), and required in addition to what was done for the LN mid-IR RR wave experiment to also measure the visible and near-IR range with a silicon-based CCD spectrometer; in this range we see signs of the SH and TH components, as well as higher-order QPM resonances (explained later). We should also mention that Fig. 7.3 shows an alternative plot of the recorded supercontinua that better emphasizes the high-frequency part. Coming back to Fig. 6.9, by using the phase-matching curves superposed above the spectrum, we confirm that the broad mid-IR peak above the ZDW is the Kerr SPM-RR wave, equivalent to the one we have also observed in bulk LN. Secondly, a peak is located at 1002 nm. Even if this is close to a QPM phase-matching line (dashed line), we show below evidence that this is indeed the SFG-RR wave. Finally, the peak at 4700 nm is the DFG-RR wave.

At this point it is worth remarking the excellent agreement with the numerical simulations in light red, performed using the NAEE (2.11). The PSD scaling is not arbitrary: the experimental input pulse peak defines 0 dB, and the experimental spectrum is then shifted down so the area remains constant. The simulation was then also set at 0 dB peak input PSD, and in this way the simulation can be overlapped and compared *quantitatively* with the experiment. The agreement is not coincidental, as simulations agreed well also with other recorded supercontinua at other pitch values, pump wavelengths and intensities. To achieve this kind of 1-1 agreement over nearly a decade of bandwidth, the main parameters that we varied were the Kerr nonlinearity, the Raman fraction and the effective quadratic nonlinearity. All other parameters were set as closely as possible to the experimental values. Eventually, the combination that we settled on was to use the same Kerr values as in the mid-IR RR wave simulations ($n_2^{\mathrm{SPM}} = 54 \cdot 10^{-20}$ m^2/W at 1400 nm, adjusted slightly using Miller's rule for the longer wavelengths used, and $f_R = 0.35$). Instead the d_{eff} we used was lower, 18 pm/V. This is entirely justifiable within the experimental uncertainties of various PPLN samples (it is well known that the poling process may reduce d_{eff} and that sample-to-sample variation may occur).

Figure 6.10 shows the dynamics of the RR wave formation as the input peak intensity is increased: the soliton is seen to be blue-shifted (the black dashed line shows the calculated "center-of-mass" soliton wavelength). This is in stark contrast to the massive Raman-induced red-shift observed in unpoled LN. It is a consequence of pumping close to the ZDW, which makes the soliton recoil towards the blue. Based on the appearance of the RR waves, we estimate that the soliton forms for much lower intensities (at around 50 GW/cm^2) than in unpoled LN, which is due to the larger effective nonlinearity as QPM significantly reduces the SHG phase-mismatch.

The blue-shifted soliton wavelength directly affects all three phase-matching conditions. This blue-shift explains why the SPM-RR plateau red-shifts with increasing intensity. The DFG-RR phase-matched RR wave remains more or less constant, but the SFG-RR wave noticeably changes wavelength from low to high intensity as the soliton blue shifts, see bottom plot. Even if this peak lies quite close to the $m_0 = 1$ QPM line, there is evidence that it is indeed a DW: it clearly follows the calculated SFG-RR phase-matching as the intensity increases and it is also too broadband to be a QPM line; note in contrast how narrow the $m_0 = 3$ and 5 QPM lines are. For high intensities the SPM-RR plateau flattens, and numerical simulations indicate that this is due to increased pump depletion as well as significant self-steepening during the soliton formation stage. The visible range contains spectral "copies" of the soliton supercontinuum at the harmonic

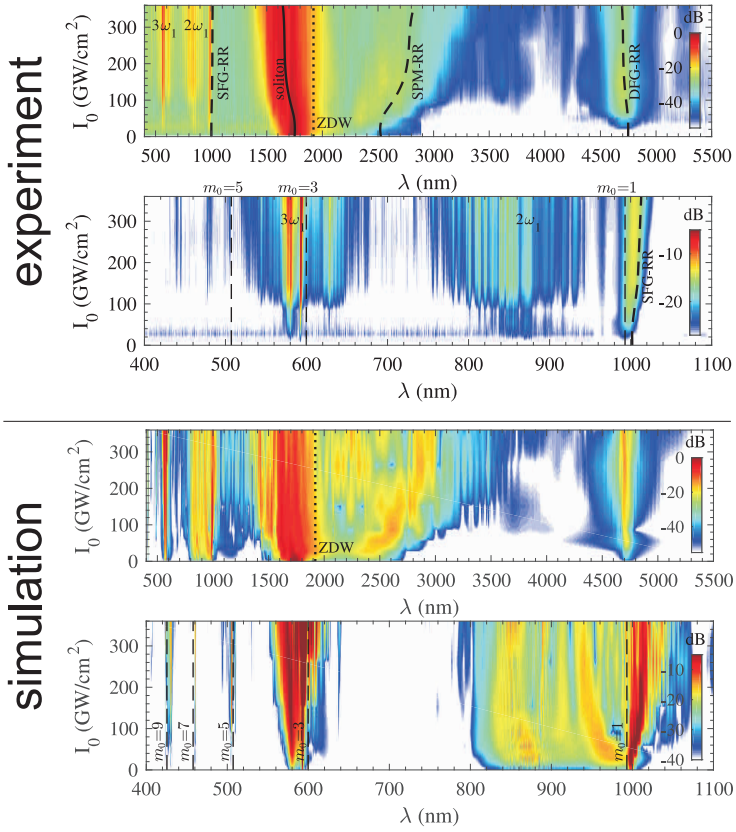

Figure 6.10: Comparing experimental data with simulations of the supercontinua for various intensities with the same parameters as Fig. 6.9. Dashed lines: theoretical phase-matching wavelengths using the extracted soliton wavelengths (black line). The second plot shows details of the visible and short-wavelength near-IR range, including calculated QPM resonances.

wavelengths ($2\omega_1$, $3\omega_1$); these are the "driven" harmonic waves by the cascaded SHG and THG nonlinearities that we investigated with the nonlocal analysis. They represent a coherent extension of the supercontinuum into the visible. The simulations indeed confirmed that the supercontinua had a high degree of coherence, also in the driven harmonic extensions.

Finally, Fig. 6.11 shows the broadband tunability of the mid-IR RR wave from the DFG process. The spectra were recorded in a 20 mm long PPLN crystal with 10 different QPM pitch values. All spectra were recorded one after another so the intensity magnitudes are therefore absolute and can be related to each other. The tuning range demonstrated here has a quite specific importance: as the inset bars indicate, the IR molecular vibration absorption bands that are present in this range are IR stretching modes, which, apart from the well-known band for CO_2 in the gas phase, include the important alkyne and nitrile stretching modes. This degree of tunability is quite unique, especially considering that only a single pump pulse was used, and it could be exploited by using an adiabatic change

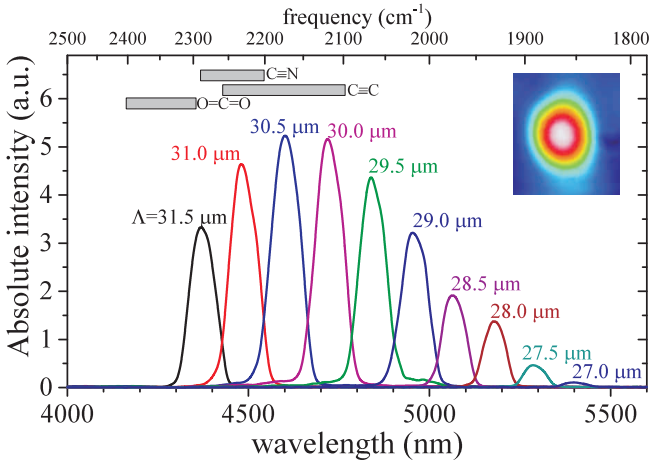

Figure 6.11: Experimental mid-IR spectra showing the DFG-RR waves, recorded with a 20 mm PPLN with 10 different QPM pitch values using $\lambda_0 = 1.75$ μm and $I_0 = 55$ GW/cm^2; note the linear y-axis. Inset: typical transverse beam profile of the long-pass filtered mid-IR RR wave.

in the pitch along the crystal to give a broader and smoother DFG-RR peak to cover the spectral gap towards the SPM-RR. Our theoretical calculations also indicate that by raising the PPLN temperature from 20 to 250 °C would shift the RR wavelengths with 5%. In the 4WM case the RR position has little or no tunability except in a gas-filled hollow-core fiber, where the pressure may control both the dispersion and the nonlinearity [148, 159, 147, 160]. However, it also requires adjusting the pump power.

6.5 Solitonic vs non-solitonic resonant radiation

One can always find radiation when there is phase matching; a soliton is not required to do that. A good example is the PPLN experiment in the previous section, where many RR waves appeared of non-solitonic origin due to QPM higher-order phase matching. In addition, as we discussed in connection with the DFG RR wave, this particular case is subject to the velocity-matching condition where the phase-velocity of generated DFG RR wave must be identical to the group velocity of the pump. This is exactly the same condition as when one launches a broadband fs pump and expect to see THz radiation become phase-matched, but there we do not excite a soliton, so clearly it works without soliton excitation as well. The main property of working with solitons is therefore not a question of whether we can achieve phase-matching at all, but rather *where* in the spectrum we can observe it and ultimately also how strong it can be.

Thus, when discussing RR waves with solitonic origin, it is important to distinguish them from the cases where the origin is non-solitonic. This issue has not been discussed much in the literature, and we stumbled upon it by chance: In our simulations and experiments we could observe RR waves in agreement with the solitonic phase-matching conditions. However, the question arose whether this radiation could simply be explained as phase-matching from sidebands of the very broad pump spectrum of the input laser

(i.e. before it becomes a soliton). This question motivated an experimental and theoretical study [10] where we compared the nonlocal theory with ordinary phase-matching. However, it is now clear that this is exactly the same as asking what is the difference in e.g. the DFG case between the standard THz emission from phase-matching the sidebands of a broadband pump and the soliton-induced RR waves.

In the following we discuss the different approaches. We use the SHG case as example, as it leans naturally towards the nonlocal theory, and the experiment was ultimately performed in type I BBO, so the FW and SH have different polarizations.

6.5.1 Phase-matched sidebands theory

We have already in Sec. 3.2 explained how the nonlocal theory works, and how it is connected to the soliton-induced RR wave phase-matching condition derived in the previous section.

Let us therefore try to calculate the phase-matching in the linear case. The traditional approach based on phase-matched sidebands works as follows: In absence of phase matching between the center frequency ω_1 and ω_2, phase-matched SHG of a pulsed beam can occur using a sideband frequency in the FW spectrum ω_1', which then generates a SH at $\omega_2' = 2\omega_1'$ that is detuned from ω_2. This explains the detuned SH peak observed. Obviously changing the amount of phase mismatch of the center frequencies changes the SH detuned frequency that can be phase-matched also changes, which explains the tunability.

In order to quantify this, it is well known that under the undepleted FW approximation (I_1 is constant in ζ) the SH intensity obeys the equation

$$I_2(L) = \frac{2\omega_1^2 d_{\text{eff}}^2}{n_1^2 n_2 c^3 \varepsilon_0} L^2 \text{sinc}^2(\Delta k L/2) I_1^2 \tag{6.32}$$

which can be derived directly from Eq. (2.1b) by integrating over ζ and neglecting SH dispersion; the "undepleted FW" assumption also implies that the FW does not depend on z, and therefore can be taken constant in this integration. We now study the chromatic variation of the phase-matching condition $\Delta k = k_2^{(0)} - 2k_1^{(0)}$, i.e. $\Delta k(\omega) = k_2(2\omega) - 2k_1(\omega)$: when $\Delta k(\omega_1) \neq 0$ we may look for a phase-matching point detuned away from the FW frequency ω_1', but where frequency conservation is obeyed $\omega_2' = 2\omega_1'$. Graphically, the sinc-function at phase matching is centered at ω_2, but in absence of phase matching it is shifted to a new frequency ω_2'. Focusing on a sideband Ω^{sb} to the SH frequency this can be written as $\Delta k(\Omega^{\text{sb}}) = k_2(\omega_2 + \Omega^{\text{sb}}) - 2k_1(\omega_1 + \Omega^{\text{sb}}/2)$, and expanding it we get $\Delta k(\Omega^{\text{sb}}) = \Delta k - d_{12}\Omega^{\text{sb}} + \frac{1}{2}\Omega^{\text{sb}2}(k_2^{(2)} - k_1^{(2)}/2) + O(\Omega^{\text{sb}3})$. When $d_{12}^2 - 2\Delta k(k_2^{(2)} - k_1^{(2)}/2) > 0$, phase-matching occurs at the frequency offsets

$$\Omega_{\pm}^{\text{sb}} = \frac{d_{12} \pm \sqrt{d_{12}^2 - 2\Delta k(k_2^{(2)} - k_1^{(2)}/2)}}{k_2^{(2)} - k_1^{(2)}/2} \tag{6.33}$$

accurate up to 2. order. We see that the condition for having phase-matched sidebands, $d_{12}^2 - 2\Delta k(k_2^{(2)} - k_1^{(2)}/2) > 0$, is reminiscent of the resonance condition we employed for the nonlocal theory, cf. Eq. (3.15). If we express it through the phase-mismatch parameter it becomes $\Delta k < \Delta k_{\text{r}}^{\text{sb}} = d_{12}^2/(2k_2^{(2)} - k_1^{(2)})$ when $k_2^{(2)} - k_1^{(2)}/2 > 0$; compare this with

the nonlocal result Eq. (3.14). Note that an analytical result for the detuned SH frequency was calculated previously [86, 19] taking into account only GVM (i.e. accurate to 1. order only).

This approach is quite phenomenological, because the undepleted FW result Eq. (6.32) is based on the monochromatic phase mismatch $\Delta k = k_2^{(0)} - 2k_1^{(0)}$. Any direct influence of the FW dispersion is absent from this equation, and can therefore not play a role in the analysis. However, it intuitively makes sense that we may "track" the phase-mismatch variation vs. frequency and therefore make the generalization to $\Delta k(\omega) = k_2(2\omega) - 2k_1(\omega)$. The nonlocal approach also highlights how easily the SH higher-order dispersion is taken into account to describe dispersion beyond the monochromatic phase-mismatch parameter, and in fact a sinc-like result can be derived in the case where SH dispersion is present (see [71]).

6.5.2 The approach of Valiulas et al.

To see this, we follow the approach in [71]. The first step is standard, and introduces an auxiliary SH amplitude $E_2(\zeta,\tau) = B_2(\zeta,\tau)e^{-i\Delta k\zeta}$ so the SH equation becomes

$$\left[i\frac{\partial}{\partial\zeta} + \Delta k - id_{12}\frac{\partial}{\partial\tau} - \tfrac{1}{2}k_2^{(2)}\frac{\partial^2}{\partial\tau^2}\right]B_2 + \frac{\omega_1 d_{\text{eff}}}{cn_2}E_1^2 = 0 \tag{6.34}$$

In Fourier domain this can be written as

$$\frac{\partial}{\partial z}B_2(\zeta,\Omega) - iD_2(\Omega)B_2(\zeta,\Omega) = i\frac{\omega_1 d_{\text{eff}}}{cn_2}\mathscr{F}[E_1^2] \tag{6.35}$$

where $D_2(\Omega) = \frac{1}{2}k_2^{(2)}\Omega^2 - d_{12}\Omega + \Delta k$ is the effective SH dispersion operator in frequency domain. To solve this we first look for solutions to the homogeneous equation $\frac{\partial}{\partial\zeta}B_2(\zeta,\Omega) - iD_2(\Omega)B_2(\zeta,\Omega) = 0$, which are on the form $B_2^{(h)} = ae^{iD_2(\Omega)z}$. Under the assumption that $\mathscr{F}[E_1^2]$ does not depend on ζ a particular solution $B_2^{(p)}$ can be found that is constant in ζ. This makes the $\partial B_2^{(p)}/\partial\zeta = 0$, and therefore we directly get from Eq. (6.35)

$$B_2^{(p)}(\Omega) = -\frac{\omega_1 d_{\text{eff}}}{cn_2 D_2(\Omega)}\mathscr{F}[E_1^2] \tag{6.36}$$

Inserting the total solution as a linear combination $B_2 = B_2^{(h)} + B_2^{(p)}$ into Eq. (6.35) and using the boundary condition $B_2(\zeta = 0,\Omega) = 0$ we get $a = -B_2^{(p)}(\Omega)$, and thus

$$B_2^{(h)}(\zeta,\Omega) = \frac{\omega_1 d_{\text{eff}}}{cn_2 D_2(\Omega)}\mathscr{F}[E_1^2]e^{iD_2(\Omega)z} \tag{6.37}$$

The total solution then becomes

$$B_2(\zeta,\Omega) = \frac{\omega_1 d_{\text{eff}}}{cn_2 D_2(\Omega)}\mathscr{F}[E_1^2]\left[e^{iD_2(\Omega)\zeta} - 1\right] \tag{6.38}$$

$$= ie^{iD_2(\Omega)\zeta/2}\frac{\omega_1 d_{\text{eff}}}{cn_2}\zeta\,\mathscr{F}[E_1^2]\text{sinc}[D_2(\Omega)\zeta/2] \tag{6.39}$$

If we now consider a transform-limited FW, $|\mathscr{F}[E_1^2]| = \mathscr{F}[|E_1|^2]$, then we get

$$I_2(\zeta,\Omega) = \frac{2\omega_1^2 d_{\text{eff}}^2}{n_1 n_2^2 c^3\varepsilon_0}\zeta^2\text{sinc}^2[D_2(\Omega)\zeta/2]I_1^2(\Omega) \tag{6.40}$$

where the usual sinc-like behavior is recovered, only here the full SH dispersion is present in the argument.

We see that the nonlocal result is recovered in this process: the particular solution (6.36) is namely exactly equivalent to the nonlocal result derived in Eq. (3.12). This is also what is denoted as the "driven" wave in [71], and it should not be surprising that the particular solution found by assuming a ζ-independent behavior is identical to the nonlocal result. Instead the homogeneous part, denoted as the "free" wave in [71], is neglected in the nonlocal approach, but it describes the well-known temporal walk-off wave that travels away from the FW after one GVM length $T_0/|d_{12}|$ and moves with the SH group velocity (and evidently also becomes affected by the SH HOD, cf. the $e^{iD_2(\Omega)\zeta}$ phase term).

Still the FW dispersion is elusive in these approaches; while this does not play a role when a soliton is excited, since it is inherently dispersion free, it will play a role in the non-solitonic regimes. We here note that the FW dispersion can indirectly affect the SH through the FW "source term", $\mathscr{F}[E_1^2]$. Even when the undepleted FW assumption holds, a phase can namely be accumulated due to dispersion. This does make the source term ζ-dependent, and in order to show the consequence a more rigorous analysis is required, see e.g. [64].

It seems clear from these considerations that the only difference between the two cases is the assumption posed on the FW. The phase-matched sidebands theory assumes that the FW follows the material dispersion. The nonlocal theory as a starting point assumes that the FW is not affected by higher-order dispersion, and only carries a phase and a group velocity. However, in both cases any effect of the FW dispersion to the theoretical result must come from releasing this assumption. In both cases this is handled by the same approximation, so at the end it is just a matter of choice whether the FW GVD will play a factor or not, and not a restriction. A well-known example of a FW that does not disperse nor change its amplitude in ζ, is the temporal soliton; it is merely described by a phase and a group velocity, and no other higher-order dispersion terms. The nonlocal theory is therefore implicitly a soliton-based approach while the traditional phase-matched sidebands theory is needed when the pump is dispersive (i.e. it is explicitly a non-solitonic approach).

6.5.3 Experimental observation of nonlocal resonances: analogy to soliton-induced resonant radiation

We decided to conduct an experiment [10] to verify (a) the presence of the nonlocal resonance frequencies in the resonant regime of cascading, (b) to show that these were different that traditional phase-matching to the SH sideband. The experiment was conducted in type I BBO ($oo \rightarrow e$) at a moderately high intensity (both 80 and 160 GW/cm^2 were used) with 60 fs pulses at 1.03 μm, and the crystal was angle-rotated around the phase-matching angle to access both the focusing and defocusing cascading ranges. As it turned out, this intensity was high enough to excite defocusing solitons in the $\Delta k > 0$ range, and as such this was in reality the first observation of the soliton-induced SFG-RR wave, and for sure the first observation of birefringent phase-matching of the RR wave, i.e. coupling between the soliton in one polarization to an RR wave in the cross-polarization.

The experimental results are summarized in Fig. 6.12, where (a) shows the qualita-

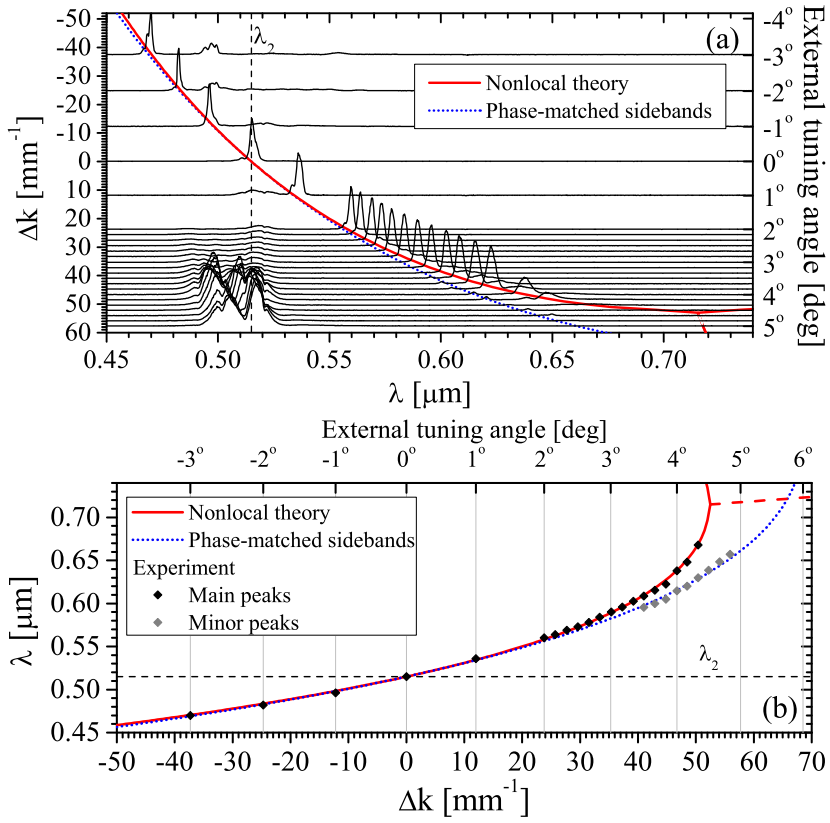

Figure 6.12: (a) Experimental evolution of the SH spectrum vs. Δk. All spectra are normalized to the same peak value and were recorded in a 25 mm long BBO crystal using $\lambda_1 = 1.03$ μm, 60 fs FWHM and $I_0 = 80$ GW/cm^2. The baseline of each spectrum indicates the invoked phase mismatch. (b) Quantitative comparison between theory and experimental data. Taken from [10].

tive evolution of the recorded SH spectrum as the angle was rotated around the phase-matching angle. We see that there is a sharp SH peak that goes from detuned towards the blue of the degenerate SH wavelength $\lambda_2 = \lambda_1/2$ for negative Δk (focusing cascading range) to a strongly red-shifted SH peak on the positive Δk side (defocusing cascading range). As the transition to the non-resonant regime is approached ($\Delta k_r^{nl} \simeq 52$ mm^{-1}) the peak becomes very broad and is now no longer dominating; around zero detuning (λ_2) some modulated peaks are instead dominating. A quantitative comparison between the experimental peaks and the nonlocal resonances is shown in (b) and we see there is a perfect agreement between them. The main deviation from the nonlocal theory and the phase-matched sideband theory occurs exactly in the defocusing range where we can excite solitons. Further evidence for this is that we in this regime observed moderate self-compression effects in autocorrelation traces of the FW, which is a typical feature of solitons. This confirms that the observed peaks are soliton-induced RR waves, medi-

ated by the SHG nonlinearity, and historically this preceded the similar observation in PPLN of the SFG-RR wave [14] and the bulk LN and BBO observations of the SPM-RR waves [11, 12]. In the defocsuing soliton range some minor blue-shifted peaks are present, which seem to obey the phase-matched sidebands theory (blue dotted curve). This is most likely conversion of the non-solitonic part of the FW. Finally, beyond the transition $\Delta k_r \simeq 52$ mm^{-1} the detuned peak disappears because the nonlocal response becomes nonresonant.

Figure 6.13(a) shows selected values of the phase-mismatch sweep, and it is compared with the nonlocal theory (b) and the phase-matched sidebands theory (c). Clearly the nonlocal theory is most accurate in explaining the trend. In Fig. 6.13 we show in (d) the results of plane-wave numerical simulations with phase-mismatch values identical to the selected spectra in (a). The FW spectra (thick lines) in (d1) show significant spectral broadening. The SH spectral trend in (d2) is very similar to the experiment in (a); in particular we verify that at $+5^\circ$ we see the same type of spectrum as in the experiment, namely that the radiation around λ_2 dominates due to the broadband nonlocal response. This is because the phase-mismatch value is in the non-resonant range where there are no phase-matched RR frequencies. Since the theory predicts that $I_2(\Omega) \propto |R(\Omega)|^2 |\mathscr{F}[E_1^2(\tau)]|^2$, and not $I_2(\Omega) \propto |R(\Omega)|^2 I_1^2(\Omega)$, we also show $|\mathscr{F}[E_1^2(\tau)]|$ in (d1) with thin lines: due to a significant FW phase it becomes much broader than $I_1(\Omega)$, and thus $I_1(\Omega)$ is not a good measure to predict $I_2(\Omega)$. (d3) and (d4) show the time traces: For negative Δk the total nonlinearity is self-focusing, and since the GVD is positive the FW broadens temporally (leading to so-called optical wave-breaking [118]). At positive Δk the total nonlinearity is self-defocusing and (d3) shows that the intensity is large enough to excite a FW soliton, leading to a moderate compression (just like what we observed in the experiment). To quantify this the total soliton order, Eq. (5.4), is shown in each case, and the sign of the total nonlinearity is included to distinguish the self-focusing case ($n_2^{\text{tot}} > 0$) from the self-defocusing case ($n_2^{\text{tot}} < 0$). As the self-defocusing soliton orders employed are all larger than unity soliton self-compression is observed for all $\Delta k > 0$ cases. A strong pulse shock front is seen for low positive Δk that gradually degrades along with the pulse compression factor for higher Δk. This is because the cascading self-steepening term is $\propto d_{12}/\Delta k$ and because the effective soliton order decreases, respectively. In (d4) the SH temporal intensities are shown. The dashed line indicates the calculated walk-off delay due to GVM; this is the "free" wave. The "driven" wave appears in the vicinity of the $\tau = 0$ regime; it is essentially a temporal copy of the FW (particularly evident for large Δk). The strong SH components observed in between the driven and free waves for positive Δk are the nonlocal RR waves.

We end by remarking the extreme tunability of the resonant SH peak: we can practically tune it across the entire visible range. This technique is actually quite commonly used, where SHG in thick crystals is employed to generate a spectrally compressed peak that is wavelength-tunable through Δk [86, 19, 87, 88, 89, 65, 67, 70]. It is also important to note that the resonance bandwidth is inversely proportional to the crystal length, cf. Eq. (6.32). The main difference between what we observe is that in the historical experiments the intensity is not high enough to excite the soliton. Conversely the intensities we use make it possible to transfer large energies into the SH peak.

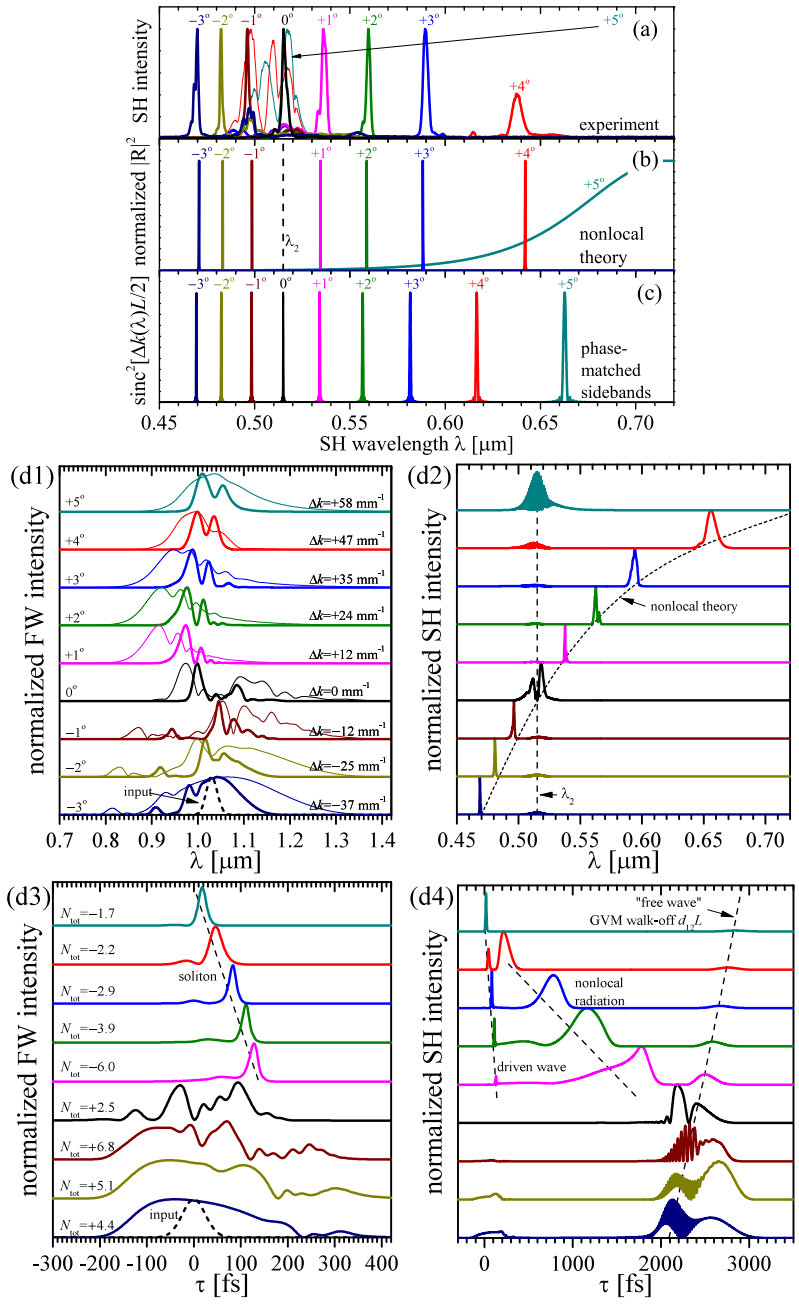

Figure 6.13: (a) Selected SH normalized experimental spectra from Fig. 6.12. (b) The nonlocal theory, predicting $I_2 \propto |R(\Omega)|^2$. (c) Phase-matched sidebands theory, predicting $I_2 \propto \mathrm{sinc}^2[\Delta k(\lambda)L/2]$. (d) Numerical simulations of the SEWA equations with the same crystal angles and experimental parameters as (a). (d1+d2) Normalized spectra; in (d1) $|\mathscr{F}[E_1^2(\tau)]|$ is also shown (thin lines). (d3+d4) Normalized temporal intensities (note the different time axis scalings). An offset is imposed between each curve for clarity of presentation. Adapted from [10].

Chapter 7

Supercontinuum generation with defocusing solitons

But I am up riding high amongst the waves
Where I can feel like I
Have a soul that has been saved
Where I can feel like I've
Put away my early grave

Pearl Jam "Amongst the Waves"

Supercontinuum generation (SCG) was one of the early observations of extreme nonlinear effects made in bulk media [161], but due to a transverse instability by a combination of diffraction and self-focusing effects, above a critical power [162] the beam breaks up into unstable hot spots eventually leading to filamentation [163]. Filamentation is often undesirable as it can lead to a spatially incoherent beam. However, under controlled circumstances a so-called white-light continuum (WLC) can be generated [164], where "white" in the name historically comes from the bandwidth being so broad that it appears "white", i.e. containing all colors. In a WLC typically a single filament is created ensuring a good spatial coherence [165].

SCG with soliton formation is perhaps the technique that allows for the largest bandwidths, typically spanning well over an octave, as well as much more flat spectra than a WLC; it also exploits SPM-induced broadening, but temporal ultrashort solitons are formed due to the interplay with material dispersion. The interaction between the solitons will massively extend the spectral bandwidth. Essentially the time trace of a soliton-induced SCG can be a very complex train of ultrashort solitons and other waves, but strikingly the process can be extremely coherent, even from shot to shot. The problem in bulk is that formation of temporal solitons is accompanied by filamentation due to self-focusing, and therefore soliton-induced SCG almost exclusively occurs in a waveguide or fiber [136], where 2-3 orders of magnitude lower pulse energies are used.

There are currently two challenges that overall dominate the supercontinuum community, one is going towards the UV range (and beyond) and another is going towards the mid-IR range. Both take their starting point in the near-IR range, exploiting the massive amount of technology in efficient, stable high-power pulsed lasers that have been developed over the past decades. We have in the past decade decided to focus on the mid-IR

range for cascading since transparent nonlinear crystals are abundant in this range (unlike the UV, which is a significant challenge) and because the defocusing supercontinuum extends itself naturally towards the mid-IR by excitation of RR waves. Unless otherwise stated we will in this chapter not address waveguide and fiber aspects of SCG, and instead focus on the high-energy aspect of SCG, occurring in bulk media or gases.

The mid-IR range, spanning from 2.0-8.0 μm (short range) and 8.0-20 μm (long range), holds a tremendous scientific and technological potential, which has yet to truly unfold due to a general lack of efficient mid-IR pulsed lasers. There are many reasons for the large interest in the mid-IR range. Firstly it contains the vibrational stretching modes of the important C-H, O-H and N-H bonds that lie in the 2.5-3.5 μm wavelength range, and the carbon doublet and triplets in the 4-7 μm range. From 7-20 μm lies the so-called "fingerprint region" where all organic compounds have a unique spectral absorption pattern due to single-bond bending modes. In order to excite and control these modes, bright, ultrashort and ultrabroadband coherent mid-IR radiation is needed. If instead near-IR laser pulses are used, overtones of the vibrations are excited, reducing the desired control. Secondly, the mid-IR range is of interest for meteorology and defense applications because of an increased atmospheric transmission (e.g. from 3-5 μm) and because the 2-3 μm wavelength range is considered "eye-safe", i.e. minimal eye damage will incur under exposure.

Both the SPM-induced broadening and the WLC techniques are widely used in the near-IR but until recently little has been done in the mid-IR: Broadband continua were found when pumping with mid-IR pulses through SPM alone (i.e. before filamentation set in)[166, 116, 167], which is limited in energy by onset of small-scale filamentation, or by generating a WLC by an increased peak power [168, 169, 170, 171, 172, 173]. Alternatively one may start with a femtosecond near-IR source and mix the frequency-converted harmonics in air and use four-wave mixing to achieve broadband mid-IR radiation [174, 175, 176], but with a very low yield. With similar techniques near-IR laser pulses can be converted to few-cycle or even single-cycle duration to practically any desired (longer) wavelengths, but again the yield is very low.

7.1 Filament-free supercontinuum generation in crystals

The potential of a using a defocusing nonlinearity to have filament-free nonlinear interaction for SCG is naturally promising, given the pulse energy limitations of filamentation that we have outlined above. This remains a main motivation, just like it has been for using the soliton effect to compress pulses with large pulse energies. In a supercontinuum context there are several other aspects that are attractive about a defocusing nonlinearity in crystals

- The soliton can be excited using near-IR lasers; soliton-based filamentation is in turn requiring large amounts of anomalous dispersion, meaning it has to be pumped with longer wavelengths [177, 168, 170, 122, 171, 172, 79] and it requires very short pump pulses [80].

- The supercontinuum naturally extends towards longer wavelengths because RR waves are directly phase-matched there, unlike filamentation which tends naturally

to go towards the blue. Therefore it is more pertinent to the task of using near-IR laser technology to enter the mid-IR range.

- Crystals are compact, may have high damage thresholds, and can have large aperture, supporting large energies.

Supercontinuum generation has been observed in bulk quadratic nonlinear crystals [31, 35, 36, 178, 38, 39, 40]. Around phase-matching the pump spectral broadening is accompanied by second-harmonic generation, which adds to the spectral bandwidth. However, even when tuning away from SHG phase matching ($\Delta k \neq 0$) the spectral broadening was observed to become surprisingly large [35, 36, 178]. Historically the extended broadening away from phase matching was explained as the SPM initiated continuum around the pump mixing through sum-frequency generation (SFG) with the pump. However, we now know that the cascaded, phase-mismatched SHG process generates an SPM-like nonlinearity, which adds to the focusing material Kerr SPM nonlinearity. When $\Delta k > 0$ the total nonlinearity may become defocusing, while for $\Delta k < 0$ the cascaded effect is also self-focusing, so the supercontinuum can be assisted by controlled filamentation [38, 39, 40].

Thus, while cascading has been known for decades, it is only recently that it has been used for supercontinuum generation, and the role of cascading has in some sense been overlooked until our contributions.

7.1.1 Supercontinuum generation in BBO

The goal of our BBO experiments have not directly been to observe SCG, but the last experiment pursuing the RR waves did manage to record very broadband spectra under various pump conditions [12]. The results are summarized in Fig. 7.1, where we use three different pump wavelengths in the normal dispersion regime for soliton excitation. Up to 0.1 mJ pulse energies were used.

The 1.24 μm case has only a weak coupling into the RR wave; this is because the cascading blue shifts the soliton so the phase-matching condition is over an octave away. The supercontinuum therefore has a quite large dip, and only a few % of the total energy resides beyond the ZDW. In the 1.3 μm case the energy beyond the ZDW is almost 10%, since the soliton center wavelength is close to the ZDW. Finally, the 1.4 μm is peculiar, since it as was explained in Fig. 6.3 it consists of a leaked part of the SPM broadened pump above th ZDW and a solitonic part below the ZDW. Despite a reduced bandwidth compared to the other cases, these supercontinua still span over an octave, and the spectral variation is roughly 10 dB with almost half the energy beyond the ZDW.

The phase-mismatch value for each pump wavelength was chosen to give the most energy into the RR wave; as we can see we can make it smaller as the ZDW is approached since the GVM drops so reducing Δk does not give increased self-steepening (which scales as $d_{12}/\Delta k$). Another consequence of the low GVM is that the transition to the resonant regime is very close to phase-matching in this wavelength range, cf. Fig. 5.1(a).

We finally remark that there is also a continuum in the *e* polarization in the SH component in the visible, cf., e.g., the simulations shown in Figs. 5.6 and 6.3. We did not record it for this specific experiment, but from the simulation results we estimate that around 5% of the pump energy resides in the *e* polarization.

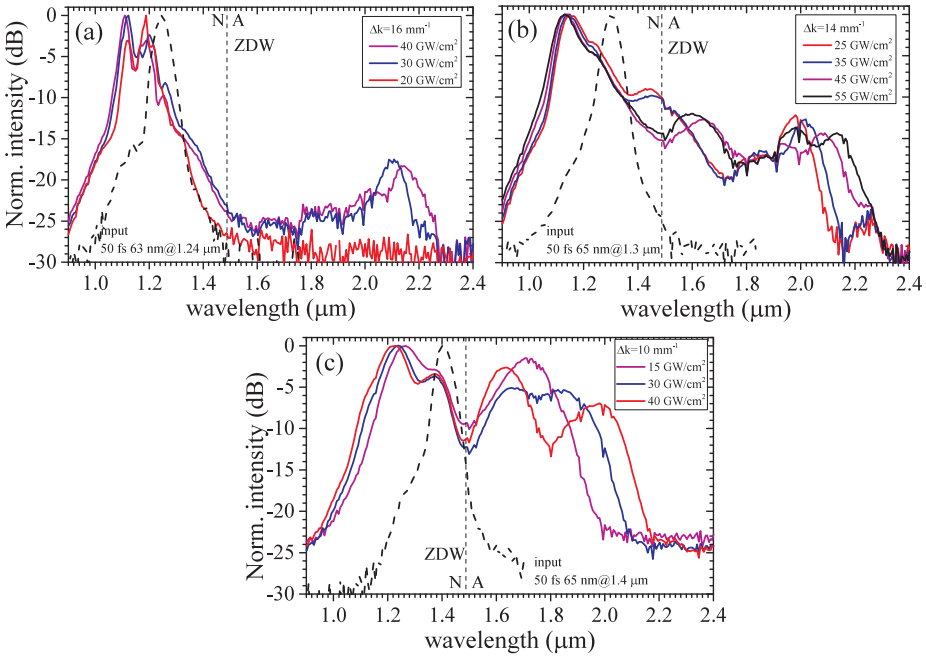

Figure 7.1: Experimentally recorded supercontinua in 25 mm BBO for pump wavelengths of (a) $\lambda = 1.24$ μm, (b) 1.30 μm, (c) 1.40 μm and for various pump intensities. The details of the experimental setup is explained in Sec. 5.3. Adapted from [12].

7.1.2 Supercontinuum generation in LN

LN was the first crystal we used actively for SCG. While investigating soliton formation, we realized that in LN after just 1 mm of propagation we could excite the soliton. This gave us the opportunity to go very far beyond the soliton self-compression point, just like in a fiber, and observe a full supercontinuum [7].

Initially we recorded only SCG in the near-IR, cf. Fig. 6.5 [7], but later we got access to the mid-IR and could characterize also the long-wavelength part of the spectrum, cf. Fig. 6.6 [11]. In Fig. 7.2 we show the SCG evolution during a sweep of the input intensity. Significant broadening starts to occur between 50 and 90 GW/cm^2, after which the new spectral shoulder clearly redshifts with increased intensity. This indicates that the Raman effect is indeed affecting the dynamics before soliton formation (no MIR DW radiation, the tell-tale sign of a soliton, was observed for these cases). At higher intensities the supercontinuum develops into the mid-IR. As we noted in Sec. 6.3 there are two DW peaks, since besides the main one just below 2.9 μm there is also a minor peak between $3.5 - 4.0$ μm. The presence of this minor peak was in the simulations in the previous chapter explained as an early-stage RR wave when the soliton first forms. The early formation is unfortunately below the noise floor of our mid-IR measurement, but otherwise the experiment and the simulations corroborate each other on this point.

This experiment shows how one directly can get an over 1.5 octave spanning super-

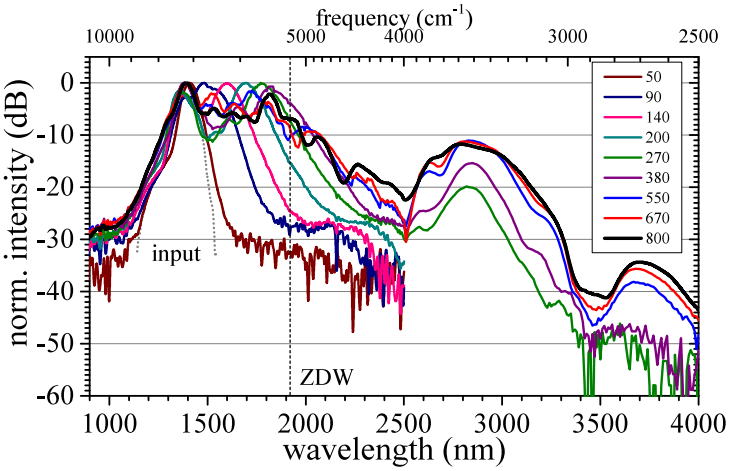

Figure 7.2: Variation of the supercontinuum content in 10 mm LN at $\lambda_1 = 1.4$ μm while sweeping the input peak intensity (indicated in GW/cm^2). The black curve corresponds to the case in Fig. 6.6(b). Adapted from [7].

continuum with 100's of μJ of energy (basically limited by the OPA), and with over 10 μJ in the mid-IR. All that in a small piece of bulk LN, pumped with a near-IR laser.

We eventually discovered that the QPM control offered by a PPLN crystal was not just a way of getting more cascading nonlinearity, its celebrated tunability gave access to controlling the supercontinuum content. Historically, we had hesitations about using QPM because we knew that in order to get more cascading nonlinearity than unpoled LN, in wide wavelength ranges the cascading became resonant; this was the message from the nonlocal theory and it was put forward as a direct warning in [7]. Ironically, it was actually the resonant nonlocal response that ultimately gave access to (a) observation of the novel 3WM RR waves, (b) RR waves with direct tunable control over the spectral position.

The resulting supercontinuum from PPLN can be incredibly rich and broadband. We have already discussed this in detail in connection with the observation of the 3WM RR waves in Chapter 6. In Fig. 7.3 we show the spectra from the same experiment that was used to show the SFG and DFG RR waves. The intensity is swept from low to the maximum available value in the experiment, and remarkably already at around 50 GW/cm^2 does the mid-IR RR waves from SPM and DFG show up. In the same figure we also show the spectra plotted vs frequency (for convenience normalized to the input frequency). The mid-IR spectral features are astonishingly weak in this representation (in part also because the PSD is now normalized towards frequency), and in turn the harmonics become much clearer. We see that the SHG-RR wave is gradually removing itself from the QPM phase-matching line [gray line, $m_0 = 1$ cf. Eq. (6.26)] as the intensity grows. We also appreciate the SH and TH "free" waves. Note that most of the SH "energy" is in the SHG RR wave, since we are in the nonlocal resonant regime. This is typical, and was also observed in the BBO experiment in Sec. 6.5.3. Instead, the TH clearly has phase-matching to a resonance close to the degenerate frequency.

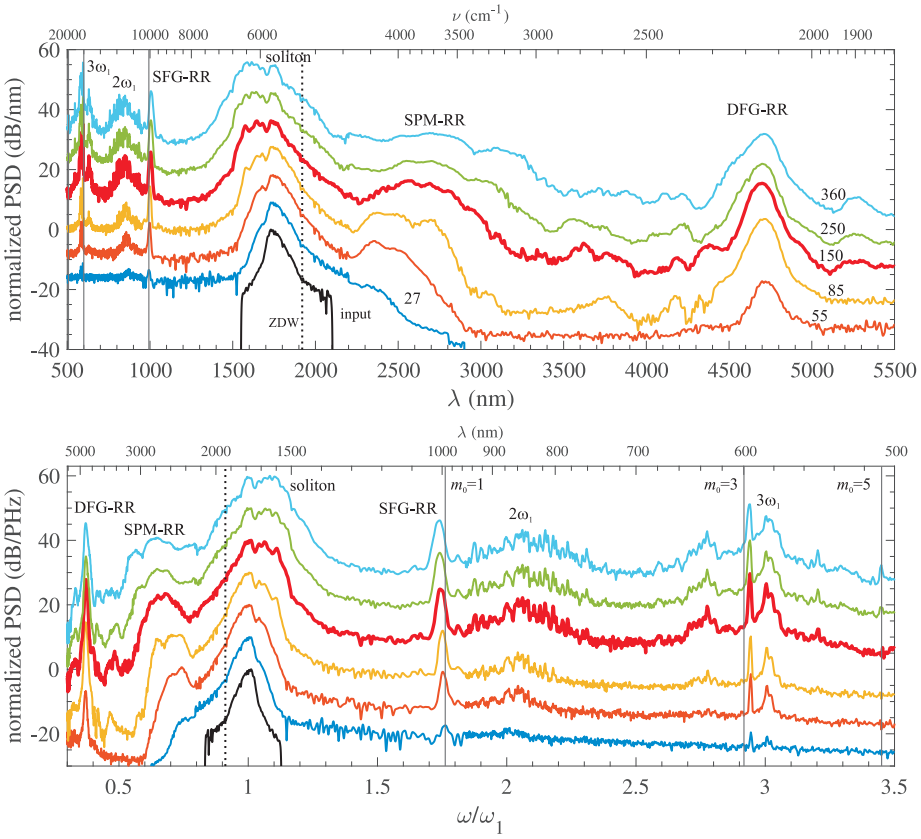

Figure 7.3: Variation of the supercontinuum while sweeping the input peak intensity in a PPLN crystal. The spectra are shown both in wavelength and frequency domain (a 10 dB offset is imposed for convenience of presentation). The numbers next to the curves in the wavelength spectrum shows the peak intensity [GW/cm^2]. The experiment was the same as in Fig. 6.9(b).

7.1.3 Supercontinuum generation in LIS

Lithium thioindate ($LiInS_2$, LIS) was singled out in our mid-IR type 0 crystal sweep in Sec. 4.4. It has a ZDW around 3.53 μm and an FOM $\simeq 2$. Furthermore it is commercially available in quite big samples. Our simulations in [9] showed soliton formation and RR waves in the mid-IR, eventually giving octave-spanning SCG in the mid-IR.

In [13] we conducted an experiment to confirm this prediction. We used a commercially available LIS crystal (Moltech), 15 mm long and 6×6 mm^2 aperture. LIS belongs to the biaxial *mm*2 point group and our sample was cut with $\theta = 90^\circ$ and $\phi = 0$; most likely it was the first time Moltech had cut an LIS crystal like this. This cut gives a maximum quadratic nonlinearity $d_{\text{eff}} = d_{33}$ where $d_{33} = 16$ pm/V@2.3 μm [179], and makes the SHG noncritical so both pump and SH have the same polarization (both are "slow" waves, with linear refractive index given by n_Z, see more details in [9]).

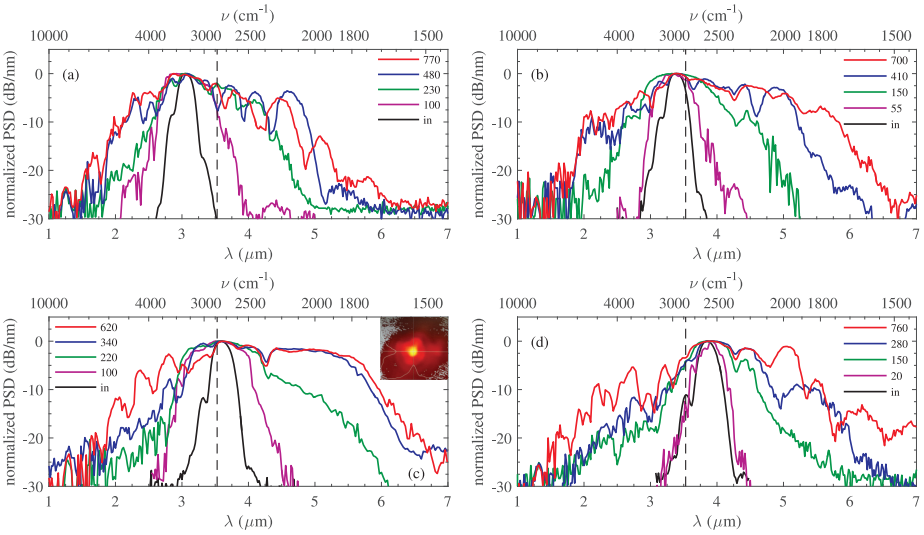

Figure 7.4: Experimentally recorded supercontinua in 15 mm LIS for pump wavelengths of (a) $\lambda = 3.05$ μm, (b) 3.39 μm, (c) 3.60 μm and (d) 3.86 μm, and for various pump intensities (indicated in GW/cm^2). The inset in (c) shows a measurement of the transverse profile measured with an IR sensitive camera for an experiment with similar conditions as the one in (c) [180]. The power spectral density (PSD) normalized to its peak value is shown. The vertical dashed line denotes the ZDW. The top axis shows the frequency in inverse wavenumbers $\nu = 1/\lambda$, as often used in spectroscopy. Note the absorption dip at the CO_2 line ($\nu \simeq 2,400$ cm^{-1}).

The SHG process is highly phase-mismatched ($l_{\text{coh}} = \pi/\Delta k \simeq 60$ μm), but notably not as much as in LN (where the coherence length can be an order of magnitude shorter); dispersion-wise LIS is instead more similar to BBO, which explains why we need 10-15 mm crystals to see significant nonlinear effects. Due to the high quadratic nonlinearity the cascading Kerr nonlinear index is large ($n_2^{\text{casc}} \simeq -60 \cdot 10^{-20}$ m^2/W in the pump range of interest). The material Kerr nonlinearity for LIS is not known. However, from its rather high bandgap along the Z direction ($E_g = 3.55$ eV [179]) the two-band model estimates the Kerr nonlinearity to be around $+30 \cdot 10^{-20}$ m^2/W. We therefore expect the overall cubic nonlinearity to be self-defocusing. That being said, our simulations in connection with the experiment showed a somewhat higher Kerr nonlinearity, $n_2^{\text{SPM}} = 50 \cdot 10^{-20}$ m^2/W and a Raman fraction $f_R = 0.2$; this implies that the electronic Kerr nonlinearity is $40 \cdot 10^{-20}$ m^2/W.

The experiment used our most advanced laser and detecting technology at the time, namely a commercial 6 mJ 1 kHz TiSa-amplifier, followed by a high-energy optical parametric amplifier (OPA) that pumps a non-collinear difference-frequency generation stage. Pulses in the $3-4$ μm range were used with up to 50 μJ energy, 85 fs FWHM duration, around 200-250 nm bandwidth and were close to transform limit. The input beam was loosely focused (0.27 mm FWHM) to reach up to 800 GW/cm^2 intensities. The specific wavelength range is actually of very significant interest as current optical parametric chirped pulse amplifiers are being developed for this range, and are even commercially

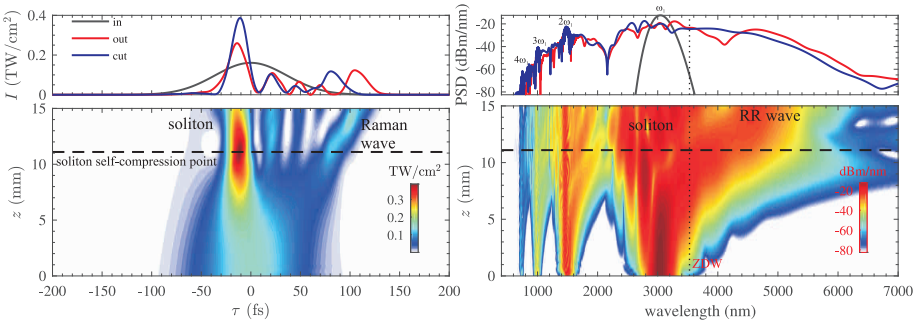

Figure 7.5: Numerical simulation at $\lambda = 3.05$ μm with 200 GW/cm^2 peak input intensity, 85 fs FWHM and 200 nm bandwidth. The "cut" shows the state for maximum peak power in time domain, i.e. where the soliton self-compresses after 11 mm propagation. The simulation used the NAEE model, and the harmonics below 2000 nm have been filtered away to avoid interference fringes in the time plot.

available now (Fastlite black Starzz, 150 μJ sub-50 fs pulses in this range).

The results are shown in Fig. 7.4, and we focus first on the cases (a) and (b) where we pump below the ZDW and therefore expect soliton formation. In (a) we see direct evidence of RR waves in the anomalous dispersion regime, while in (b) it seems to disappear with the maximum intensity. There is also some broadening towards the blue. In both cases the octave spanning bandwidth is reached around 150 GW/cm^2. For the two cases that used pumping close to the ZDW, the supercontinuum is very flat across the central range; this indicates that non-solitonic spectral broadening occurs (optical wave breaking [118]).

Broad and modulated supercontinua were observed both in (a) and (d) when pumping somewhat detuned from the ZDW (to the blue and red, respectively). This is surprising as we would have expected such a supercontinuum only in the soliton case (a). Part of the explanation lies in the the large bandwidth of the pump: we remind that the transform-limited pulse duration was between 70-80 fs, sub-8 cycles in this wavelength range. This combination means that no matter whether we pump above or below the ZDW the early-stage spectral broadening leaks into the normal dispersion regime.

In Fig. 7.5 we show a numerical simulation of the soliton case of Fig. 7.4(a). Soliton self compression occurs after 11 mm, which is accompanied by an RR wave centered around 5.0 μm. Pulse splitting is also observed similar to what was observed in the LN soliton case, cf. Figs. 5.9 and 5.10; this trailing pulse is caused by the competing delayed Raman effect, and is denoted "Raman wave". In the spectrum the Raman wave is not easy to identify, but they are as mentioned in Chapter 5 part of the blue extension of the continuum around the pump wavelength. We have also indicated the harmonics in the spectrum, and the center of each harmonic is composed of the "free" waves having spectral interference fringes because they beat with the "driven" waves at each harmonic, which are locked to the continuum around the pump wavelength.

The supercontinuum in (c), pumped slightly above the ZDW, seems the most interesting as it is extremely flat and broadband even under moderate intensities. Fig. 7.6 shows

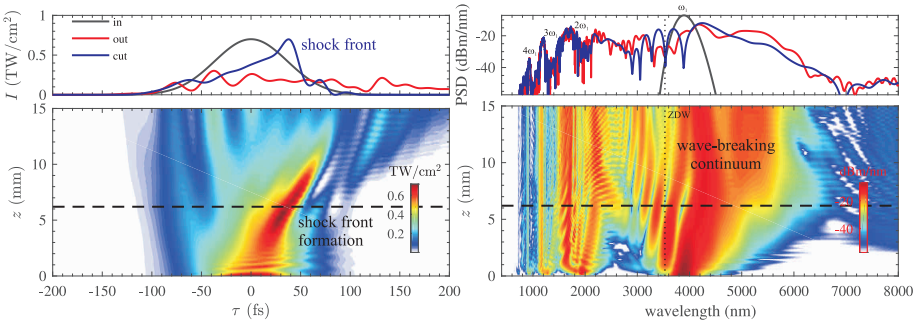

Figure 7.6: Numerical simulation at $\lambda = 3.9$ μm with 700 GW/cm^2 peak input intensity, 85 fs FWHM and 260 nm bandwidth. The "cut" shows the state where shock-front formation is occurring. The simulation used the NAEE model, and the harmonics below 2900 nm have been filtered away to avoid interference fringes in the time plot.

a simulation pumped a bit further above the ZDW, and where clearly the SCG is dominated by wave-breaking: a shock front is formed after 4-6 mm after which the pulse is being stretched in time and the chirp becomes very linear. This is typical when the sign of the nonlinearity and the GVD are the same. Due to the broadband pump the early-stage SPM towards the blue causes leakage into the normal dispersion regime, which gives the leading-edge peak.

We are currently attempting together with collaborators to SCG from LIS as a broadband pump, i.e. exciting several vibrational modes at different frequencies [180]. This may comprise of a paradigm change since usually the supercontinuum is only carrying enough spectral power at the selected frequencies to be a probe of some dynamical process. Our collaborators are currently investigating cascading crystals as well as other bulk media [173] for this purpose.

Chapter 8

Conclusion and outlook

We are the reckless
We are the wild youth
Chasing visions of our futures

Daughter “Youth”

This thesis summarizes our contributions over the past decade to the specific field of cascaded nonlinearities and its potential for advancing science and applications in ultrafast nonlinear optics.

The original motivation was to provide analytical and numerical insight into high-energy pulse compression using cascaded SHG in nonlinear crystals. Here nonlinear spectral broadening and temporal soliton formation was used to compress mJ-class femtosecond pulses towards few-cycle duration. The analytical approach came in part from nonlinear fiber optics, where the temporal soliton dynamics is very well understood and as it turns out this analogy works extremely well [2] despite most cascading applications do not rely on any type of waveguiding; the reason is that the defocusing nonlinearity makes diffraction negligible as long as the spot size is not too small, and the system can therefore be considered a quasi-plane wave system. Another key method for analyzing the cascaded system came from spatial solitons, and it led to the so-called nonlocal theory [1]. The premise is simple enough: the cascaded nonlinearity relies on cyclic up- and down-conversion of the SH, and therefore if the group velocities of the FW and SH are mismatched, the nonlinear phase shift will start building up non-locally, i.e. away from the maximum intensity in the pulse center and in the direction of the GVM drift. It turns out that the nonlocal theory is absolutely instrumental in understanding and predicting how the soliton behaves, and it can even be used to explain how the soliton couples to resonant radiation in both the SHG direction and the DFG direction. It also connects to how the cascading is contributing to self-steepening, which is known to depend on the ratio between GVM and the phase mismatch, and this is reflected in the slope of the nonlocal response function. These insights allowed us to define a so-called *compression window* where soliton formation is optimized, and we could even inside the window *a priori* roughly determine where the best phase-mismatch value would be for getting the best results [3].

Having built up knowledge about the cascaded SHG case, it was time to look for applications and set up the first experiments. An important aspect was that we had found

a number of key indicators that could aid us in screening cases (e.g. center wavelength, pulse duration, peak power etc.) without necessarily having to do simulations. At the time Yb-doped fiber amplifiers were emerging with 300+ fs pulse durations and 10s of μJ of energy centered at 1030-1064 nm. Our analyses revealed that common crystals like BBO and LN in the birefringent (type I) SHG configuration were not suitable to carry out the pulse compression due to the long pulses and rather low pulse energies [4]. Today these amplifiers can deliver pulses close to 200 fs using fiber or thin-disk laser technology. The 200 fs duration does make BBO a possible candidate for soliton compression, cf. simulations in [2, 3], although quite long (3-4 cm) crystals need to be used, which makes spatial walk-off an issue. Ultimately this sets a lower limit to the pulse peak power to perform the compression, which means that only Yb-based solid state laser amplifiers can be used and in turn it excludes some of the emerging fiber and thin-disk lasers [132]. Recently a compressor was shown that allowed pulse compression from 200 fs from a thin-disk oscillator to 30 fs. Due to the long initial pulse it was based on a sequence of 3 BBO crystals in the cascading configuration [30]. This study did not exploit solitons, but only the defocusing nonlinearity for spectral broadening followed by dispersion compensation externally to the nonlinear medium (a so-called external compressor, or two-step compressor). We should also mention that recent rapid progress in hollow-core fiber technology has opened a similar avenue [181], where 20-30 fs compression is possible in a single fiber in an external compression setup with up to 100 μJ energy. Instead, BBO would be a great option for compressing 50 fs pulses to few-cycle duration, so this might be an option as an additional stage of compression (i.e. 200 fs to 30-50 fs using a BBO sequence, then soliton compression to 10-15 fs in a single BBO, 5-10 mm long so spatial walk-off will not be an issue).

Having realized the challenges of soliton compression in type I crystals like BBO, we had the idea to try type 0 cascading in LN. Since the crystal is cheap and high quality, it was an easy test to do, and the alluring promises were the usual ones when considering type 0 interaction, especially LN, namely a very large quadratic nonlinear tensor component d_{33} and the fact that the type 0 does not have any spatial walk off, which as we noted above often is a serious obstacle for type I cascading in crystals like BBO. Although we made early attempts of observing defocusing solitons at 800 nm, it was unsuccessful. It turns out that the Kerr focusing nonlinearity was well underestimated in the literature. In this process we also discovered that LN is very Raman active, unlike BBO, and used significant efforts to develop the numerical codes and material knowledge about LN, see e.g. [6, 90, 7, 99], BBO [8], and other crystals [9]. The issue is that the net total defocusing nonlinearity relies on outbalancing the instantaneous intrinsic material focusing nonlinearity. This task is incredibly sensitive to delayed Raman contributions and overall material nonlinearity (instantaneous plus delayed). Another issue is the seemingly widespread lack of consensus in the literature about the anisotropy of the cubic nonlinear tensor component, governing the nonlinear refractive index [8]. All these developments, discoveries and literature research had to be made (often the hard way) before arriving at the bigger picture.

The early outcome of this massive effort behind understanding fundamental properties of LN, especially when pumped in the sub-100 fs range, was that we had to pump a longer wavelengths (above 1.2 μm). We were then finally able to observe a multitude of nonlinear phenomena, like the self-defocusing soliton [7], its self-compression to sub-20

fs even with 100s of μJ of energy without filamentation [7], the formation of a filament-free supercontinuum [7, 11] extending well into the mid-IR, the simultaneous emission of resonant radiation (RR) phase-matched to the near-IR soliton well into the mid-IR [11]. Finally using periodically poled LN (PPLN) the QPM control over the SHG phase-mismatch allowed us to observe emission of novel soliton-induced RR waves stemming from three-wave mixing (sum- and difference frequency generation) effects [14].

Apart from this very recent PPLN experiment, it is important to note that our research into type 0 cascading in LN was all done in bulk QPM-free crystals. There are many technical advantages to QPM-free type 0 cascading that might seem logical but were not clear or appreciated at the time we proposed it. First of all, the technology behind the crystal is really simple (basically just grow and cut it), it is easy to get hold of in good quality and cheap even in large samples. Secondly, for high-energy applications the limited aperture of PPLN remains an obstacle (although serious efforts are currently made to minimize this penalty [182]). Thirdly, using QPM to deliberate achieve non-phase matched interaction because the goal is a cascading effect leaves a huge number of higher-order QPM processes prone to become close to phase matched. This results in a large number of lines across the spectral range that tend to deplete the pump energy. This happens especially when invoking extremely broadband pulses in connection with wave-breaking or soliton formation. Fourth, QPM will significantly increase self steepening. This is because type 0 interaction is very inter-harmonic dispersive, resulting in a large group-velocity mismatch, and this GVM is known to give large self-steepening contributions [61, 63, 1], which QPM is only aggravating by lowering the phase mismatch [7, 85]. All these issues motivates the idea behind buying a cheap, few-mm long large aperture bulk LN, put it into the near-IR femtosecond beam path and observe soliton formation and supercontinuum generation with even mJ level pulse energies.

Finally, from a technological QPM is almost exclusively restricted to ferro-electric crystals like LN and KTP. Therefore by widening the search for good type 0 crystals to all those where QPM is not possible, we opened a new door towards ultrafast nonlinear optics. This in particular in the important mid-IR range, where there are many type 0 crystals like LN that are transparent, and that had not been investigated for cascading yet (i.e. phase-mismatched SHG). Our grand cascading roadmap [9] was recently successfully tested where the first of many new type 0 candidates was tested for octave-spanning supercontinuum generation in the mid-IR with up to 50 μJ of energy, basically only limited by the parametric conversion from the near-IR to the pump wavelength in the $3-4$ μm mid-IR range [13].

A similar experimental study was conducted recently by Ashihara et al.[116], where GaAs was pumped in the mid-IR just below its ZDW to give significant spectral broadening (well over 2000 nm of bandwidth) at 5.0 μm. GaAs has a very large quadratic nonlinearity, and is as such a good cascading candidate, but we calculate its FOM to be less than unity, i.e. self-focusing is dominating, and this was also noted by the authors. Therefore the spectral broadening came purely from self-focusing SPM due to the high material n_2^{SPM} of GaAs. Finally, we mention that in quadratic nonlinear crystals it is also possible to perform adiabatic near-IR to mid-IR frequency conversion and achieve octave-spanning bandwidths [183].

The discovery of the vast potential for cascading in type 0 crystals naturally directed our attention towards the mid-IR range. At the same time the mid-IR range became in-

creasingly attractive in the laser and nonlinear optics community, and solutions were requested where the efficient and technologically mature near-IR laser technology could be used to down-convert femtosecond pulses into the mid-IR. In parallel with starting up the first type 0 investigations we pointed out the vast and until then overlooked potential in exciting defocusing solitons with near-IR lasers: these solitons will naturally become phase-matched to RR waves located at longer (instead of shorter) wavelengths simply due to the fact that the defocusing solitons reside in the normal dispersion range, below the zero-dispersion wavelength [5]. This means that near-IR lasers can excite solitons directly in a bulk medium without any waveguiding, using sub-mJ or even mJ energies, and phase-match directly into RR waves located in the anomalous dispersion range in the mid-IR [6]. This was later verified experimentally [11, 12] with recorded efficiencies as high as 6%, remarkable for a single-pump scheme and considering the 1 octave span between the soliton and the RR wave. It was also shown in a novel mid-IR type 0 crystal, where pumping in the important emerging laser amplifier range $3-4\ \mu$m we could phase-match to an RR wave located in the $5-7\ \mu$m range [13]. We stress that the supercontinua from defocusing nonlinearities are remarkably energetic, orders of magnitude above those of filaments [175, 168, 176, 173].

The efficient excitation of soliton-induced RR waves is one of the key ingredients behind fiber-based supercontinuum sources. However, obtaining tunable control over their spectral location has only been observed in gas-based hollow-core fibers [148]. We discovered that in the crystals the usual SPM-based RR wave, which is hardly tunable at all (and therein lies the challenge), is accompanied by new RR waves that can be widely tunable [14]. This is because they are parametrically controlled by the phase-mismatch parameter, simply because they originate from three-wave mixing, as opposed to the four-wave mixing nonlinearity behind SPM. It turns out that this kind of RR wave, excited by the defocusing soliton, is directly connected to the nonlocal theory we derived [1]. Through the nonlocal theory we found that the delayed nonlocal response function can lead to resonant transfer into the SH when the GVM is strong and the phase-mismatch low, and this can be used to seamlessly tune the SH resonance peak across an octave around the degenerate SH wavelength [10]. Thus, this is a new kind of RR wave, excited in the SHG spectrum or the DFG spectrum, whose parametric control gives new opportunities for covering spectral gaps. We see this opportunity arise especially for microcavities where it is difficult to get a very broadband spectrum for frequency comb self referencing, and currently soliton dynamics is helping to overcome this obstacle [184]. In addition quadratic nonlinearities are currently being explored for on-chip inherent harmonic conversion of the IR comb lines [185, 186, 187, 188, 189]. This means that three-wave mixing RR waves can provide a unique tunable control over the coherent extension of the comb lines.

8.1 Current and future challenges

Let us end by providing an overview over the current topics and challenges that are connected to the cascading research presented in this thesis in one way or another.

There are some interesting new aspects to explore in nonlinear crystals pumping in the anomalous dispersion regime. First of all, the absence of a soliton leads to optical wave breaking, where the continuum becomes very flat and the pulse is heavily chirped

(similar to what we showed in Sec. 7.1.3). The chirp is extremely linear over the entire pulse profile, so very efficient post-compression can be done with dispersive elements. For the defocusing case this technique can be taken to Joule-class pulses [117], in principle, and any of the type 0 crystals shown in the crystal roadmap Fig. 4.3 can be used in the anomalous dispersion range, so there is a large potential for making a mid-IR external compressor. Additionally, while the wavebreaking supercontinuum is less broadband, it is known to be low noise, extremely coherent and often very flat spectrally, which are all beneficial for, e.g. spectroscopy. Secondly, recent experiments in BBO showed controlled filamentation when cascading is focusing and dispersion is anomalous [39]. It would be interesting to investigate this further, e.g. in the mid-IR in a type I configuration where extremely large focusing nonlinearities can be produced.

We have in this thesis focused on high-power pulses (sub-GW peak powers and beyond), but we have also made and effort to exploit cascading in waveguides, specifically LN, where the hope is that similar nonlinear effects (soliton formation, supercontinuum generation, tunable RR waves in the mid-IR etc.) can be observed with kW class pulses from e.g. fiber laser oscillators. Supercontinuum generation in PPLN waveguides has been observed [32, 33], even extending to 3 μm, and the hope is to exploit the new knowledge we have of the physics behind cascading to push this to beyond 5 μm like in the bulk PPLN experiment we recently conducted [14]. Our simulations [85, 190, 191] and experiment [34] showed that ridge waveguides are probably the best option for obtaining mid-IR mode guidance. This was also confirmed recently in a seminal experiment [192], where the pumping condition was not directly from a fiber laser but was instead a cascaded supercontinuum.

Another very exciting field is so-called hollow-core anti-resonant fibers [193, 194, 195], which are currently revolutionizing the nonlinear optics community. The exciting prospect is that they are bridging the fiber optics community (where a soliton has nJ energy and kW peak power) with the bulk community (where a filaments and defocusing solitons have MW-GW of peak powers and μJ energies). The fibers can provide broadband guidance of sub-mJ energies over octaves of bandwidth, and remarkably silica fibers can be used well into the short-wavelength mid-IR. We investigated potential designs for low loss and effective single-mode operation in a large core [196, 197, 198], with the goal of conducting nonlinear optics experiments in the mid-IR with μJ pulse energies [131]. The question right now is whether the mid-IR range has some surprising new effects in store regarding plasma formation through ionization of the gas, which is the physical process behind filamentation, and this can be studied in such fibers. Additionally, these fibers are excellent for high-energy pulse compression, another topic we have researched over the past decade. The tunability of such a gas-filled fiber (pressure control over dispersion and nonlinear response), the energy levels (10s of μJ or more) and the prospect of mid-IR operation lies extremely close to what this thesis has presented and what we plan about doing in the years to come. We recently discovered though simulations [131] that when the gas in a hollow-core fiber is ionized in the mid-IR, the focusing nonlinearity of the gas suddenly gets a competing defocusing nonlinearity from the plasma, which is delayed. This is strikingly identical to the defocusing SPM vs. delayed focusing Raman that we have discussed in the previous chapters, except the signs of the dispersion and the nonlinearities are all reversed.

One of the main drivers behind our research has been to use near-IR lasers to go to

the mid-IR, especially concerning RR wave excitation and the associated supercontinuum generation. In silica fibers this is not possible because silica fibers do not transmit beyond 2.4 μm. Fluoride or chalcogenide fibers are mid-IR transparent, but the have the challenge that they need to be pumped at longer wavelengths, and they do not have the required dispersion engineering to get the second ZDW at longer wavelengths as required to couple from a focusing soliton to longer wavelengths. Therefore the current developments in silicon-based photonics is extremely interesting, because now waveguides are readily available for pumping with low-power femtosecond Er-based fiber lasers in the telecom C window, and where the dispersion can be tailored to give two zero-dispersion wavelengths around the soliton at the pump wavelength [199, 200, 201]. The new superstar in this context is silicon-rich nitride, which alleviates many of the obstacles provided in using silicon for nonlinear optics (see e.g. [202]), and avoids the low nonlinear effects of stoichiometric silicon nitride [203]. We recently showed very broadband supercontinuum generation with below 100 pJ of pulse energy (sub-kW peak power) [137], and we are currently pushing towards getting the long-wavelength RR wave further into the mid-IR by tailored dispersion engineering.

Bibliography

[1] M. Bache, O. Bang, J. Moses, and F. W. Wise, "Nonlocal explanation of stationary and nonstationary regimes in cascaded soliton pulse compression," Opt. Lett. **32,** 2490–2492 (2007).

[2] M. Bache, J. Moses, and F. W. Wise, "Scaling laws for soliton pulse compression by cascaded quadratic nonlinearities," J. Opt. Soc. Am. B **24,** 2752–2762 (2007), [erratum: *ibid.*, **27**, 2505 (2010)].

[3] M. Bache, O. Bang, W. Krolikowski, J. Moses, and F. W. Wise, "Limits to compression with cascaded quadratic soliton compressors," Opt. Express **16,** 3273–3287 (2008).

[4] M. Bache and F. W. Wise, "Type-I cascaded quadratic soliton compression in lithium niobate: Compressing femtosecond pulses from high-power fiber lasers," Phys. Rev. A **81,** 053815 (2010).

[5] M. Bache, O. Bang, B. B. Zhou, J. Moses, and F. W. Wise, "Optical Cherenkov radiation in ultrafast cascaded second-harmonic generation," Phys. Rev. A **82,** 063806 (2010).

[6] M. Bache, O. Bang, B. B. Zhou, J. Moses, and F. W. Wise, "Optical Cherenkov radiation by cascaded nonlinear interaction: an efficient source of few-cycle energetic near- to mid-IR pulses," Opt. Express **19,** 22557–22562 (2011).

[7] B. B. Zhou, A. Chong, F. W. Wise, and M. Bache, "Ultrafast and Octave-Spanning Optical Nonlinearities from Strongly Phase-Mismatched Quadratic Interactions," Phys. Rev. Lett. **109,** 043902 (2012).

[8] M. Bache, H. Guo, B. Zhou, and X. Zeng, "The anisotropic Kerr nonlinear refractive index of the beta-barium borate (β-BaB_2O_4) nonlinear crystal," Opt. Mater. Express **3,** 357–382 (2013).

[9] M. Bache, H. Guo, and B. Zhou, "Generating mid-IR octave-spanning supercontinua and few-cycle pulses with solitons in phase-mismatched quadratic nonlinear crystals," Opt. Mater. Express **3,** 1647–1657 (2013).

[10] B. Zhou, H. Guo, and M. Bache, "Soliton-induced nonlocal resonances observed through high-intensity tunable spectrally compressed second-harmonic peaks," Phys. Rev. A **90,** 013823 (2014).

[11] B. Zhou, H. Guo, and M. Bache, "Energetic mid-IR femtosecond pulse generation by self-defocusing soliton-induced dispersive waves in a bulk quadratic nonlinear crystal," Opt. Express **23,** 6924–6936 (2015).

[12] B. Zhou and M. Bache, "Dispersive waves induced by self-defocusing temporal solitons in a beta-barium-borate crystal," Opt. Lett. **40,** 4257–4260 (2015).

[13] B. Zhou and M. Bache, "Invited Article: Multiple-octave spanning high-energy mid-IR supercontinuum generation in bulk quadratic nonlinear crystals," APL Photonics **1,** 050802 (2016).

[14] B. B. Zhou, X. Liu, H. R. Guo, X. L. Zeng, X. F. Chen, H. P. Chung, Y. H. Chen, and M. Bache, "Parametrically Tunable Soliton-Induced Resonant Radiation by Three-Wave Mixing," Phys. Rev. Lett. **118,** 143901 (2017).

[15] L. A. Ostrovskii, "Self-action of light in crystals," Pis'ma Zh. Eksp. Teor. Fiz. **5,** 331 (1967), [JETP Lett. **5**, 272-275 (1967)].

[16] S. Saltiel, S. Tanev, and A. D. Boardman, "High-order nonlinear phase shift caused by cascaded third-order processes," Opt. Lett. **22,** 148–150 (1997).

[17] M. Bache, F. Eilenberger, and S. Minardi, "Higher-order Kerr effect and harmonic cascading in gases," Opt. Lett. **37,** 4612–4614 (2012).

[18] R. DeSalvo, D. Hagan, M. Sheik-Bahae, G. Stegeman, E. W. Van Stryland, and H. Vanherzeele, "Self-focusing and self-defocusing by cascaded second-order effects in KTP," Opt. Lett. **17,** 28–30 (1992).

[19] R. Maleck Rassoul, A. Ivanov, E. Freysz, A. Ducasse, and F. Hache, "Second-harmonic generation under phase-velocity and group-velocity mismatch: influence of cascading self-phase and cross-phase modulation," Opt. Lett. **22,** 268–270 (1997).

[20] X. Liu, L.-J. Qian, and F. W. Wise, "High-energy pulse compression by use of negative phase shifts produced by the cascaded $\chi^{(2)} : \chi^{(2)}$ nonlinearity," Opt. Lett. **24,** 1777–1779 (1999).

[21] X. Liu, K. Beckwitt, and F. Wise, "Two-dimensional optical spatiotemporal solitons in quadratic media," Phys. Rev. E **62,** 1328–1340 (2000).

[22] P. Di Trapani, A. Bramati, S. Minardi, W. Chinaglia, C. Conti, S. Trillo, J. Kilius, and G. Valiulis, "Focusing versus Defocusing Nonlinearities due to Parametric Wave Mixing," Phys. Rev. Lett. **87,** 183902 (2001).

[23] S. Ashihara, J. Nishina, T. Shimura, and K. Kuroda, "Soliton compression of femtosecond pulses in quadratic media," J. Opt. Soc. Am. B **19,** 2505–2510 (2002).

[24] P. Di Trapani, G. Valiulis, A. Piskarskas, O. Jedrkiewicz, J. Trull, C. Conti, and S. Trillo, "Spontaneously Generated X-Shaped Light Bullets," Phys. Rev. Lett. **91,** 093904 (2003).

[25] O. Jedrkiewicz, J. Trull, G. Valiulis, A. Piskarskas, C. Conti, S. Trillo, and P. Di Trapani, "Nonlinear X waves in second-harmonic generation: Experimental results," Phys. Rev. E **68,** 026610 (2003).

[26] S. Ashihara, T. Shimura, K. Kuroda, N. E. Yu, S. Kurimura, K. Kitamura, M. Cha, and T. Taira, "Optical pulse compression using cascaded quadratic nonlinearities in periodically poled lithium niobate," Appl. Phys. Lett. **84,** 1055–1057 (2004).

[27] J. Moses and F. W. Wise, "Soliton compression in quadratic media: high-energy few-cycle pulses with a frequency-doubling crystal," Opt. Lett. **31,** 1881–1883 (2006).

[28] X. Zeng, S. Ashihara, X. Chen, T. Shimura, and K. Kuroda, "Two-color pulse compression in aperiodically-poled lithium niobate," Opt. Commun. **281,** 4499 – 4503 (2008).

[29] J. Moses, E. Alhammali, J. M. Eichenholz, and F. W. Wise, "Efficient high-energy femtosecond pulse compression in quadratic media with flattop beams," Opt. Lett. **32,** 2469–2471 (2007).

[30] M. Seidel, J. Brons, G. Arisholm, K. Fritsch, V. Pervak, and O. Pronin, "Efficient High-Power Ultrashort Pulse Compression in Self-Defocusing Bulk Media," Scientific Reports **7,** 1410– (2017).

[31] T. Fuji *et al.*, "Monolithic carrier-envelope phase-stabilization scheme," Opt. Lett. **30,** 332–334 (2005).

[32] C. Langrock, M. M. Fejer, I. Hartl, and M. E. Fermann, "Generation of octave-spanning spectra inside reverse-proton-exchanged periodically poled lithium niobate waveguides," Opt. Lett. **32,** 2478–2480 (2007).

[33] C. R. Phillips, C. Langrock, J. S. Pelc, M. M. Fejer, J. Jiang, M. E. Fermann, and I. Hartl, "Supercontinuum generation in quasi-phase-matched $LiNbO_3$ waveguide pumped by a Tm-doped fiber laser system," Opt. Lett. **36,** 3912–3914 (2011).

[34] H. R. Guo, B. B. Zhou, M. Steinert, F. Setzpfandt, T. Pertsch, H. P. Chung, Y. H. Chen, and M. Bache, "Supercontinuum generation in quadratic nonlinear waveguides without quasi-phase matching," Opt. Lett. **40,** 629–632 (2015).

[35] N. M. N. Srinivas, S. S. Harsha, and D. N. Rao, "Femtosecond supercontinuum generation in a quadratic nonlinear medium (KDP)," Opt. Express **13,** 3224–3229 (2005).

[36] R. Sai Santosh Kumar, S. Sree Harsha, and D. Narayana Rao, "Broadband supercontinuum generation in a single potassium di-hydrogen phosphate (KDP) crystal achieved in tandem with sum frequency generation," Appl. Phys. B **86,** 615–621 (2007).

[37] R. S. S. Kumar, K. L. N. Deepak, and D. N. Rao, "Depolarization properties of the femtosecond supercontinuum generated in condensed media," Phys. Rev. A **78,** 043818 (2008).

[38] K. Krupa, A. Labruyère, A. Tonello, B. M. Shalaby, V. Couderc, F. Baronio, and A. B. Aceves, "Polychromatic filament in quadratic media: spatial and spectral shaping of light in crystals," Optica **2,** 1058–1064 (2015).

[39] R. Šuminas, G. Tamošauskas, V. Jukna, A. Couairon, and A. Dubietis, "Second-order cascading-assisted filamentation and controllable supercontinuum generation in birefringent crystals," Opt. Express **25,** 6746–6756 (2017).

[40] R. Šuminas, G. Tamošauskas, G. Valiulis, and A. Dubietis, "Spatiotemporal light bullets and supercontinuum generation in β-BBO crystal with competing quadratic and cubic nonlinearities," Opt. Lett. **41,** 2097–2100 (2016).

[41] V. Ulvila, C. R. Phillips, L. Halonen, and M. Vainio, "Frequency comb generation by a continuous-wave-pumped optical parametric oscillator based on cascading quadratic nonlinearities," Opt. Lett. **38,** 4281–4284 (2013).

[42] V. Ulvila, C. R. Phillips, L. Halonen, and M. Vainio, "High-power mid-infrared frequency comb from a continuous-wave-pumped bulk optical parametric oscillator," Opt. Express **22,** 10535–10543 (2014).

[43] M. Zavelani-Rossi, G. Cerullo, and V. Magni, "Mode locking by cascading of second-order nonlinearities," IEEE J. Quantum Electron. **34,** 61–70 (1998).

[44] L. Qian, X. Liu, and F. Wise, "Femtosecond Kerr-lens mode locking with negative nonlinear phase shifts," Opt. Lett. **24,** 166–168 (1999).

[45] A. Agnesi, A. Guandalini, and G. Reali, "Self-stabilized and dispersion-compensated passively mode-locked Yb:Yttrium aluminum garnet laser," Appl. Phys. Lett. **86,** 171105 (2005).

[46] A. Agnesi, L. Carrà, F. Pirzio, and G. Reali, "Femtosecond Nd:glass oscillator operating in normal dispersion regime," Opt. Express **16,** 9549–9553 (2008).

[47] J.-J. Zondy, F. A. Camargo, T. Zanon, V. Petrov, and N. U. Wetter, "Observation of strong cascaded Kerr-lens dynamics in an optimally-coupled cw intracavity frequency-doubled Nd:YLF ring laser," Opt. Express **18,** 4796–4815 (2010).

[48] N. Meiser, K. Seger, V. Pasiskevicius, A. Zukauskas, C. Canalias, and F. Laurell, "Cascaded mode-locking of a spectrally controlled Yb:KYW laser," Appl. Phys. B pp. 1–7 (2013).

[49] C. Dorrer, R. G. Roides, J. Bromage, and J. D. Zuegel, "Self-phase modulation compensation in a regenerative amplifier using cascaded second-order nonlinearities," Opt. Lett. **39,** 4466–4469 (2014).

[50] C. R. Phillips, A. S. Mayer, A. Klenner, and U. Keller, "SESAM modelocked Yb:$CaGdAlO_4$ laser in the soliton modelocking regime with positive intracavity dispersion," Opt. Express **22,** 6060–6077 (2014).

[51] C. R. Phillips, A. S. Mayer, A. Klenner, and U. Keller, "Femtosecond mode locking based on adiabatic excitation of quadratic solitons," Optica **2,** 667–674 (2015).

[52] K. Beckwitt, F. W. Wise, L. Qian, L. A. Walker II, and E. Canto-Said, "Compensation for self-focusing by use of cascade quadratic nonlinearity," Opt. Lett. **26,** 1696–1698 (2001).

[53] C. Conti, S. Trillo, P. D. Trapani, J. Kilius, A. Bramati, S. Minardi, W. Chinaglia, and G. Valiulis, "Effective lensing effects in parametric frequency conversion," J. Opt. Soc. Am. B **19,** 852–859 (2002).

[54] S. Cussat-Blanc, R. Maleck Rassoul, A. Ivanov, E. Freysz, and A. Ducasse, "Influence of cascading phenomena on a type I second-harmonic wave generated by an intense femtosecond pulse: application to the measurement of the effective second-order coefficient," Opt. Lett. **23,** 1585–1587 (1998).

[55] S. Ashihara, J. Nishina, T. Shimura, K. Kuroda, T. Sugita, K. Mizuuchi, and K. Yamamoto, "Nonlinear refraction of femtosecond pulses due to quadratic and cubic nonlinearities in periodically poled lithium tantalate," Opt. Commun. **222,** 421 – 427 (2003).

[56] J. Moses, B. A. Malomed, and F. W. Wise, "Self-Steepening of Ultrashort Optical Pulses without Self-Phase Modulation," Phys. Rev. A **76,** 021802(R) (2007).

[57] L. D. Noordam, H. J. Bakker, M. P. de Boer, and H. B. van Linden van den Heuvell, "Second-harmonic generation of femtosecond pulses: observation of phase-mismatch effects," Opt. Lett. **15,** 1464–1466 (1990).

[58] X. Liu, F. O. Ilday, K. Beckwitt, and F. W. Wise, "Femtosecond nonlinear polarization evolution based on cascade quadratic nonlinearities," Opt. Lett. **25,** 1394–1396 (2000).

[59] S. Ashihara, T. Shimura, K. Kuroda, N. E. Yu, S. Kurimura, K. Kitamura, J. H. Ro, M. Cha, and T. Taira, "Group-velocity-matched cascaded quadratic nonlinearities of femtosecond pulses in periodically poled MgO:$LiNbO_3$," Opt. Lett. **28,** 1442–1444 (2003).

[60] G. Xu, L. Qian, T. Wang, H. Zhu, C. Zhu, and D. Fan, "Spectral narrowing and temporal expanding of femtosecond pulses by use of quadratic nonlinear processes," IEEE J. Select. Top. Quantum Electron. **10,** 174–180 (2004).

[61] F. Ö. Ilday, K. Beckwitt, Y.-F. Chen, H. Lim, and F. W. Wise, "Controllable Raman-like nonlinearities from nonstationary, cascaded quadratic processes," J. Opt. Soc. Am. B **21,** 376–383 (2004).

[62] F. Baronio, C. D. Angelis, M. Marangoni, C. Manzoni, R. Ramponi, and G. Cerullo, "Spectral shift of femtosecond pulses in nonlinear quadratic PPSLT Crystals," Opt. Express **14,** 4774–4779 (2006).

[63] J. Moses and F. W. Wise, "Controllable Self-Steepening of Ultrashort Pulses in Quadratic Nonlinear Media," Phys. Rev. Lett. **97,** 073903 (2006).

[64] W. Su, L. Qian, H. Luo, X. Fu, H. Zhu, T. Wang, K. Beckwitt, Y. Chen, and F. Wise, "Induced group-velocity dispersion in phase-mismatched second-harmonic generation," J. Opt. Soc. Am. B **23,** 51–55 (2006).

[65] K. Moutzouris, F. Adler, F. Sotier, D. Träutlein, and A. Leitenstorfer, "Multimilliwatt ultrashort pulses continuously tunable in the visible from a compact fiber source," Opt. Lett. **31,** 1148–1150 (2006).

[66] M. Marangoni, C. Manzoni, R. Ramponi, G. Cerullo, F. Baronio, C. D. Angelis, and K. Kitamura, "Group-velocity control by quadratic nonlinear interactions," Opt. Lett. **31,** 534–536 (2006).

[67] M. A. Marangoni, D. Brida, M. Quintavalle, G. Cirmi, F. M. Pigozzo, C. Manzoni, F. Baronio, A. D. Capobianco, and G. Cerullo, "Narrow-bandwidth picosecond pulses by spectral compression of femtosecond pulses in second-order nonlinear crystals," Opt. Express **15,** 8884–8891 (2007).

[68] M. Centini, V. Roppo, E. Fazio, F. Pettazzi, C. Sibilia, J. W. Haus, J. V. Foreman, N. Akozbek, M. J. Bloemer, and M. Scalora, "Inhibition of Linear Absorption in Opaque Materials Using Phase-Locked Harmonic Generation," Phys. Rev. Lett. **101,** 113905 (2008).

[69] E. Fazio, F. Pettazzi, M. Centini, M. Chauvet, A. Belardini, M. Alonzo, C. Sibilia, M. Bertolotti, and M. Scalora, "Complete spatial and temporal locking in phase-mismatched second-harmonic generation," Opt. Express **17,** 3141–3147 (2009).

[70] E. Pontecorvo, S. Kapetanaki, M. Badioli, D. Brida, M. Marangoni, G. Cerullo, and T. Scopigno, "Femtosecond stimulated Raman spectrometer in the 320-520nm range," Opt. Express **19,** 1107–1112 (2011).

[71] G. Valiulis, V. Jukna, O. Jedrkiewicz, M. Clerici, E. Rubino, and P. DiTrapani, "Propagation dynamics and X-pulse formation in phase-mismatched second-harmonic generation," Phys. Rev. A **83,** 043834 (2011).

[72] F. Baronio, M. Conforti, C. D. Angelis, D. Modotto, S. Wabnitz, M. Andreana, A. Tonello, P. Leproux, and V. Couderc, "Second and third order susceptibilities mixing for supercontinuum generation and shaping," Opt. Fiber Technol. **18,** 283 – 289 (2012).

[73] C. Rolland and P. B. Corkum, "Compression of high-power optical pulses," J. Opt. Soc. Am. B **5,** 641–647 (1988).

[74] M. Nisoli, S. D. Silvestri, and O. Svelto, "Generation of high energy 10 fs pulses by a new pulse compression technique," Appl. Phys. Lett. **68,** 2793–2795 (1996).

[75] C. Hauri, W. Kornelis, F. Helbing, A. Heinrich, A. Couairon, A. Mysyrowicz, J. Biegert, and U. Keller, "Generation of intense, carrier-envelope phase-locked few-cycle laser pulses through filamentation," Appl. Phys. B **79,** 673–677 (2004).

[76] A. Jarnac *et al.*, "Compression of TW class laser pulses in a planar hollow waveguide for applications in strong-field physics," The European Physical Journal D **68,** 373 (2014).

[77] D. V. Skryabin and A. V. Gorbach, "Colloquium: Looking at a soliton through the prism of optical supercontinuum," Rev. Mod. Phys. **82,** 1287–1299 (2010).

[78] P. He *et al.*, "High-efficiency supercontinuum generation in solid thin plates at 0.1 TW level," Opt. Lett. **42,** 474–477 (2017).

[79] V. Shumakova, P. Malevich, S. Ališauskas, A. Voronin, A. M. Zheltikov, D. Faccio, D. Kartashov, A. Baltuska, and A. Pugzlys, "Multi-millijoule few-cycle mid-infrared pulses through nonlinear self-compression in bulk," Nat. Commun. **7,** 12877– (2016).

[80] A. A. Balakin, A. V. Kim, A. G. Litvak, V. A. Mironov, and S. A. Skobelev, "Extreme self-compression of laser pulses in the self-focusing mode resistant to transverse instability," Phys. Rev. A **94,** 043812 (2016).

[81] X. Liu, B. Zhou, H. Guo, and M. Bache, "Mid-IR femtosecond frequency conversion by soliton-probe collision in phase-mismatched quadratic nonlinear crystals," Opt. Lett. **40,** 3798–3801 (2015), arXiv:1505.05180.

[82] N. I. Nikolov, D. Neshev, O. Bang, and W. Z. Krolikowski, "Quadratic solitons as nonlocal solitons," Phys. Rev. E **68,** 036614 (2003).

[83] A. W. Snyder and D. J. Mitchell, "Accessible Solitons," Science **276,** 1538–1541 (1997).

[84] W. Krolikowski, O. Bang, N. Nikolov, D. Neshev, J. Wyller, J. Rasmussen, and D. Edmundson, "Modulational instability, solitons and beam propagation in spatially nonlocal nonlinear media," J. Opt. B: Quantum Semiclass. Opt. **6,** s288–s294 (2004).

[85] H. Guo, X. Zeng, B. Zhou, and M. Bache, "Nonlinear wave equation in frequency domain: accurate modeling of ultrafast interaction in anisotropic nonlinear media," J. Opt. Soc. Am. B **30,** 494–504 (2013).

[86] H. J. Bakker, W. Joosen, and L. D. Noordam, "Observation of frequency modulation in second-harmonic generation of ultrashort pulses," Phys. Rev. A **45,** 5126–5134 (1992).

[87] P. Pioger, V. Couderc, L. Lefort, A. Barthelemy, F. Baronio, C. D. Angelis, Y. Min, V. Quiring, and W. Sohler, "Spatial trapping of short pulses in Ti-indiffused $LiNbO_3$ waveguides," Opt. Lett. **27,** 2182–2184 (2002).

[88] H. Zhu, T. Wang, W. Zheng, P. Yuan, L. Qian, and D. Fan, "Efficient second harmonic generation of femtosecond laser at one micron," Opt. Express **12,** 2150–2155 (2004).

[89] F. Baronio *et al.*, "Generation of quadratic spatially trapped beams with short pulsed light," J. Opt. B: Quantum Semiclass. Opt. **6,** S182–S189 (2004).

[90] M. Bache and R. Schiek, "Review of measurements of Kerr nonlinearities in lithium niobate: the role of the delayed Raman response," arXiv:1211.1721 (2012).

[91] T. Brabec and F. Krausz, "Nonlinear Optical Pulse Propagation in the Single-Cycle Regime," Phys. Rev. Lett. **78,** 3282–3285 (1997).

[92] W. Ettoumi, Y. Petit, J. Kasparian, and J.-P. Wolf, "Generalized Miller Formulæ," Opt. Express **18,** 6613–6620 (2010).

[93] M. Sheik-Bahae, A. Said, T.-H. Wei, D. Hagan, and E. Van Stryland, "Sensitive measurement of optical nonlinearities using a single beam," IEEE J. Quantum Electron. **26,** 760–769 (1990).

[94] P. Kinsler, "Optical pulse propagation with minimal approximations," Phys. Rev. A **81,** 013819 (2010).

[95] A. Couairon, E. Brambilla, T. Corti, D. Majus, O. de J. Ramírez-Góngora, and M. Kolesik, "Practitioner's guide to laser pulse propagation models and simulation," Eur. Phys. J. Special Topics **199,** 5–76 (2011).

[96] M. Conforti, F. Baronio, and C. De Angelis, "Ultrabroadband Optical Phenomena in Quadratic Nonlinear Media," IEEE Photon. J. **2,** 600–610 (2010).

[97] M. Conforti, F. Baronio, and C. De Angelis, "Nonlinear envelope equation for broadband optical pulses in quadratic media," Phys. Rev. A **81,** 053841 (2010).

[98] M. Conforti, A. Marini, T. X. Tran, D. Faccio, and F. Biancalana, "Interaction between optical fields and their conjugates in nonlinear media," Opt. Express **21,** 31239–31252 (2013).

[99] M. Bache, "The Nonlinear Analytical Envelope Equation in quadratic nonlinear crystals," arXiv:1603.00188 (unpublished).

[100] M. Conforti, F. Baronio, and C. D. Angelis, "Modeling of ultrabroadband and single-cycle phenomena in anisotropic quadratic crystals," J. Opt. Soc. Am. B **28,** 1231–1237 (2011).

[101] G. P. Agrawal, *Nonlinear fiber optics*, 5 ed. (Academic Press, San Diego, 2012).

[102] H. Tan, G. P. Banfi, and A. Tomaselli, "Optical frequency mixing through cascaded second-order processes in beta-barium borate," Appl. Phys. Lett. **63,** 2472–2474 (1993).

[103] F. Hache, A. Zéboulon, G. Gallot, and G. M. Gale, "Cascaded second-order effects in the femtosecond regime in β-barium borate: self-compression in a visible femtosecond optical parametric oscillator," Opt. Lett. **20,** 1556–1558 (1995).

[104] R. DeSalvo, A. A. Said, D. Hagan, E. W. Van Stryland, and M. Sheik-Bahae, "Infrared to ultraviolet measurements of two-photon absorption and n_2 in wide bandgap solids," IEEE J. Quantum Electron. **32,** 1324–1333 (1996).

[105] M. Sheik-Bahae and M. Ebrahimzadeh, "Measurements of nonlinear refraction in the second-order $\chi^{(2)}$ materials $KTiOPO_4$, $KNbO_3$, β-BaB_2O_4 and LiB_3O_5," Opt. Commun. **142,** 294–298 (1997).

[106] H. Li, F. Zhou, X. Zhang, and W. Ji, "Bound electronic Kerr effect and self-focusing induced damage in second-harmonic-generation crystals," Opt. Commun. **144,** 75 – 81 (1997).

[107] H. P. Li, C. H. Kam, Y. L. Lam, and W. Ji, "Femtosecond Z-scan measurements of nonlinear refraction in nonlinear optical crystals," Opt. Mater. **15,** 237–242 (2001).

[108] R. Ganeev, I. Kulagin, A. Ryasnyanskii, R. Tugushev, and T. Usmanov, "The nonlinear refractive indices and nonlinear third-order susceptibilities of quadratic crystals," Opt. Spectrosc. **94,** 561–568 (2003), [Opt. Spektrosk. **94**, 615-623 (2003)].

[109] P. S. Banks, M. D. Feit, and M. D. Perry, "High-intensity third-harmonic generation," J. Opt. Soc. Am. B **19,** 102–118 (2002).

[110] D. N. Nikogosyan, "Beta barium borate (BBO) - A review of its properties and applications," Appl. Phys. A **52,** 359–368 (1991).

[111] J. E. Midwinter and J. Warner, "The effects of phase matching method and of crystal symmetry on the polar dependence of third-order non-linear optical polarization," Br. J. Appl. Phys. **16,** 1667–1674 (1965).

[112] C. Wang and E. Baardsen, "Optical third harmonic generation using mode-locked and non-mode-locked lasers," Appl. Phys. Lett. **15,** 396–397 (1969).

[113] M. Sheik-Bahae, D. Hutchings, D. Hagan, and E. Van Stryland, "Dispersion of bound electron nonlinear refraction in solids," IEEE J. Quantum Electron. **27,** 1296 –1309 (1991).

[114] R. C. Miller, "Optical second harmonic generation in piezoelectric crystals," Appl. Phys. Lett. **5,** 17–19 (1964).

[115] M. Sheik-Bahae and E. W. V. Stryland, "Optical Nonlinearities in the Transparency Region of Bulk Semiconductors," in *Nonlinear Optics in Semiconductors I*, Vol. 58 of *Semiconductors and Semimetals*, E. Garmire and A. Kost, eds., (Elsevier, 1998), Chap. 4, pp. 257 – 318.

[116] S. Ashihara and Y. Kawahara, "Spectral broadening of mid-infrared femtosecond pulses in GaAs," Opt. Lett. **34,** 3839–3841 (2009).

[117] M. Bache and B. Zhou, "High-Energy Compression of Mid-IR Pulses in a Bulk Nonlinear Crystal," In *2015 European Conference on Lasers and Electro-Optics - European Quantum Electronics Conference*, p. CF.3.6 (Optical Society of America, 2015).

[118] W. J. Tomlinson, R. H. Stolen, and A. M. Johnson, "Optical wave breaking of pulses in nonlinear optical fibers," Opt. Lett. **10,** 457–459 (1985).

[119] S. De Silvestri, M. Nisoli, G. Sansone, S. Stagira, and O. Svelto, "Few-Cycle Pulses by External Compression," in *Few-Cycle Laser Pulse Generation and Its Applications*, Vol. 95 of *Topics in Applied Physics*, F. X. Kärtner, ed., (Springer Berlin, 2004), pp. 137–178.

[120] E. Granados, L.-J. Chen, C.-J. Lai, K.-H. Hong, and F. X. Kärtner, "Wavelength scaling of optimal hollow-core fiber compressors in the single-cycle limit," Optics Express **20,** 9099 (2012).

[121] G. Tamosauskas, A. Dubietis, and G. Valiulis, "Soliton-effect optical pulse compression in bulk media with $\chi^{(3)}$ nonlinearity," Nonlinear Anal. Modelling Control **5,** 99–105 (2000).

[122] M. Hemmer, M. Baudisch, A. Thai, A. Couairon, and J. Biegert, "Self-compression to sub-3-cycle duration of mid-infrared optical pulses in dielectrics," Opt. Express **21,** 28095–28102 (2013).

[123] A. Pugzlys, P. Malevich, S. Alisauskas, A. A. Voronin, D. Kartashov, A. Baltuska, A. Zheltikov, and D. Faccio, "Self-compression of Millijoule mid-IR Femtosecond Pulses in Transparent Dielectrics," In *CLEO: 2014*, p. FTh1D.3 (Optical Society of America, 2014).

[124] A. V. Husakou and J. Herrmann, "Supercontinuum Generation of Higher-Order Solitons by Fission in Photonic Crystal Fibers," Phys. Rev. Lett. **87,** 203901 (2001).

[125] H. Li, C. Kam, Y. Lam, F. Zhou, and W. Ji, "Nonlinear refraction of undoped and Fe-doped $KTiOAsO_4$ crystals in the femtosecond regime," Appl. Phys. B **70,** 385–388 (2000).

[126] L. F. Mollenauer, R. H. Stolen, J. P. Gordon, and W. J. Tomlinson, "Extreme picosecond pulse narrowing by means of soliton effect in single-mode optical fibers," Opt. Lett. **8,** 289–291 (1983).

[127] W. J. Tomlinson, R. H. Stolen, and C. V. Shank, "Compression of optical pulses chirped by self-phase modulation in fibers," J. Opt. Soc. Am. B **1,** 139–149 (1984).

[128] E. M. Dianov, Z. S. Nikonova, A. M. Prokhorov, and V. N. Serkin, "Optimal compression of multi-soliton pulses in optical fibers," Sov. Tech. Phys. Lett. **12,** 311–313 (1986), [Pis'ma Zh. Tekh. Fiz. **12**, 756–760 (1986)].

[129] M. Bache, B. Zhou, A. Chong, and F. W. Wise, "Generating Energetic Few-Cycle Pulses at 800 nm Using Soliton Compression with Type 0 Cascaded Quadratic Interaction in Lithium Niobate," In *Conference on Lasers and Electro-Optics*, p. CWA5 (Optical Society of America, 2010).

[130] J. Burghoff, H. Hartung, S. Nolte, and A. Tünnermann, "Structural properties of femtosecond laser-induced modifications in $LiNbO_3$," Appl. Phys. A **86,** 165–170 (2007).

[131] M. S. Habib, C. Markos, O. Bang, and M. Bache, "Soliton-plasma nonlinear dynamics in mid-IR gas-filled hollow-core fibers," Opt. Lett. **42,** 2232–2235 (2017), Opt. Lett. **42,** 2943-2943 (2017).

[132] M. Bache and B. Zhou, "Cascaded Soliton Compression of Energetic Femtosecond Pulses at 1030 nm," In *Research in Optical Sciences*, p. JT2A.60 (Optical Society of America, 2012).

[133] P. K. A. Wai, C. R. Menyuk, Y. C. Lee, and H. H. Chen, "Nonlinear pulse propagation in the neighborhood of the zero-dispersion wavelength of monomode optical fibers," Opt. Lett. **11,** 464–466 (1986).

[134] N. Akhmediev and M. Karlsson, "Cherenkov radiation emitted by solitons in optical fibers," Phys. Rev. A **51,** 2602–2607 (1995).

[135] I. Cristiani, R. Tediosi, L. Tartara, and V. Degiorgio, "Dispersive wave generation by solitons in microstructured optical fibers," Opt. Express **12,** 124–135 (2003).

[136] J. M. Dudley, G. Genty, and S. Coen, "Supercontinuum generation in photonic crystal fiber," Rev. Mod. Phys. **78,** 1135–1184 (2006).

[137] X. Liu, M. Pu, B. Zhou, C. J. Krückel, A. Fülöp, V. Torres-Company, and M. Bache, "Octave-spanning supercontinuum generation in a silicon-rich nitride waveguide," Opt. Lett. **41,** 2719–2722 (2016).

[138] D. V. Skryabin and A. V. Yulin, "Theory of generation of new frequencies by mixing of solitons and dispersive waves in optical fibers," Phys. Rev. E **72,** 016619 (2005).

[139] D. V. Skryabin, F. Luan, J. C. Knight, and P. S. J. Russell, "Soliton Self-Frequency Shift Cancellation in Photonic Crystal Fibers," Science **301,** 1705–1708 (2003).

[140] D. Nikogosyan, *Nonlinear Optical Crystals: A Complete Survey* (Springer, Berlin, 2005).

[141] D. Zhang, Y. Kong, and J. Zhang, "Optical parametric properties of 532-nm-pumped beta-barium-borate near the infrared absorption edge," Opt. Commun. **184,** 485–491 (2000).

[142] K. Kato, N. Umemura, and T. Mikami, in *Sellmeier and thermo-optic dispersion formulas for beta-BaB[sub 2]O[sub 4] (revisited)*, P. E. Powers, ed., (SPIE, 2010), No. 1, p. 75821L.

[143] O. Gayer, Z. Sacks, E. Galun, and A. Arie, "Temperature and wavelength dependent refractive index equations for MgO-doped congruent and stoichiometric $LiNbO_3$," Appl. Phys. B **91,** 343–348 (2008).

[144] J.-P. Fève, B. Boulanger, O. Pacaud, I. Rousseau, B. Ménaert, G. Marnier, P. Villeval, C. Bonnin, G. M. Loiacono, and D. N. Loiacono, "Phase-matching measurements and Sellmeier equations over the complete transparency range of KTiOAsO4, RbTiOAsO4, and CsTiOAsO4," J. Opt. Soc. Am. B **17,** 775–780 (2000).

[145] K. Fradkin-Kashi, A. Arie, P. Urenski, and G. Rosenman, "Mid-infrared difference–frequency generation in periodically poled KTiOAsO4 and application to gas sensing," Opt. Lett. **25,** 743–745 (2000).

[146] S.-J. Im, A. Husakou, and J. Herrmann, "High-power soliton-induced supercontinuum generation and tunable sub-10-fs VUV pulses from kagome-lattice HC-PCFs," Opt. Express **18,** 5367–5374 (2010).

[147] F. Belli, A. Abdolvand, W. Chang, J. C. Travers, and P. S. Russell, "Vacuum-ultraviolet to infrared supercontinuum in hydrogen-filled photonic crystal fiber," Optica **2,** 292–300 (2015).

[148] N. Y. Joly, J. Nold, W. Chang, P. Hölzer, A. Nazarkin, G. K. L. Wong, F. Biancalana, and P. S. J. Russell, "Bright Spatially Coherent Wavelength-Tunable Deep-UV Laser Source Using an Ar-Filled Photonic Crystal Fiber," Phys. Rev. Lett. **106,** 203901 (2011).

[149] D. Novoa, M. Cassataro, J. C. Travers, and P. S. J. Russell, "Photoionization-Induced Emission of Tunable Few-Cycle Midinfrared Dispersive Waves in Gas-Filled Hollow-Core Photonic Crystal Fibers," Phys. Rev. Lett. **115,** 033901 (2015).

[150] X. Zeng, H. Guo, B. Zhou, and M. Bache, "Soliton compression to few-cycle pulses with a high quality factor by engineering cascaded quadratic nonlinearities," Opt. Express **20,** 27071–27082 (2012).

[151] M. Conforti, N. Westerberg, F. Baronio, S. Trillo, and D. Faccio, "Negative-frequency dispersive wave generation in quadratic media," Phys. Rev. A **88,** 013829 (2013).

[152] E. Rubino, J. McLenaghan, S. C. Kehr, F. Belgiorno, D. Townsend, S. Rohr, C. E. Kuklewicz, U. Leonhardt, F. König, and D. Faccio, "Negative-Frequency Resonant Radiation," Phys. Rev. Lett. **108,** 253901 (2012).

[153] C. R. Lourés, T. Roger, D. Faccio, and F. Biancalana, "Superresonant Radiation Stimulated by Higher Harmonics," Phys. Rev. Lett. **118,** 043902 (2017).

[154] Q. Hu, B.Sc. thesis supervised by Morten Bache, Technical University of Denmark, 2010, cascaded Soliton Compression with Difference Frequency Generation.

[155] A. Nahata, A. S. Weling, and T. F. Heinz, "A wideband coherent terahertz spectroscopy system using optical rectification and electro-optic sampling," Appl. Phys. Lett. **69,** 2321–2323 (1996).

[156] Y.-S. Lee, T. Meade, V. Perlin, H. Winful, T. B. Norris, and A. Galvanauskas, "Generation of narrow-band terahertz radiation via optical rectification of femtosecond pulses in periodically poled lithium niobate," Applied Physics Letters **76,** 2505–2507 (2000).

[157] J. L'huillier, G. Torosyan, M. Theuer, Y. Avetisyan, and R. Beigang, "Generation of THz radiation using bulk, periodically and aperiodically poled lithium niobate – Part 1: Theory," Appl. Phys. B **86,** 185–196 (2007).

[158] J. L'huillier, G. Torosyan, M. Theuer, C. Rau, Y. Avetisyan, and R. Beigang, "Generation of THz radiation using bulk, periodically and aperiodically poled lithium niobate – Part 2: Experiments," Appl. Phys. B **86,** 197–208 (2007).

[159] K. F. Mak, J. C. Travers, P. Hölzer, N. Y. Joly, and P. S. J. Russell, "Tunable vacuum-UV to visible ultrafast pulse source based on gas-filled Kagome-PCF," Opt. Express **21,** 10942–10953 (2013).

[160] A. Ermolov, K. F. Mak, M. H. Frosz, J. C. Travers, and P. S. J. Russell, "Supercontinuum generation in the vacuum ultraviolet through dispersive-wave and soliton-plasma interaction in a noble-gas-filled hollow-core photonic crystal fiber," Phys. Rev. A **92,** 033821 (2015).

[161] *The Supercontinuum Laser Source*, 2 ed., R. R. Alfano, ed., (Springer, New York, 2006).

[162] G. Fibich and A. L. Gaeta, "Critical power for self-focusing in bulk media and in hollow waveguides," Opt. Lett. **25,** 335–337 (2000).

[163] A. Couairon and A. Mysyrowicz, "Femtosecond filamentation in transparent media," Phys. Rep. **441,** 47–189 (2007).

[164] A. Brodeur and S. L. Chin, "Ultrafast white-light continuum generation and self-focusing in transparent condensed media," J. Opt. Soc. Am. B **16,** 637–650 (1999).

[165] M. Bradler, P. Baum, and E. Riedle, "Femtosecond continuum generation in bulk laser host materials with sub-μJ pump pulses," Applied Physics B **97,** 561 (2009).

[166] P. B. Corkum, P. P. Ho, R. R. Alfano, and J. T. Manassah, "Generation of infrared supercontinuum covering 3–14 μm in dielectrics and semiconductors," Opt. Lett. **10,** 624–626 (1985).

[167] J. J. Pigeon, S. Y. Tochitsky, C. Gong, and C. Joshi, "Supercontinuum generation from 2 to 20 μm in GaAs pumped by picosecond CO_2 laser pulses," Opt. Lett. **39,** 3246–3249 (2014).

[168] F. Silva, D. Austin, A. Thai, M. Baudisch, M. Hemmer, D. Faccio, A. Couairon, and J. Biegert, "Multi-octave supercontinuum generation from mid-infrared filamentation in a bulk crystal," Nature Comms. **3,** 807 (2012).

[169] D. Kartashov, S. Ališauskas, A. Pugžlys, A. Voronin, A. Zheltikov, M. Petrarca, P. Béjot, J. Kasparian, J.-P. Wolf, and A. Baltuška, "White light generation over three octaves by femtosecond filament at 3.9μm in argon," Opt. Lett. **37,** 3456–3458 (2012).

[170] J. Darginavičius, D. Majus, V. Jukna, N. Garejev, G. Valiulis, A. Couairon, and A. Dubietis, "Ultrabroadband supercontinuum and third-harmonic generation in bulk solids with two optical-cycle carrier-envelope phase-stable pulses at 2 μm," Opt. Express **21,** 25210–25220 (2013).

[171] H. Liang, P. Krogen, R. Grynko, O. Novak, C.-L. Chang, G. J. Stein, D. Weerawarne, B. Shim, F. X. Kärtner, and K.-H. Hong, "Three-octave-spanning supercontinuum generation and sub-two-cycle self-compression of mid-infrared filaments in dielectrics," Opt. Lett. **40,** 1069–1072 (2015).

[172] O. Mouawad, P. Béjot, F. Billard, P. Mathey, B. Kibler, F. Désévédavy, G. Gadret, J.-C. Jules, O. Faucher, and F. Smektala, "Mid-infrared filamentation-induced supercontinuum in As-S and an As-free Ge-S counterpart chalcogenide glasses," App. Phys. B **121,** 433–438 (2015).

[173] A. M. Stingel, H. Vanselous, and P. B. Petersen, "Covering the vibrational spectrum with microjoule mid-infrared supercontinuum pulses in nonlinear optical applications," J. Opt. Soc. Am. B **34,** 1163–1169 (2017).

[174] T. Fuji and T. Suzuki, "Generation of sub-two-cycle mid-infrared pulses by four-wave mixing through filamentation in air," Opt. Lett. **32,** 3330–3332 (2007).

[175] P. B. Petersen and A. Tokmakoff, "Source for ultrafast continuum infrared and terahertz radiation," Opt. Lett. **35,** 1962–1964 (2010).

[176] C. Calabrese, A. M. Stingel, L. Shen, and P. B. Petersen, "Ultrafast continuum mid-infrared spectroscopy: probing the entire vibrational spectrum in a single laser shot with femtosecond time resolution," Opt. Lett. **37,** 2265–2267 (2012).

[177] M. Durand, A. Jarnac, A. Houard, Y. Liu, S. Grabielle, N. Forget, A. Durécu, A. Couairon, and A. Mysyrowicz, "Self-Guided Propagation of Ultrashort Laser Pulses in the Anomalous Dispersion Region of Transparent Solids: A New Regime of Filamentation," Phys. Rev. Lett. **110,** 115003 (2013).

[178] S. A. Ali, P. B. Bisht, A. Nautiyal, V. Shukla, K. S. Bindra, and S. M. Oak, "Conical emission in β-barium borate under femtosecond pumping with phase matching angles away from second harmonic generation," J. Opt. Soc. Am. B **27,** 1751–1756 (2010).

[179] S. Fossier *et al.*, "Optical, vibrational, thermal, electrical, damage, and phase-matching properties of lithium thioindate," J. Opt. Soc. Am. B **21,** 1981–2007 (2004).

[180] M. Bache, B. B. Zhou, S. Ashihara, A. Stingel, H. Vanselous, and P. B. Petersen, "Multiple-μJ mid-IR supercontinuum generation in quadratic nonlinear crystals," In *2016 41st International Conference on Infrared, Millimeter, and Terahertz waves (IRMMW-THz)*, pp. 1–2 (2016).

[181] K. F. Mak, M. Seidel, O. Pronin, M. H. Frosz, A. Abdolvand, V. Pervak, A. Apolonski, F. Krausz, J. C. Travers, and P. S. J. Russell, "Compressing μJ-level pulses from 250 fs to sub-10 fs at 38-MHz repetition rate using two gas-filled hollow-core photonic crystal fiber stages," Opt. Lett. **40,** 1238–1241 (2015).

[182] K. Ravi, D. N. Schimpf, and F. X. Kärtner, "Pulse sequences for efficient multi-cycle terahertz generation in periodically poled lithium niobate," Opt. Express **24,** 25582–25607 (2016).

[183] H. Suchowski, P. R. Krogen, S.-W. Huang, F. X. Kärtner, and J. Moses, "Octave-spanning coherent mid-IR generation via adiabatic difference frequency conversion," Opt. Express **21,** 28892–28901 (2013).

[184] V. Brasch, M. Geiselmann, T. Herr, G. Lihachev, M. H. P. Pfeiffer, M. L. Gorodetsky, and T. J. Kippenberg, "Photonic chip–based optical frequency comb using soliton Cherenkov radiation," Science **351,** 357–360 (2016).

[185] H. Jung, R. Stoll, X. Guo, D. Fischer, and H. X. Tang, "Green, red, and IR frequency comb line generation from single IR pump in AlN microring resonator," Optica **1,** 396–399 (2014).

[186] S. Miller, K. Luke, Y. Okawachi, J. Cardenas, A. L. Gaeta, and M. Lipson, "On-chip frequency comb generation at visible wavelengths via simultaneous second- and third-order optical nonlinearities," Opt. Express **22,** 26517–26525 (2014).

[187] I. Ricciardi, S. Mosca, M. Parisi, P. Maddaloni, L. Santamaria, P. De Natale, and M. De Rosa, "Frequency comb generation in quadratic nonlinear media," Phys. Rev. A **91,** 063839 (2015).

[188] F. Leo, T. Hansson, I. Ricciardi, M. De Rosa, S. Coen, S. Wabnitz, and M. Erkintalo, "Walk-Off-Induced Modulation Instability, Temporal Pattern Formation, and Frequency Comb Generation in Cavity-Enhanced Second-Harmonic Generation," Phys. Rev. Lett. **116,** 033901 (2016).

[189] H. Jung, X. Guo, N. Zhu, S. B. Papp, S. A. Diddams, and H. X. Tang, "Phase-dependent interference between frequency doubled comb lines in a $\chi^{(2)}$ phase-matched aluminum nitride microring," Opt. Lett. **41,** 3747–3750 (2016).

[190] H. Guo, B. Zhou, X. Zeng, and M. Bache, "Highly coherent mid-IR supercontinuum by self-defocusing solitons in lithium niobate waveguides with all-normal dispersion," Opt. Express **22,** 12211–12225 (2014).

[191] H. Guo, X. Zeng, B. Zhou, and M. Bache, "Few-cycle solitons and supercontinuum generation with cascaded quadratic nonlinearities in unpoled lithium niobate ridge waveguides," Opt. Lett. **39,** 1105–8 (2014).

[192] K. Iwakuni, S. Okubo, O. Tadanaga, H. Inaba, A. Onae, F.-L. Hong, and H. Sasada, "Generation of a frequency comb spanning more than 3.6 octaves from ultraviolet to mid infrared," Opt. Lett. **41,** 3980–3983 (2016).

[193] A. D. Pryamikov, A. S. Biriukov, A. F. Kosolapov, V. G. Plotnichenko, S. L. Semjonov, and E. M. Dianov, "Demonstration of a waveguide regime for a silica hollow - core microstructured optical fiber with a negative curvature of the core boundary in the spectral region > 3.5 μm," Opt. Express **19,** 1441–1448 (2011).

[194] F. Yu, W. J. Wadsworth, and J. C. Knight, "Low loss silica hollow core fibers for 3–4 μm spectral region," Opt. Express **20,** 11153–11158 (2012).

[195] W. Belardi and J. C. Knight, "Hollow antiresonant fibers with low bending loss," Opt. Express **22,** 10091–10096 (2014).

[196] M. S. Habib, O. Bang, and M. Bache, "Low-loss hollow-core silica fibers with adjacent nested anti-resonant tubes," Opt. Express **23,** 17394–17406 (2015).

[197] M. S. Habib, O. Bang, and M. Bache, "Low-loss single-mode hollow-core fiber with anisotropic anti-resonant elements," Opt. Express **24,** 8429–8436 (2016).

[198] M. S. Habib, O. Bang, and M. Bache, "Low-Loss Hollow-Core Anti-Resonant Fibers With Semi-Circular Nested Tubes," IEEE Journal of Selected Topics in Quantum Electronics **22,** 156–161 (2016).

[199] J. M. C. Boggio, D. Bodenmüller, T. Fremberg, R. Haynes, M. M. Roth, R. Eisermann, M. Lisker, L. Zimmermann, and M. Böhm, "Dispersion engineered silicon nitride waveguides by geometrical and refractive-index optimization," J. Opt. Soc. Am. B **31,** 2846–2857 (2014).

[200] C. J. Krückel, A. Fülöp, T. Klintberg, J. Bengtsson, P. A. Andrekson, and V. Torres-Company, "Linear and nonlinear characterization of low-stress high-confinement silicon-rich nitride waveguides," Opt. Express **23,** 25827–25837 (2015).

[201] C. J. Krückel, A. Fülöp, T. Klintberg, J. Bengtsson, P. A. Andrekson, and V. Torres-Company, "Linear and nonlinear characterization of low-stress high-confinement silicon-rich nitride waveguides: erratum," Opt. Express **25,** 7443–7444 (2017).

[202] L. Yin and G. P. Agrawal, "Impact of two-photon absorption on self-phase modulation in silicon waveguides," Opt. Lett. **32,** 2031–2033 (2007).

[203] A. R. Johnson *et al.*, "Octave-spanning coherent supercontinuum generation in a silicon nitride waveguide," Optics Letters **40,** 5117–4 (2015).

About the author

Morten Bache was born in Copenhagen, Denmark, in 1974. He obtained his M.Sc. in engineering, specialized in Applied Physics, from the Technical University of Denmark in 1999. In his master's thesis, he worked on nonlinear structures in complex nonlinear chemical systems, during which he spent five months at Université Libre de Bruxelles, Belgium. He obtained a Ph.D. in physics in 2002 from the Department of Informatics and Mathematical Modelling at the Technical University of Denmark, where he worked on theoretical nonlinear and quantum optics and modeling of complex spatial and temporal phenomena arising from laser light interacting with quadratic nonlinear materials. During his Ph.D. he spent two months at University of Wisconsin, USA, and five months at Universitat de les Illes Balears, Spain.

Between 2002 and 2005 he held a postdoc position in the group of professor Luigi Lugiato, University of Insubria, Como, Italy. He worked on modeling spatio-temporal nonlinear and quantum properties of short, intense pulses in quadratic nonlinear materials and in vertical-cavity surface-emitting lasers.

From 2005-2008 he held a Steno postdoc grant from the Danish Natural Science Research Council at DTU Fotonik, Technical University of Denmark. He worked on so-called cascaded nonlinearities in quadratic nonlinear crystals, focusing especially on temporal soliton formation and compression of energetic femtosecond pulses. He became an assistant professor in 2007 and an associate professor in 2008 at DTU Fotonik. In 2009 he received the DFF Young Elite Researchers Award, and in 2011 he became leader of the Ultrafast Nonlinear Optics team at DTU Fotonik. His current research is focused on various aspects of ultrafast nonlinear optics, especially temporal soliton dynamics in cascaded nonlinearities in crystals, intense light-matter interaction in gases and dielectrics, nonlinear plasmonics, nonlinear effects in hollow-core gas-filled fibers and nonlinear optics in integrated waveguides and photonic crystal fibers. He has co-authored 100+ ISI peer-reviewed papers and conference contributions, with over 2,600 citations, and has received research funding for over 40 million DKK.

Cover illustration: Numerical simulation of femtosecond soliton formation in a lithium niobate crystal, illustrated in time domain (top) and wavelength domain (bottom). More details in Fig. 5.9.

Published by:
Ultrafast Infrared and Terahertz Science group
DTU Fotonik
Department of Photonics Engineering
Ørsteds Plads, bld. 343
Technical University of Denmark
2800 Kgs. Lyngby
Denmark

ISBN: 978-87-93089-99-0